Summer 2015

High Efficiency Ultrathin CIGS Solar Cells

Krishna Prasad Aryal
Old Dominion University

HIGH EFFICIENCY ULTRATHIN CIGS SOLAR CELLS

by

Krishna Prasad Aryal
M. S. August 2011, Texas Tech University

A Dissertation Submitted to the Faculty of
Old Dominion University in Partial Fulfillment of the
Requirements for the Degree of

DOCTOR OF PHILOSOPHY

ELECTRICAL AND COMPUTER ENGINEERING

OLD DOMINION UNIVERSITY
August 2015

Approved by:

Sylvain Marsillac (Director)

Hani E. Elsayed-Ali (Member)

Gon Namkoong (Member)

Gene Hou (Member)

ABSTRACT

HIGH EFFICIENCY ULTRATHIN CIGS SOLAR CELLS

Krishna Prasad Aryal
Old Dominion University, 2015
Director: Dr. Sylvain Marsillac

The global demand for renewable energy is growing rapidly. Increasing the global share of alternative sources of energy would not only bring environmental benefits, but also enhance overall energy security by diversifying energy supply. Many technology options exist nowadays to harvest the power of the sun, a sustainable energy source, and generate electricity directly from this source via the photovoltaic effect. Among them, $Cu(In,Ga)Se_2$ (CIGS) has gained significant momentum as a possible high efficiency and low cost thin film solar cell material. The capacity to scale up any photovoltaic technology is one of the criteria that will determine its long term viability. In the case of CIGS, many manufacturers are showing the way for GW-scale production capacity. However, as CIGS technology continues to increase its share of the market, the scarcity and high price of indium will potentially affect its ability to compete with other technologies. One way to avoid this bottleneck is to reduce the importance of indium in the fabrication of the cell simply by reducing its thickness without significant efficiency loss. Reducing the thickness of CIGS thin film will not only save the material but will also lower the production time and the power needed to produce the cell.

The material properties of $Cu(In,Ga)Se_2$ thin films are different with deposition process. Many different methods to deposit $Cu(In,Ga)Se_2$ thin film have been tried until now but $Cu(In,Ga)Se_2$ thin films prepared by co-evaporation of elemental sources are the most successful due to the control over the sequence of evaporation of individual material. However, the co-evaporation process is a complex process and, depending on the individual sources and substrate temperature, the thin films are grown with different characteristics. The characteristics of these thin films changes with the change in the atomic percentage (at.%) of Cu, In, Ga and Se, which depends on the evaporation conditions. Among different co-evaporation techniques to grow $Cu(In,Ga)Se_2$, 1-stage, 2-stage and 3-stage co-evaporation processes are the most successful processes

Co-evaporation process is the best technique for highly efficient CIGS solar cell but this process needs a precise control of the elemental composition in the vapor flux in order to achieve high quality material, which is not easy to obtain due to the low sticking coefficient of Selenium. One of the major concerns in $Cu(In,Ga)Se_2$ thin film solar cell fabrication that affect significantly the cell performance during deposition is stoichiometry. CIGS with low Se samples exhibited very low Cu content, additional chalcopyrite phases, very small grain size, and poor solar cell performance. So it is very important to find the minimal selenium flux to obtain high quality $Cu(In,Ga)Se_2$ thin film.

During the deposition of ultrathin $Cu(In,Ga)Se_2$ film with 1-stage, 2-stage and 3-stage co-evaporation processes, real time spectroscopic ellipsometry (RTSE) is implemented to study the material properties as well as to monitor the process. The deposition processed for individual layer of CIGS device are optimized to enhance the efficiency of the CIGS solar cell.

This dissertation is dedicated to my parents, Jagan Nath Aryal and Chandra Kala Aryal

ACKNOWLEDGMENTS

I would like to express my sincere gratitude and heartfelt appreciation to Dr. Sylvain Marsillac, my advisor for his enormous support and invaluable guidance for this project. I am greatly indebted to Dr. Marsillac for his heuristic suggestion and inspirational encouragement through this research projects and during the writing of this dissertation. His guidance and support have propelled me to be not only a better scientists but a better person in real life.

I am grateful to my committee members Dr. Hani E. Elsayed-Ali, Dr. Gon Namkoong, and Dr. Gene Hou for their time, invaluable suggestions and comments. I would like to thank Graduate Program Director, Dr. Dimitrie Popescu for his support in the completion of my doctoral studies. I would also like to thank to Dr. Christopher Bailey for his invaluable advice and guidance in my research.

I also wish to show my appreciation for all of my current and previous research teammates, Yunus Erkaya, Grace Rajan, , Tasnuva Ashrafee, Shankar Karki, Hareen Illa, Nitin Hedge, Caitlin Conway, Chad Herndon, Dr. Patrick Boland, and Dr. Vikash Ranjan.

I would like to thank my family for their never-ending support throughout my educational endeavors. In particular, I wish to thank my wife, Dina Aryal and Sons, Jagrit and Jason. Without their love and support I would be lost.

TABLE OF CONTENTS

Page

Page

LIST OF TABLES

Table Page

LIST OF FIGURES

Figure Page

Figure Page

Figure Page

Figure Page

CHAPTER 1

INTRODUCTION

1.1 Motivation and Background

Global Energy demand is expected to increase continuously every year due to population growth and economic development. In order to fulfill the energy demand with time, roughly 30 TWh of energy is required by the end of 2050. Today most of these energy demands are produced by burning fossil fuels such as coal, petroleum and natural gas. The peak supply of these energy from conventional sources has already been achieved recently or is about to be achieved within the next 20- 30 years [1]. Beside this the greenhouse gases emitted from the burning of the fossil fuels significantly affect the environment and will threaten human existence in future. In order to fulfill these future energy requirements, we, as a society, are in need of development and deployment of renewable sources of energy. Renewable energy sources such as hydroelectric, geothermal, biomass, wind and solar energy are not only abundant sources but they are also cleaner. The power of sunlight incident on the Earth is 125,000 TW, which is 10,000 times the existing annual demand of energy [2]. Energy from the sun would make life possible on this planet. At present, the typical electricity price generated from traditional sources cost ~ $0.10/kWh whereas electricity from PV plants costs around $0.27/kWh [3]. However, the electricity cost from traditional sources will continue to rise whereas the electricity from PV is decreasing due to advanced technology, improved efficiency and large scale utilities. The cross over between these prices, which is called "grid parity", will take place in the near future [4].

Many technology options exist nowadays to harvest the power of the sun, a sustainable energy source, and generate electricity directly from this source via the photovoltaic effect. Among them, $Cu(In,Ga)Se_2$ has gained significant momentum as a possible high efficiency and low cost thin film solar cell material. With 21.7% efficiency, $Cu(In,Ga)Se_2$ (CIGS) solar cells are the most efficient polycrystalline thin films solar cells today [5]. Besides high conversion efficiencies, CIGS cells have proved long term outdoor stability and radiation hardness [6-7]. The capacity to scale up any photovoltaic technology is one of the criteria that will determine its long-term viability. In the case of CIGS, many manufacturers such as Solar Frontier are showing the way for GW-scale production capacity. However, as CIGS technology continues to increase its share of the market, the scarcity and high price of indium will potentially affect its ability to compete with other technologies. One way to avoid this bottleneck is to reduce the importance of indium in the fabrication of the cell simply by reducing its thickness [8]. Reducing the thickness will not only save the material but will also lower the production time and the power needed to produce the cell. All these factors will help to reduce the production cost significantly.

1.2 Solar Cell Background Basics

A solar cell is a semiconductor device, which converts sunlight into electric power by generating current and voltage. This conversion process always consists of the following essential steps: a) generation of electron-hole pairs (e-h) in semiconductor materials by absorbing the incident photon with energy (E_{ph}) greater than or equal to the band gap (E_g) of the absorbing materials, (b) separation of these light generated e-h pairs

(c) collection of these carriers by appropriate electrodes. A p-n junction is one of the widely used structures in order to separate e-h pairs.

In order to convert incident sunlight to electrical power, photons of a range of energies need to generate electron-hole pairs. An electron-hole pair is generated only if the energy of the incident photon is enough to overcome the band gap of the materials. However, for solar cell application, photon energy greater than band gap is wasted in the form of thermalization. The current-density vs. voltage (J-V) characteristics of the solar cells measured in dark condition resemble the exponential response of a diode with higher current in the forward bias and small current in reverse bias. Under illumination, there is also a photocurrent in the cell which is in the opposite direction of the dark current and the J-V characteristics are ideally the superposition of the dark characteristics and the photocurrent. The Shockley diode equation under illumination [9] is

$$J = J_0 \left(e^{qV / AKT} - 1 \right) - J_{ph} \qquad (1.1)$$

Where J is the current density, V is the applied voltage, Jo the reverse saturation current density of the diode, q is the elementary charge, A is the ideality factor, k is the Boltzmann constant, and T is the temperature.

Figure 1.1 shows the J-V characteristics of a solar cell under illumination showing the most discussed performance parameters such as the open circuit voltage (V_{oc}), the short circuit current density (J_{sc}) and the maximum power point with voltage and current density of V_{MP} and J_{MP} respectively. The equations relating the above parameters to conversion efficiency (η) are also given.

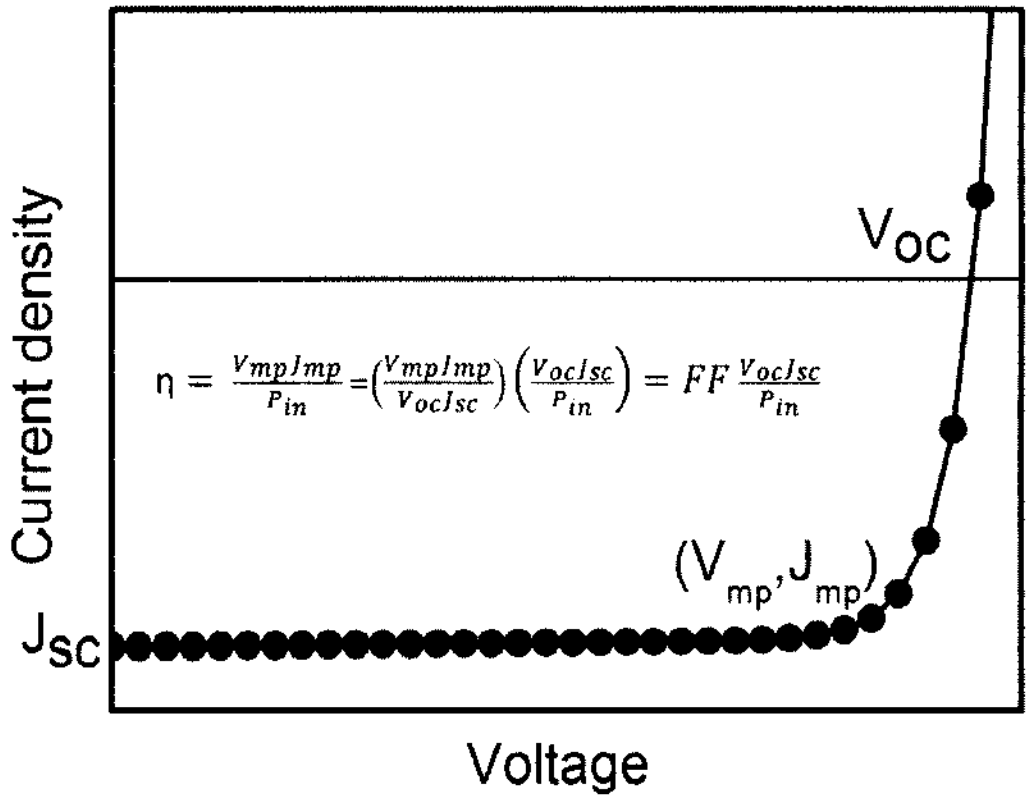

Figure 1.1 J-V characteristics of solar cells under illumination showing the open circuit (V_{oc}), the short circuit current density (J_{sc}) and the maximum power point with voltage and current density of V_{MP} and J_{MP} respectively.

1.2.1 Short-circuit Current Density

The short-circuit current density, J_{SC}, is the current through the solar cells when V = 0, which is a similar condition as the two electrodes of the cell being short-circuited together. Because V= 0, and power is the product of current and voltage, no power is generated at this point but J_{sc} marks the onset of power generation. J_{sc} of a solar cell depends on the photon flux density incident on the cell, which is determined by the spectrum of the incident light. The optimum current that the solar cell can deliver strongly depends on the optical properties such as absorption in the absorber layer and total reflection of the solar cell.

1.2.2 Open-circuit Voltage

The open-circuit voltage, V_{OC}, is the voltage at which no current flows across the solar cell, which is the same as the device being open-circuited. This is the maximum voltage that a cell can deliver. Since J= 0 there is no power produced at this point but it marks the boundary for voltages at which power can be produced. The Voc corresponds to the amount of forward bias voltage at which the dark current compensates the photo-current in the solar cell. The V_{OC} can be calculated from an equation given below by assuming that the net current is zero.

$$V_{OC} = \frac{AkT}{q} ln\left(\frac{J_{ph}}{J_o} + 1\right) \quad (1.2)$$

Where kT/q is the thermal voltage, J_{ph} is the photocurrent density and Jo is the dark saturation current.

The above equation shows that V_{OC} depends on the saturation current and light generated current in the solar cell. Since J_{ph} has a small variation, the key effect on V_{OC} is the saturation current, which may vary by orders of magnitude. The saturation current density, Jo, depends on the recombination in the solar cell so V_{oc} is a good measure of the amount of recombination in the cell.

1.2.3 Fill Factor

The fill factor is defined as the ratio of the maximum power (P_{max} = J_{mp} x V_{mp}) generated by a solar cells to the product of V_{oc} and J_{sc}.

$$FF = \frac{J_{mp}V_{mp}}{J_{sc}V_{oc}} \quad (1.3)$$

It is an indication of how close J_{mp} and V_{mp} come to the boundaries of power generation of J_{sc} and V_{oc}. It is also an indication of the sharpness of the J-V curve that connects J_{sc} and

V_{oc}. High FF is always desired since this is the indication of higher maximum power but the diode-like behavior of solar cells results in FF always being less than one.

1.2.4 Power Conversion Efficiency

The most commonly used parameters to compare the performance of a solar cell is the power conversion efficiency which is defined as the ratio of energy output from the solar cells to input energy from the sun. The efficiency of a solar cell is determined as

$$\eta = \frac{P_{max}}{P_{in}} = \frac{J_{mp}V_{mp}}{P_{in}} = \frac{V_{OC}J_{SC}FF}{P_{in}} \tag{1.4}$$

The above equation clearly shows that FF, J_{sc}, and V_{oc} all have direct effects on η. Since the area used to calculate J will affect the efficiency of the cell, the inactive areas such as grids, and interconnects should be included while calculating the efficiency for large area devices or modules. The efficiency of the solar cells is also very dependent on the power and spectrum of the incident light source and the temperature of the solar cell, since the solar cells do not absorb and convert photons to electrons at all wavelengths with the same efficiency. So all the conditions under which the conversion efficiency of the cell is measured should be carefully controlled in order to compare various solar cells. Even though the solar spectrum at the earth's surface varies with location, cloud coverage, and other factors, the AM1.5 G spectrum as shown in Figure 1.2 is the most commonly used standard spectrum for measuring and comparing the performance of photovoltaic devices. The term air mass intensity (AM) is usually used to denote the ratio of the optical path to a normal path at sea level on a cloudless day and the expression for it is given as

$$AM = \frac{1}{Cos\theta} \tag{1.5}$$

Where θ is the angle of the path Sun light travels with respect to the vertical. If θ is 48.19 ^{0} then AM condition is called AM 1.5 (AM=1/Cos (48.19) = 1.5). So the AM 1.5 is equivalent to the sunlight passing through 1.5 times the air mass of vertical illumination (AM 1).

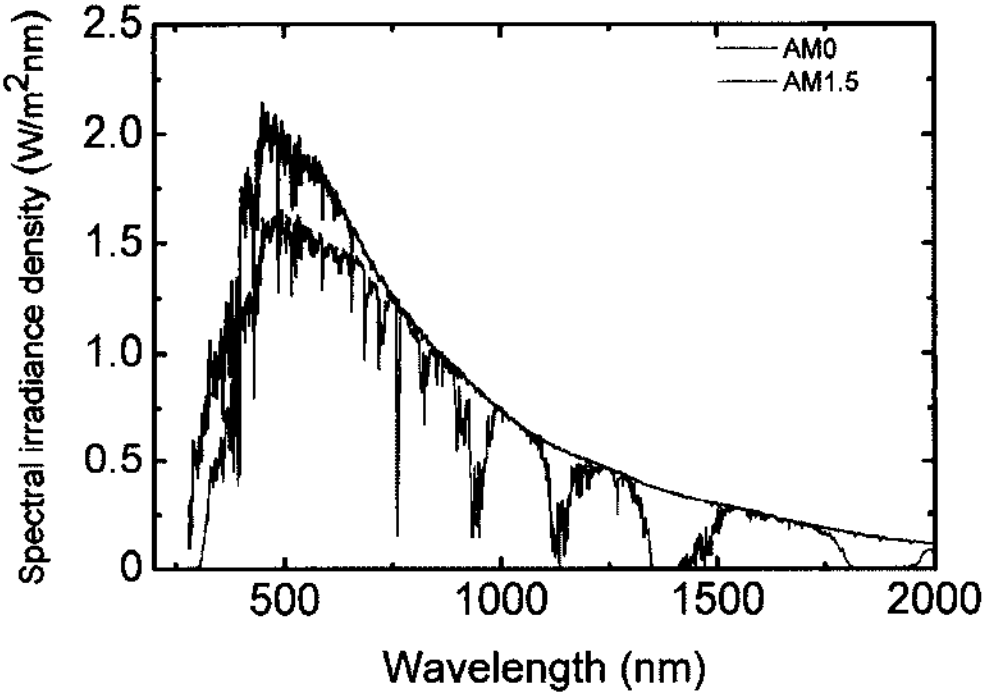

Figure 1.2: Comparison of spectral irradiation densities: AM0 irradiation (blue), and AM1.5 irradiation (red).

1.2.4 Practical Requirements from a Solar Cell Material

There are various materials, which exhibit the photovoltaic effect and can be considered for the solar cell production. However, materials for efficient solar cells needs to satisfy numerous requirements such as i) materials for practical PV application must have characteristics matched to the spectrum of the available light, ii) the materials needs to be inexpensive, non-toxic and available in large quantity, iii) the PV device production

method should be fast, inexpensive and environmental friendly and iv) the PV device performance must be stable for outdoor application for extended periods of time.

1.3 Overview of Progress in Photovoltaic (PV) Technology

1.3.1 Introduction

The history of solar energy is not new. We started to utilize the sun's energy to convert into electricity in the last two centuries. In 1839, Alexandre-Edmond Becquerel discovered the photovoltaic effect. He observed that he could produce an electric current by exposing two metal electrodes placed in conducting solution to light. In 1873, the photo-conductivity of solid selenium was discovered by Willoughby Smith [12]. In the 1950s, a silicon photovoltaic cell with efficiency around 6 % was developed at Bell Laboratories by Calvin Fuller, Daryl Chapin, and Gerald Pearson [13]. Since then, due to advancement in the technology, semiconductor based devices are developed to make more efficient solar cells which are classified into three generations known as First generation, Second generation and Third generation photovoltaic technology.

1.3.2 First Generation PV

First generation photovoltaic cells are single junction solar cells based on silicon wafers, including single crystal (c-Si) and multi-crystalline silicon (mc-Si), as well as on GaAs. The silicon cells and modules are the dominant technology on the solar cell market, accounting for more than 86% of the solar cell production. But manufacturing cost is the major challenge because of the high purity materials requirement to avoid recombination issues, even though much progress has been done in the last 5 years with module costs now

reduced to below $0.8/W. These c-Si and mc-Si semiconductors, used in commercial production, allow power conversion efficiencies up to 25%, even though the fabrication technologies at present limit them to about 15 to 20% [14]. C-Si has an indirect band gap of ~ 1.17 eV, which has the following problems: it absorbs sunlight poorly and needs relatively thick layers in the order of hundred micro-meters to absorb most of the incident light. GaAs, on another hand, is a direct band gap material with zinc blende crystal structure. Its band gap can be tuned by varying the group III element or the group V element. GaAs based solar cells hold the highest conversion efficiencies (30 % for single-junction and 40% for multi-junction solar cell). However, the fabrication cost of these devices is very high because of the high purity requirement. The GaAs solar cells are mainly fabricated using molecular beam epitaxy (MBE) or metal-organic chemical vapor deposition (MOCVD), which are very expensive deposition techniques. This is the main reason this technology is currently limited to space applications like satellite and space station solar cells. The second generation technology has the advantage because of being more forgiving during the deposition process.

1.3.3 Second Generation PV

In order to fulfill the requirement of lower cost and improved manufacturability at large scale, a second generation PV, also called thin films PV, has been developed. There are basically three types of solar cells that are considered in this generation: Cadmium Telluride (CdTe), Copper indium gallium diselenide (CIGS) and amorphous silicon (a-Si). These thin films absorb the solar spectrum much more efficiently than c-Si or mc-Si and use only a couple of microns of active materials. They also offer a way to increase the unit

of manufacturing by 100 times from first generation PV i.e. Silicon wafer (~ 100 cm^2) to a glass sheet (~ 1 m^2) [15]. The recorded efficiency of CIGS (21.7%) [5] and CdTe (20.8 %) [14] have provided ample evidence of the potential of thin-film PV. Although the expansion of 2nd generation of PV is getting slower than expected, it still has greater potential to bring down the production cost of PV in large scale production by reducing material usage and production costs.

1.3.4 Third Generation PV

The primary approach of 3rd generation PV is to reduce the PV costs further below the level of 2nd generation PV by increasing the efficiency while keeping the almost similar advantage of thin film deposition technique. In order to achieve such efficiency improvements, PV technology is seeking to overcome the Shockley-Quesser limit of 31-41% efficiency for single-band gap devices [16]. The inability to absorb incident light with energy less than the band gap and thermalization of light energies exceeding the band gap are the main important power-loss mechanism in single band gap cells. These two power loss mechanism can potentially be addressed by designing a series of new device structure based on innovative technologies. These new devices include multi-junction/tandem cells, quantum dot cells, intermediate band solar cells, hot-carrier cells and non-semiconductor cells such as organic photovoltaic, polymer solar cells, and dye-sensitized solar cells. A new concept in PV based on 'inorganics-organics' offers improved solar efficiency in comparison to third generation PV. The hybrid active materials which is the combination of the low cost and conducting polymers films (organic) and the life time stability of novel nano-structure (inorganic) improves the harvesting cross-section, the charge dissociation

and charge transport within the PV devices [10]. These new devices include mainly carbon nanostructures, mNPs, metal oxides and nano-hybrids.

1.4 Thesis Objectives and Organization

Many technology options exist nowadays to harvest the power of the sun, a sustainable energy source, and generate electricity directly from this source via the photovoltaic effect. Among them, $Cu(In,Ga)Se_2$ has gained significant momentum as a possible high efficiency and low cost thin film solar cell material. With 21.7% efficiency, $Cu(In,Ga)Se_2$ (CIGS) solar cells are the most efficient polycrystalline thin films solar cells today. The capacity to scale up any photovoltaic technology is one of the criteria that will determine its long term viability. However, as CIGS technology continues to increase its share of the market, the scarcity and high price of indium will potentially affect its ability to compete with other technologies. One way to avoid this bottleneck is to reduce the importance of indium in the fabrication of the cell simply by reducing its thickness without significant efficiency loss. Reducing the thickness of $Cu(In,Ga)Se_2$ thin film will not only save the material but will also lower the production time and the power needed to produce the cell. Even though $Cu(In,Ga)Se_2$ thin film solar cells are an excellent candidate for the renewable energy production with competitive prices, the knowledge of device physics especially in ultrathin devices is still incomplete. The main objective of this work is to understand the optical and electrical properties of ultra-thin $Cu(In,Ga)Se_2$ as a function of process and composition, and to use that knowledge to enhance the efficiency of such devices. To better understand the optical properties of ultra-thin $Cu(In,Ga)Se_2$ as a function of process and other deposition conditions, real time spectroscopic ellipsometry (RTSE) can be used as a

suitable *in*-situ sensor to monitor the thickness, roughness, optical properties, and growth temperature.

Before starting the ultra-thin CIGS deposition, the following items are the critical parameters and problems to consider:

- Highly efficient ultra-thin Cu(In,Ga)Se_2 devices are fabricated from slightly Cu-poor Cu(In,Ga)Se_2 thin films with band gap around 1.15 eV.
- The efficiency of the cell reduces if the Cu at.% in the ultra-thin Cu(In,Ga)Se_2 thin film is too low, while Cu-rich films result in shunted devices.
- For optimum quality, ultrathin Cu(In,Ga)Se_2 films are deposited by 2-stage and 3-stage co-evaporation process, which involves Cu-rich to Cu-poor transitions.
- Reduce light absorption will reduce the photocurrent.
- The impact of back surface recombination can increase.

We will therefore perform *in-situ* monitoring of high quality ultra-thin Cu(In,Ga)Se_2 film to understand the optical and electrical properties of the films as a function process and thickness.

In Chapter 2, materials properties of Cu(In,Ga)Se_2 thin films and characterization techniques used to explore the Cu(In,Ga)Se_2 thin films and devices are presented.

In Chapter 3, the effect of absorber thickness on ultra-thin CIGS films and devices are discussed. Chapter 3 also includes the numerical simulation results to analyze the experimental results for ultrathin CIGS solar cells.

In Chapter 4, characterization of ultra-thin CIGS films deposited by 1-stage, 2-stage and 3-stage process are presented. Chapter 4 also provides an overview of the effect of selenium pressure on ultrathin CIGS films and devices.

In Chapter 5, characterizations of ultra-thin CIGS films deposition using in-situ spectroscopic ellipsometry are discussed.

In Chapter 6, advances in CIGS fabrication processes are discussed.

In the final chapter, a summary and conclusion of the work presented here will be given. This chapter also discusses future works and goals for further improvement of the PV device quality.

CHAPTER 2

$Cu(In,Ga)Se_2$ SOLAR CELL: MATERIAL PROPERTIES AND CHARACTERIZATION METHODS

2.1 $Cu(In,Ga)Se_2$ Material Properties

2.1.1 Introduction

The history of $CuInSe_2$ (CIS) solar cells starts with the invention of CIS solar cells in Bell Laboratories in the early 1970s. No real effort was given to these devices until Boeing demonstrated the first high efficiency (9.4%) device in 1981 [17]. At the same time, CuS_2 was being explored as a thin film solar cell but had electrochemical instabilities problems. Since then, research on CuS_2 has almost stopped but CIS progressed continuously. Now $Cu(In,Ga)Se_2$ (CIGS) solar cells deposited by three-stage process have achieved above 20 % energy conversion efficiency, which is the highest record for thin film polycrystalline solar cells [5].

2.1.2 Structural and Compositional Properties

$Cu(In,Ga)Se_2$ forms a quaternary compound when Gallium (Ga) atoms partially substitute Indium (In) atoms in $CuInSe_2$ ternary system. The CIGS has a chalcopyrite tetragonal structure, which is similar to that of the $CuInSe_2$ structure as shown in Figure 2.1. The tetragonal structure of the chalcopyrite compound can be considered as a super lattice Zinc Blende structure by elongating the unit cube along the z-axis twice the length that becomes the c-axis of the chalcopyrite structure [18]. The ratio of the tetragonal lattice

parameters c/a, which is called tetragonal deformation, is close to 2 and varies due to the difference in bond strength in Cu-Se, In-Se or Ga-Se. So, the c/a ratio is a function of $x \equiv Ga/(In+Ga)$, where $c/a>2$ for $x = 0$ and $c/a<2$ for $x = 1$.

CIGS can be either p-type or n-type depending on the dominant defects. Usually, n-type CIGS is grown under Cu-rich and Se-deficient environment whereas p-type CIGS is grown under Cu-poor and Se-rich environment [19]. Thus Se vacancy (V_{Se}) and Cu vacancy (V_{Cu}) are believed to be the dominant defects in n- and p-type CIGS respectively [19]. P-type CIGS thin films are used as absorber layers in solar cell application.

Figure 2.2 (a) shows the ternary phase diagram with possible phases in the Cu-In-Se system. The pseudo-binary In_2Se_3-Cu_2Se equilibrium phase diagram, which is derived from the Cu-In-Se ternary system, is shown in Figure 2.2 (b). In the phase diagram, α is the chalcopyrite CuInSe2 phase, δ is a high-temperature phase and β is an ordered defect compound phase (ODC). The α phase is the most important phase in the Cu-In-Se system for high efficient CIGS solar cell. It can be clearly seen that the single phase field for CuInSe2 at low temperature is narrower than at higher temperature, and becomes maximum around 6000C. So the best suited growth temperature for CIGS thin film is around 600^0C. The average copper (Cu) compositions of high quality CIGS films deposited at high temperature is 22-24 at%, which lie within the single phase region.

CIGS is formed by alloying $CuInSe_2$ in any proportion with $CuGaSe_2$. In high performance CIGS cell, the Ga/(In+Ga) and the Cu/(In+Ga) ratios are typically 0.2-0.3 and 0.7-1, respectively. There is the possibility of high defect density in the Cu-poor film but these defect densities should be reasonably low and electronically inactive to avoid adverse effects on solar cells performance [20]. At the Cu-poor boundary, the α-phase coexists with

the β-phase, which represents a number of ODC like $CuIn_3Se_5$, $CuIn_5Se_8$ etc. The addition of Ga or Na suppresses the formation of ordered defect compounds [20] and thus widens the α-phase towards the Cu poor boundary. Thus, these provide slightly more freedom in terms of deposition conditions.

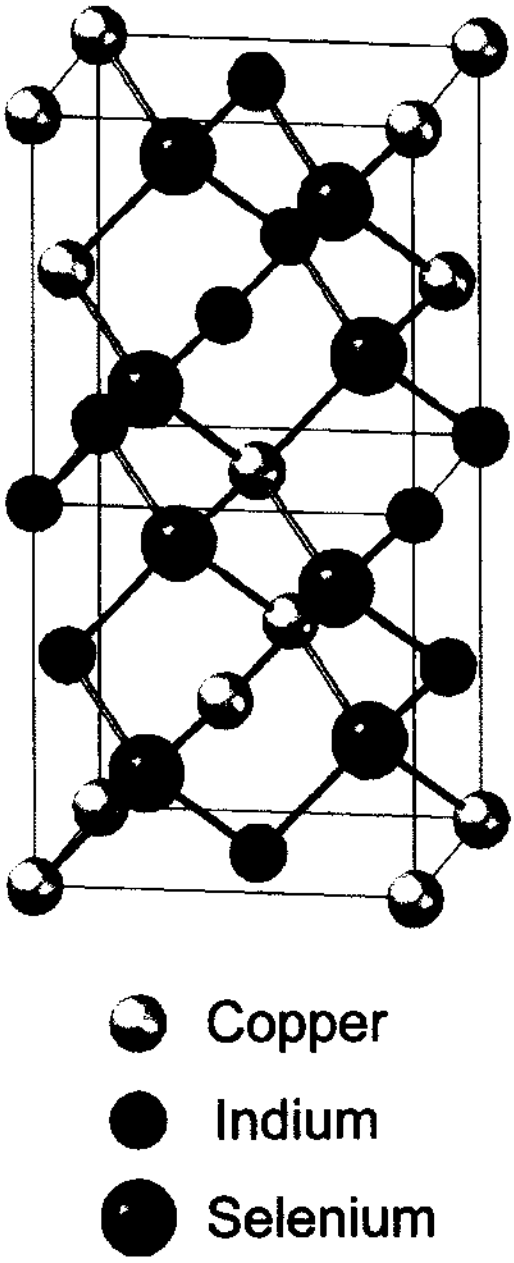

Figure 2.1 Chalcopyrite crystal structures of CIGS [after 21]

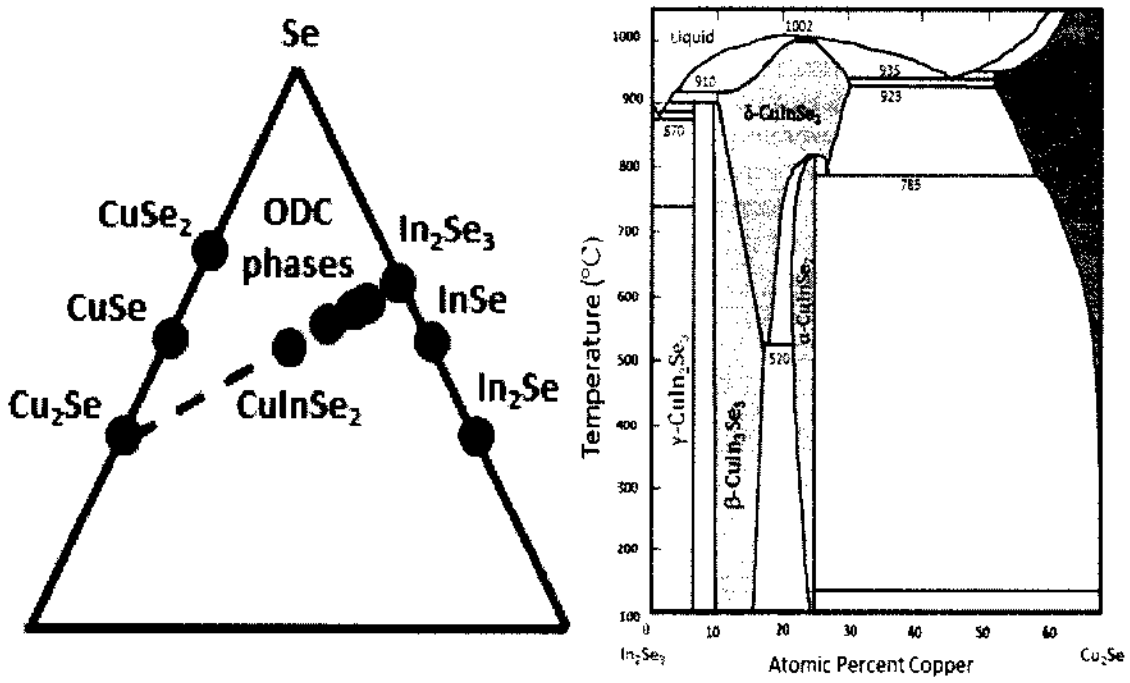

Figure 2.2 (a) Ternary phase diagram of Cu-In-Se system [after 17] and (b) pseudo-binary phase diagram [after 21].

2.1.3 Optical Properties and Band Gap Grading

CIGS films have very high absorption coefficient, with values larger than 10^5 cm^{-1} for 1.5 eV and higher energy photons [22]. So, only a few micrometer thick CIGS film is needed to absorb most of the incident light. The absorption coefficient, α, can be calculated from the transmission and reflection coefficients using the following expression [23]:

$$\alpha = \frac{2\ln(1-R) - \ln(T)}{d} \tag{2.1}$$

Where d is the thickness of the thin film, R is the reflection and T is the transmission. Since CIGS is a direct gap semiconductor, the absorption coefficient in the region of strong absorption obeys the following equation

$$\alpha = \frac{A}{h\upsilon}(h\upsilon - E_g)^{1/2} \tag{2.2}$$

Where h is the Planck constant, ν is the radiation frequency, E_g is the band gap energy and A is a constant, which depends on the nature of the radiation. The extrapolation of the linear portion of the $(\alpha h\nu)^2$ versus hν graph at $h\nu = 0$ gives therefore the band gap value of the material. $Cu(In,Ga)Se_2$ has a tunable band gap that varies with x = Ga/(In+Ga). The relation between the E_g and x can be expressed by the following empirical formula [24]:

$$E_g = (1-x)E_g(CIS) + xE_g(CGS) - bx(1-x) \tag{2.3}$$

Where E_g(CIS) is 1.04 eV, the band gap of $CuInSe_2$; E_g(CGS) is 1.68 eV, the band gap of $CuGaSe_2$; and b is the bowing parameter that depends on the growth. The most reproducible values of b are around 0.15–0.24 eV [24]. The Ga content in the $Cu(In,Ga)Se_2$ thin film affects the band-gap primarily in the conduction band. The band gap of $Cu(In,Ga)Se_2$ increases with increasing Ga content by shifting the conduction band position [24]. So, with an appropriate spatial variation of Ga in the $Cu(In,Ga)Se_2$, various band gap profiles can be achieved as shown in Figure 2.3. Introducing a higher Ga/(In+Ga) ratio near the front surface (Space charge region) and at the back surface region of $Cu(In,Ga)Se_2$ film will increase the band gap locally. The increase in the band gap, ΔE_g, creates an additional electric field, which is also called quasi electrical field [25]. The Ga-gradient in the space charge region (SRC) and at the back surface improves J_{sc} performance due to the additional force created that increases the carrier collection. The back surface recombination can be reduced significantly due to the back surface grading, which also enhances the voltage by reducing recombination. The SCR grading as an addition to the back surface grading also increases the device voltage since the voltage is also determined

by the band gap in the space charge region. In general, a proper band-gap grading in the SCR and back surface are capable of significantly improving the device performance.

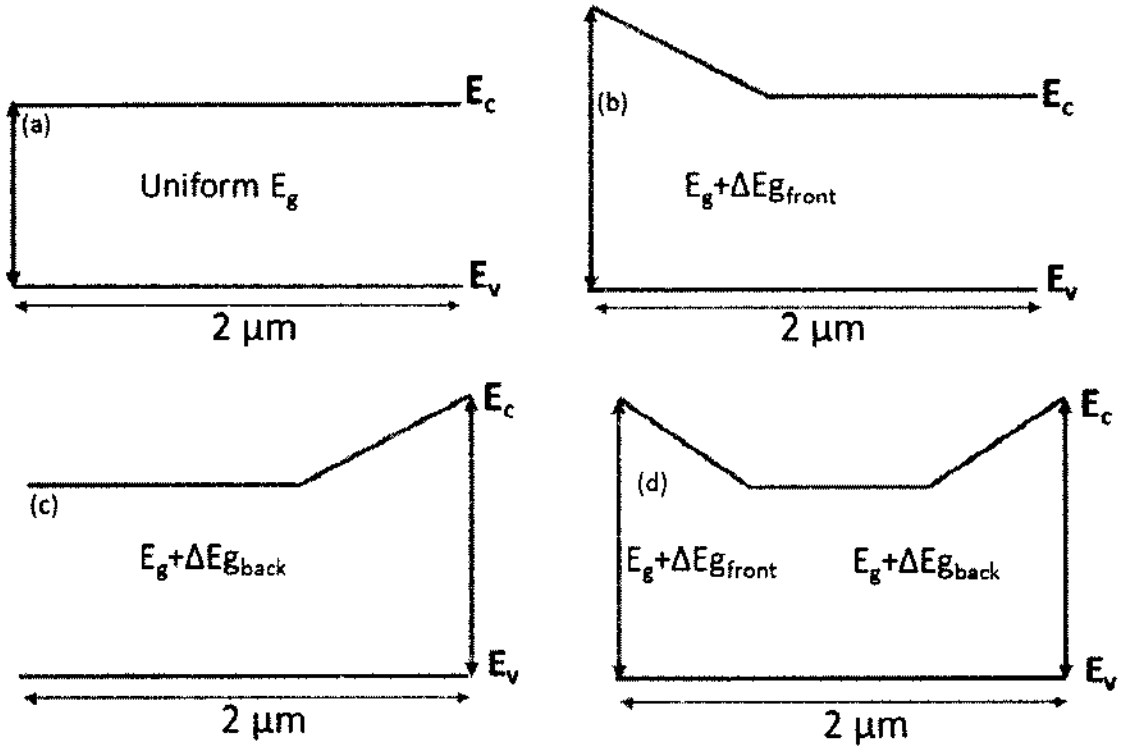

Figure 2.3 Different types of absorber band gap profiles. (a) Uniform band gap (b) Front grading (Space charge region grading) (c) back surface grading (d) Double grading.

2.2 Materials and Devices Characterization

CIGS thin films and devices were analyzed in-situ, in real time or ex-situ via different types of characterization techniques. The outcomes from these techniques were then corroborated to get a complete understanding of the materials and devices properties.

2.2.1 X-ray Fluorescence (XRF)

X-ray fluorescence (XRF) is a non-destructive, powerful analytical technique to identify and determine the elemental composition of a material. This technique can be used to determine most of the elements in the periodic table from boron (B) to uranium (Ur) in the range of part per million (ppm) to 100%. The working principle consists of bombarding a sample with primary X-rays that causes the constituent atom to be energized, so that individual electrons move out of their normal positions and into orbitals further from the central nucleus. When the atom returns back to its stable state, the electrons drop back into their inner orbits and give off their excess energy in the form of characteristic secondary X-rays (fluorescence) whose energy is the difference between the two binding energies of the corresponding shells. By measuring the energies of the characteristic secondary X-rays, and counting the number of X-rays of each energy, XRF allows identifying which elements are present in a sample and also determining the relative concentration of these elements within the sample. In most cases, the innermost K and L shells are involved in XRF detection. A typical x-ray spectrum from an irradiated sample will display multiple peaks of different intensities as shown in Figure 2.4 below. XRF can also be used for thickness measurement, for films that are not thicker than the penetration depth of radiation.

The composition and thickness of CIGS thin films were measured using XRF to make sure that no processing was done on cells that would not work, by checking the Cu/(In+Ga) ratio and the Ga/(In+Ga) ratio.

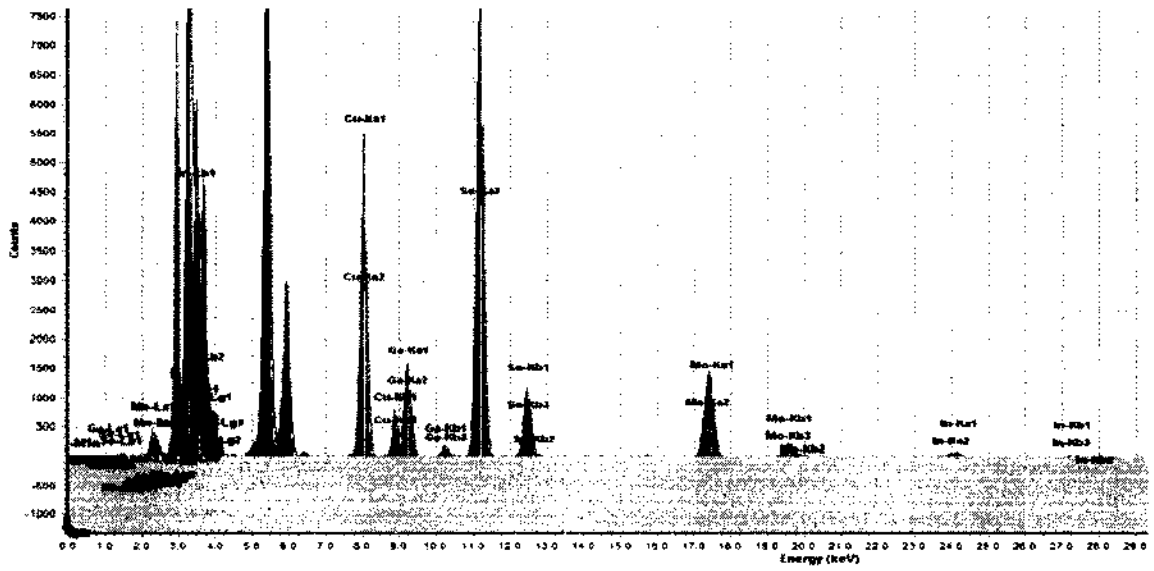

Figure 2.4 XRF Spectrum taken using Solar Metrology System SMX with 2 mm beam and 60k HV

2.2.2 X-ray Diffraction (XRD)

X-ray diffraction is a rapid analytical technique used to probe the crystalline phases present in materials and to measure the structural properties such as grain size, preferred orientation and defect structure of the phases. When a collimated beam of X-rays is directed at the sample surface, the material of the sample causes the X-rays to be diffracted at various angles based on its crystal structure. The diffraction spectrum of the samples is then plotted as a function of 2θ. When Bragg's law ($2d \sin\theta = n\lambda$) is satisfied, diffraction peaks appear. The diffraction angle, the number of peaks and their intensity depend on the crystal structure, symmetry and lattice constant. Comparing the peaks with XRD database gives the phase, crystal orientation, lattice constants and other information. The inter-planar spacing, d_{hkl}, corresponding to each diffraction line, is calculated by the following equation:

$$d_{hlk} = \frac{\lambda}{2Sin\theta} \tag{2.4}$$

Where θ is Bragg's angle of diffraction and λ is the wavelength of the X-rays radiation. XRD data can also be used to predict the crystallites size using Scherrer formula [26].

$$L = \frac{K_s \lambda}{\beta \cos\theta} \tag{2.5}$$

Where L is the grain size, K_s is Scherrer constant (usually set at 0.9 for spherical particles), β is the full width at half maximum of the peak in radians, λ is the wavelength of the X-ray beam and 2θ is the peak position.

The X-rays penetration depth can be varied by varying the angle of incidence of the x-rays beam. With a bigger angle it is possible to see the material composition deeper into the sample. For $Cu(In,Ga)Se_2$ compounds, since the lattice parameters for different Ga/(In+Ga) are already known, XRD can also be used to find the Ga/(In+Ga) value in the film. Sometimes, it is not desired to probe deeply into the film or not possible to get a good signal if the film is too thin. To counteract this, grazing incident XRD (GIXRD) can be used. This is basically a low angle XRD, which changes the penetration depth of the X-ray by fixing the incident angle from 1 to 10 degrees while moving the detecting arm.

2.2.3 Atomic Force Microscopy (AFM)

AFM is one type of scanning probe microscopes, which is used to obtain surface structures images (on an nm or even sub-nm scale) and other information. In AFM, a probe is maintained in close contact with the sample surface by a feedback mechanism as it scans over the surface, and the movement of the probe to stay at the same probe-sample distance

is taken to be the sample topography. Generally a cantilever made of Si or SiN is used to probe the surface of the sample by adjusting the position via control implementations. The tip of the cantilever is kept in continuous or intermittent contact with the sample surface and the cantilever is translated over the sample using a piezocontroller. A laser is reflected on the back surface of the cantilever as a scan is in progress. Whenever the laser changes its positions due to force on the cantilever, a voltage is applied to the piezoelectric to make the laser go back to its origin. The voltage corresponds to the height of surface features, since the force on the cantilever is caused by the features on the specimen. A precise calibration between the height and the voltage is accomplished by using a sample with known structure. AFM can be used in three main different modes of imaging depending on the interaction of the surface and the tip. In contact mode, the tip of the AFM probe is always kept in contact with the surface whereas the tip never touches the sample in non-contact mode measurement. During contact with the sample, the probe predominately experiences repulsive Van der Waals forces. As the tip moves further away from the surface (non-contact mode) attractive Van der Waals forces are dominant. Contact mode AFM is good for rough samples but it damages soft surfaces whereas the non-contact mode has bad resolution and usually needs ultra-high vacuum (UHV) to have best imaging. In tapping mode, the imaging is similar to contact mode however in this mode, the cantilever is oscillated at its resonant frequency via the piezoelectric crystal attached to the tip holder. During the oscillation, the probe tip keeps moving towards the surface till it lightly taps on the surface. As soon as there is contact between the tip and the surface, there is loss in the oscillation amplitude, which is used to find the topographic changes. This technique allows high resolution and is good for soft surface.

2.2.4 Mass Spectrometer

The mass spectrometer is a powerful analytical instrument which can be used to quantify known materials, to identify unknown compounds within a sample, and to elucidate the structure and chemical properties of different molecules. This is essentially a technique for "weighing" molecules. It works on the principle that ions can be separated by mass while moving through a magnetic field. The first step in the mass spectrometric analysis of compounds is the production of gas phase ions of the compound, basically by electron ionization. The ions are separated in the mass spectrometer according to their mass-to-charge ratio, and are detected in proportion to their abundance. A mass spectrum of the molecule is thus produced. It displays the result in the form of a plot of ion abundance versus mass-to-charge ratio. Thus, the complete process involves the conversion of the sample into gaseous ions, with or without fragmentation, which are then characterized by their mass to charge ratios (m/z) and relative abundances. The mass spectrometer consists of four major components i) a sample inlet ii) ion source iii) analyzer iv) detector system. Samples molecules are introduced into the instrument through a sample inlet and these molecules are converted to ions in the ionization source before being electrostatically propelled into the mass analyzer. Ions are then separated according to their *m/z* within the mass analyzer. The detector converts the ion energy into electrical signals, which are then transmitted to a computer. It provides a real time, in situ, no-contact, and non-intrusive process sensor for CIGS co-evaporation and is being used to monitor the evaporation rate of multiple elements (Cu, In, Ga and Se) in the system as shown in Figure 2.5 below.

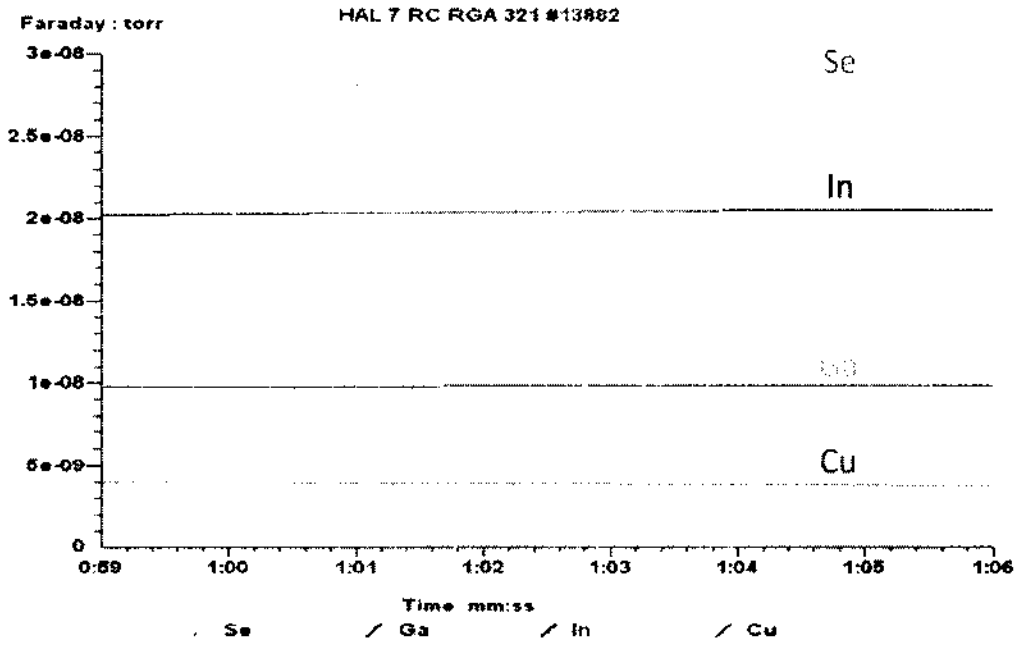

Figure 2.5 Partial pressure of copper (Cu), indium (In), gallium (Ga) and Selenium (Se) using mass spectrometer

2.2.5 Hall Effect Measurement

A Hall effect measurement system is used to measure electrical properties such as carrier concentration (n), carrier mobility (μ), resistivity (ρ), conductivity type (n or p), Hall voltage (V_H), Hall coefficient (R_H). When a current carrying conductor or semiconductor is kept in a magnetic field, a force perpendicular to both current and magnetic field, known as the Lorentz force, is experienced by the charge carrier. The Hall effect is the result of using this force to determine the magnitude and sign (n-type or p-type) of this force. When a magnetic field with a perpendicular component is applied, the paths of the charge carriers are curved so that moving charges accumulate on one side of the material. Equal and opposite charges remain on the opposite side of the material and a voltage can be measured from the charge density difference at equilibrium. During the

measurement, a sample is mounted in the van der Pauw configuration where electrodes are attached (generally soldered for a good ohmic contact) at four opposite corners. In this configuration the sheet resistance can be found, and with a magnetic field applied the charge carrier density and sign can be found.

2.2.6 Secondary Ion Mass Spectroscopy (SIMS)

Secondary ion mass spectroscopy (SIMS) is a high sensitivity surface analysis technique used to determine the surface composition, elemental impurities and depth profile on the uppermost surface layers of a sample. SIMS uses a primary ion beam, such as an Ar or Cs ion, and sends it on the surface of the sample. Ions ejected from the material of the sample are known as secondary ions. These secondary ions are then analyzed by a mass/charge analyzer using the atomic mass values. Depending upon the polarity of the sample, positive or negative secondary ions will be extracted. SIMS is a highly sensitive surface scan analysis measuring atoms in the ppm or ppb range and capable of monolayer analysis. The type of mass spectrometer employed by SIMS depends on the operating mode of the SIMS. Static and dynamic SIMS is being used in the field of surface analysis. Static SIMS is capable of analyzing the surface of an atomic monolayer by using a pulsed ion beam and a time of flight mass spectrometer while dynamic mode sputters the material of the sample using a DC primary ion beam and measuring with a quadruple or magnetic sector mass spectrometer. In this study, a dynamic SIMS analysis was used to find the impurities in the solar cell stack as well as to find the composition of the absorber layers.

2.2.7 Transmission and Reflection Measurements

The most common method of determining the band gap of a semiconductor is by transmission and reflection measurement. The transmission and reflection coefficients of the semiconductors are normally measured in the wavelength range from 200-2500 nm. Then the absorption coefficient can be calculated from transmission and reflection coefficients using the relation [23]:

$$\alpha = \frac{2\ln(1-R) - \ln(T)}{d} \tag{2.6}$$

Where α is the absorption coefficient, d is thickness of the thin film, R is the reflection and T is the transmission. Once α is calculated, then the band gap of any direct band gap semiconductors can be extracted by plotting $(\alpha h\upsilon)^2$ vs. hυ and by extrapolating the linear portion of the curve to the hυ axis. The intersection of this linear extrapolation with the hυ axis gives the band gap.

2.2.8 Energy Dispersive X-ray Spectroscopy (EDS)

Energy dispersive X–ray spectroscopy (EDS) is an analytical technique used to find the elemental composition of materials down to a spot size of a few microns. It relies on the emission of X-rays as a result of interaction of the material with the high energy radiation at atomic level. An electron from the lower energy state is ejected due to the bombardment of high energetic beam from the electron source and the atom goes to an excited state. The electron from the excited state falls back to the vacant state by releasing

energy in the form of X-rays. Since the atomic structure of an element distinguishes it from another element, this emitted X-ray is characteristic of the element. An energy-dispersive (EDS) detector is used to separate the characteristic x-rays of different elements into an energy spectrum, and EDS system software is used to analyze the energy spectrum in order to determine the abundance of specific elements in the sample.

2.2.9 Auger Electron Spectroscopy (AES)

Auger Electron Spectroscopy (AES) is an analytical technique used in the study of surfaces of composition analysis and can be used for depth profile of the composite material in combination with a sputtering gun, where sputtering is used to remove the outer layers. The basic Auger process begins with removal of an inner shell atomic electron to form a vacancy by bombarding with an electron beam. The inner shell vacancy is filled by a *second* atomic electron from a higher shell by releasing the excess energy. A *third* electron, the Auger electron, escapes carrying the excess energy in a radiationless process. The process of an excited ion decaying into a doubly charged ion by ejection of an electron is called the Auger process. The kinetic energy of the emitted electrons is measured and the signal is proportional to the number of atoms sampled. The kinetic energy of the Auger electron from an ABC transition can be estimated as [23]:

$$E_{ABC} = E_A(Z) - E_B(Z) - E_C(Z+\Delta) - q\phi \qquad (2.7)$$

where E_{ABC} is the kinetic energy of the finally ejected electron, $E_{i=A,B,C}$ is the binding energy of electron in i^{th} orbit, Z is the atomic number of ionized state and Δ is the factor

that take into account the binding energy of the C orbit due to the ionized atom. Auger electrons can only escape from the outer 5-50 Å of a solid surface at their characteristic energy, which makes it an extremely surface sensitive technique.

2.2.10 Scanning Electron Microscopy (SEM)

Scanning electron microscopy utilizes high-energy electron beam in a raster-scan pattern to produce a highly magnified image or collect other signals from the three-dimensional surface of a sample. An SEM consists of an electron gun, an electron lens system, scanning coils, an electron collector, electron detectors, display and recording devices. In SEM, larger magnifications are possible over optical microscopes since electron wavelengths are much smaller than photon wavelength and a large field of view is possible since the electron beam is small, which allows three-dimensional study of a specimen's surface. As an operation principle of a SEM, the focused electrons interact with the atoms in the specimen producing a number of different types of signals, which contains data about the specimen's surface morphology, composition, and other physical and chemical properties. The induced signals by an SEM include secondary electrons, back-scattered electrons (BSE), characteristic X-rays, photons as well as specimen current and transmitted electrons. Electron with energies 0-30 eV are detected and used to form the image in secondary electron mode. These electrons are knocked out from within a few nanometers of the surface of the specimen. Backscattered electrons are electrons from the electron beam that are elastically scattered back from the sample and provides the

information about the bulk properties of the materials since such scattering takes place in a volume extending down to 0.5 μm below the surface of the specimen.

2.2.11 Spectroscopic Ellipsometry measurement

Spectroscopic Ellipsometry is an optical tool that uses polarized light for the investigation of the dielectric properties of specimens, from which more indirect parameters such as growth or structural parameters can be derived. It measures a change in polarization as light reflects or transmits from samples. Because it uses the polarization state as a probe rather than only the intensity of the photon itself, it is a very sensitive measurement technique. It routinely generates information about layers that are thinner than the wavelength of the probing light itself and theoretically down to a single atomic layer. The detail theory of the Ellipsometry is explained in Chapter 5.

2.2.12 Current Density vs. Voltage

The standard J-V measurement is performed under a standardized "1-sun" (AM 1.5) illumination at room temperature. The solar cell is placed under the light source, minimizing the distance to the center of the light. Two electrical probes are placed on the p-type and n-type sides. Dark measurement is performed without light source while the illuminated measurement is performed with the light source on. The measurements results are collected by a highly sensitive and accurate multimeter and sent to a computer, where all the data is stored in current (I) and voltage (V) pairs. The current density (J) is calculated

after knowing the illuminated area of the sample. Thus J-V data will be obtained. This J-V measurement data helps not only in finding efficiency, fill factor, J_{sc}, V_{oc} but also helps in finding the shunt resistance, series resistance and the voltage dependent current collection. The current density in a real solar cell is written as [27].

$$J = J_0 \exp\left[\frac{q}{AKT}(V - R_s J)\right] - J_0 + \frac{V - R_s J}{R_{sh}} - J_L \qquad (2.8)$$

where A is the ideality factor, R_s is the series resistance and R_{sh} is the shunt resistance of the solar cell. An equivalent circuit of a solar cell with these parasitic resistances is shown in Figure 2.6 below.

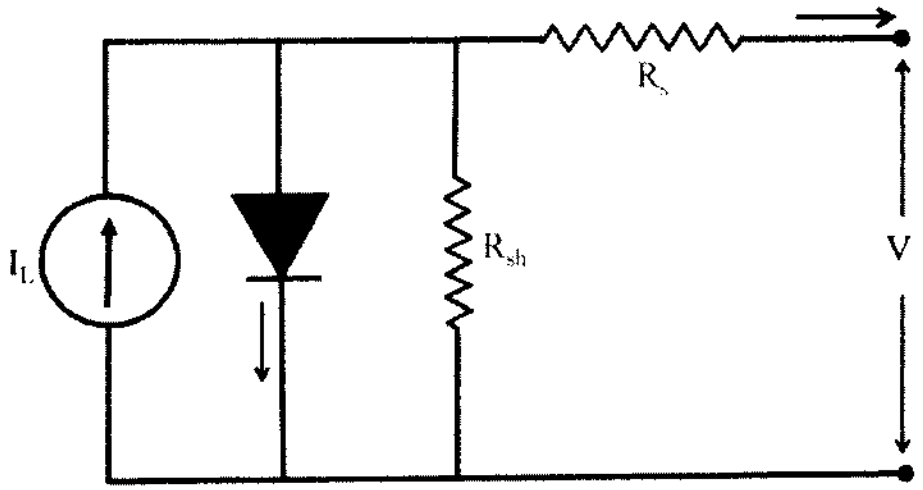

Figure 2.6 An equivalent circuit of a solar cell.

The series resistance R_s of a solar cell is not only due to the bulk resistance of the individual thin film of the cell stack but also to the resistance of the semiconductor- metal contacts and the bulk resistance of the metal contact. The series resistance can be determined from equation 2.8 by plotting $\frac{dV}{dJ} = R_s + \frac{AkT}{q}(J + J_L)^{-1}$ versus $(J + J_L)^{-1}$

under the condition that R_{sh} is infinitely high. This plot intercepts y axis at a value of R_s and the slope of the linear region allows identification of A. The effect of increase in the R_s is reflected by the decrease in the steepness of the I-V curve as shown in Figure 2.7. I_{sc} and V_{oc} remain almost the same but FF decreases for a small increment in Rs. However, large increase in Rs first affects the I_{sc} and then V_{oc}. The shunt resistance R_{sh} is infinitely high for an ideal solar cell but this is not true for the real solar cells. A real solar cell always has a finite value of shunt resistance R_{sh} and this value may decrease further for a solar cell due to the leakage path near the junction as well as due to the presence of defects like pinhole in the absorber layer. The decrease in the R_{sh} has adverse effect on the fill factor. A plot of dJ/dV determines the shunt conductance, $G = 1/R_{sh}$.

Due to a short minority carrier lifetimes, charged carriers can recombine before being swept across the junction by the in-build electric field. The magnitude of the electric field can be increased by applying a reverse biased voltage across the terminal, which allows the electrons with small diffusion length to be collected. Such an increment in the current due to bias voltage is called voltage-dependent current collection J_L (V). The presence of voltage-dependent current is observed as an increase in the slope in the reversed bias region of the light J-V curve. Such observation of the light J-V curve can be confusing since decrease in R_{sh} also affects the J-V curve in the same pattern. But the decrease in R_{sh} also affects the dark J-V curve as it does the light J-V curve. So if the dark J-V curve is well behaved but there is a slope in the light J-V curve, the voltage-dependent current collection can also be determined from the J-V measurement

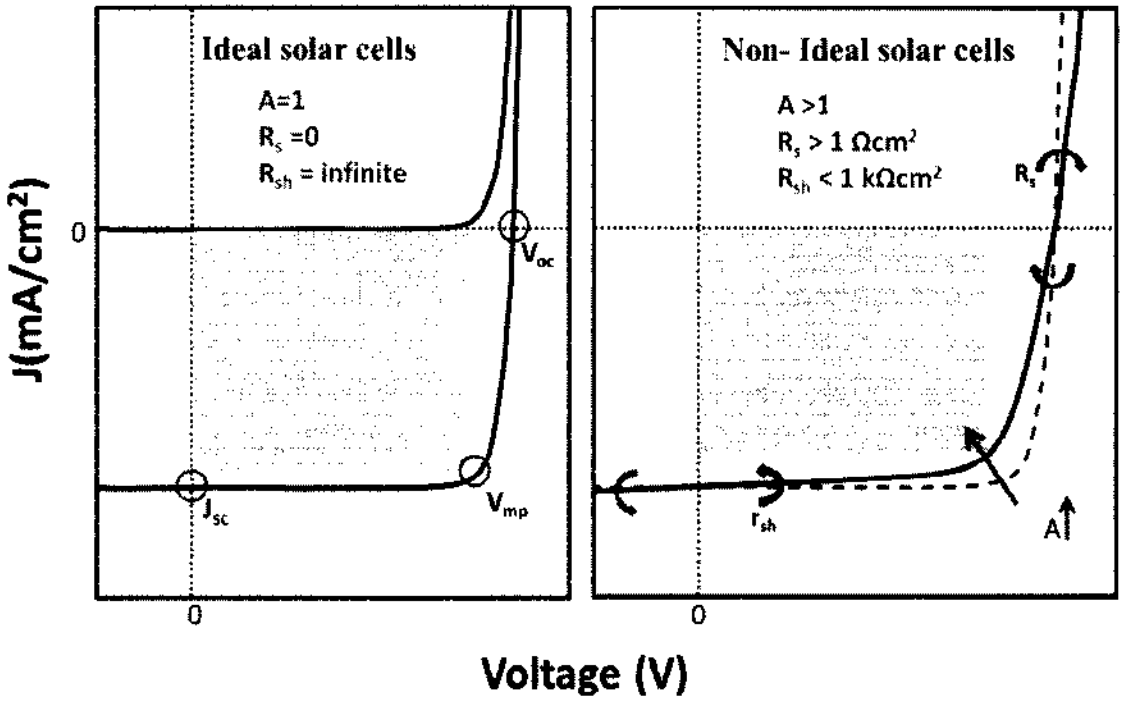

Figure 2.7 Light and dark J-V curves for an ideal and non-ideal solar cells [after 28].

2.2.13 External Quantum Efficiency

External quantum efficiency is defined as the number of charge carriers generated by the solar cells per absorbed photon of a particular energy and is a measure of the fraction of incident photons converted into current. When a photon arrives on the surface of a solar cell, it can be absorbed by any of the layers deposited on the solar cell. However, photons with high energy tend to be absorbed toward the surface of the cell facing the sun while photons with lower energy tend to be absorbed in the bulk of a solar cell. In a solar cell structure, different layers are designed to absorb different energies of light, with the layers of highest band gap toward the surface of the cell. So, each layer between the top and the bottom of the cell acts as a window. A solar cell does not get 100% QE, and the region of

the QE spectrum that have lower currents can provide insight to what layer in the solar cell is causing a problem within the cell. Therefore QE of a real solar cell may have less than a unity if either: i) the light is not absorbed or is reflected; ii) recombination occurs within the cell; or iii) there is a decrease in collection probability because of the mechanism that is being used for collection at a specific wavelength [29].

The total current density can be calculated by integrating the product of the EQE and the photon flux density. For the standard AM1.5 G solar spectrum, the calculation for short-circuit current density [30] is

$$J_{SC} = q \int_0^{\infty} EQE(\lambda) \frac{\lambda}{hc} E_{\lambda}^{AM1.5G}(\lambda) d\lambda \tag{2.9}$$

Where $E_{\lambda}^{AM1.5G}$ is the spectral irradiance of the AM1.5 G spectrum, λ is the wavelength, h is Planck's constant, and c is the speed of light.

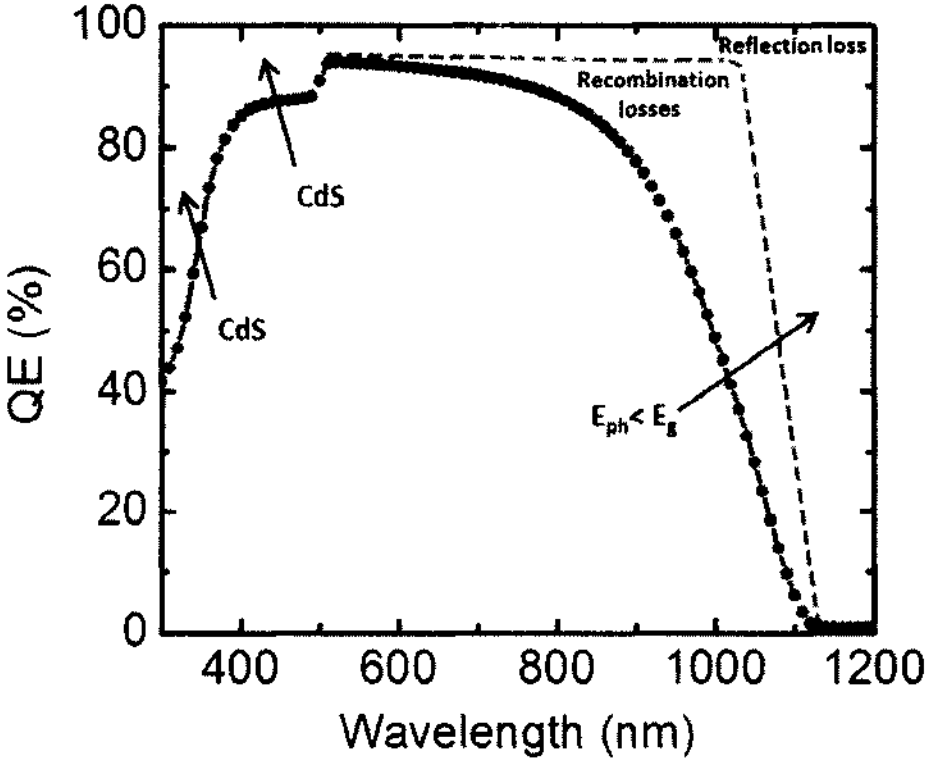

Figure 2.8: Typical CIGS quantum-efficiency curve and involved loss mechanisms.

The losses in the current are due to the optical properties of the different layers in the cell as well as to the electrical defects in the absorber layer. The different losses in the QE are shown in Figure 2.8. The following are the losses in the solar cell:

(i) "Reflection" losses are introduced by partial coverage of the front surface by the metal contact fingers or by reflection from the material interface. Such losses can be reduced by depositing a thin anti-reflecting coating.

(ii) "Window" absorption in the short-wavelength region is not significant due to the high band-gap energy of ZnO/AZO. Free electron absorption in the AZO layer can lower the quantum efficiency in the high wavelength region. Such losses can

be reduced by thinning the layers. If the thicknesses of the window layers are reduced significantly there are chances of bad junction between CdS and CIGS, shunting through i-ZnO layer and reduction in current collection due to increase in sheet resistance in the AZO layer. So there must be a balance between the optical losses and the electrical losses.

(iii) "Buffer" absorption is one of the major losses in thin-film solar cells (CIGS). Reducing the thickness of the CdS or replacing it with a higher band-gap material such as ZnS would be the possible alternatives.

(iv) "Recombination" losses are introduced due to traps or due to a low diffusion length of the absorber layer in the cell. The longer the wavelength, the deeper the generation of carriers and the higher the likelihood of recombination in the cell is. Such kind of loss can be visualized by measuring the QE under negative biased voltage.

(v) "Deep penetration" of carrier losses occurred for long wavelength photons due to incomplete absorption near the band gap of the absorber layer. These losses are inherent to most of the semiconductor since incident light with photon energy of $h\upsilon<E_g$ is not absorbed. This loss can be addressed by increasing the thickness of the absorber layer or making high quality absorbing materials.

CHAPTER 3

EFFECT OF ABSORBER THICKNESS ON ULTRATHIN CIGS FILMS AND DEVICES

3.1 Introduction and motivation

With 21.7% efficiency, $Cu(In,Ga)Se_2$ (CIGS) solar cells are the most efficient polycrystalline thin films solar cells today [5]. In addition to high efficiencies, CIGS thin film modules exhibit excellent outdoor stability [31-32] and radiation hardness [33-34]. Therefore, the combination of high efficiency with outdoor stability and radiation hardness makes CIGS a promising material for low cost and high efficiency solar cells. The standard thickness of the CIGS layer in CIGS thin-film solar cells is 1.5–2 μm [35]. If this thickness could be reduced, with only minor loss in performance, production costs could be lowered. A thinner CIGS layer would reduce the direct materials usage and so induce low materials costs. A reduction of materials usage is particularly important for indium and gallium since the supply of these metals might become an issue if CIGS thin-film solar cells are produced in very large volumes in the future [36]. The deposition time could also be reduced for thinner CIGS layers, which would directly lower production costs. However, a reduction of the absorber thickness is related with a number of problems. Even though the absorption coefficient of the CIGS material is very high, the amount of light absorbed in the CIGS layer will decrease with a reduced absorber thickness. When researchers try to reduce the CIGS layer to around 0.5 μm, the devices became electrically shunted which was related to the roughness of the film, which was of the same order as the film thickness itself [37]. In another case, an increase in the shunt conductance was observed when the CIGS

thickness was reduced [38]. Another potential problem for thinner CIGS layers is that the electrons will be generated closer to the back contact with higher probability for back contact recombination. These factors motivated us to study the effect of a reduced CIGS absorber thickness on device performance.

Fabricating CIGS solar cells with minimum thickness of the absorber layer has two key potential advantages over their thicker counterparts: it can reduce production cost by lowering material consumption and yielding higher throughput, and it can reduce recombination losses since the electron and holes generated by light do not need to travel so far. Optically, less than 0.5 μm absorber layer is needed to absorb more than 90% of the light with $E_{ph} > E_g$, even without considering reflection of the light at the back contact. However, the absorber thickness can influence the cell parameters in many ways such as i) Photocurrent density, J_{sc} reduced due to decrease in collection length ii) the effect of back contact (BC) recombination can increase and iii) local generation rate may be increased in case of a highly reflecting back contact such as ZrN, thus increasing Voc. In ultrathin CIGS solar cell, light spectrum can either be absorbed within the BC layer or they can be reflected from it. The reflected light from BC again can be absorbed during the second light pass through the ultrathin CIGS layer or transmitted out from the device. So a reduced absorber thickness must be compensated by an improved BC reflectance and a reduced BC recombination since light absorption depends upon the reflectance and absorbance of the BC layer.

In our case, solar cells with thick CIGS layer (~ 2 μm) were fabricated with the following standard structure: glass/Mo/CIGS/CdS/ZnO/ITO/grids by co-evaporation

processes and the thickness of the absorber layer was then gradually reduced to observe its effect on the device parameters.

3.2 Ultrathin CIGS Review

The concept of thinning the $Cu(In,Ga)Se_2$ (CIGS) layer is of great interest and has already been explored by several researchers [36-39]. The potential advantages of this concept derive from the reduction of cost and usage of materials (especially indium and gallium) and the increase in production throughput. In a standard CIGS device, the absorber thickness is typically 2 μm. Thickness of the absorbing layer reduction down to 0.4 μm would save 75% of the semiconductor material by considering the same yield and the deposition time would be four times shorter by keeping the same deposition rate. The recent significant achievements for producing ultra-thin cells with good performance are shown in Figure 3.1. More recently, recorded best CIGS solar cell [5] (blue diamond in Figure 3.1) have shown significant improvement in voltage and fill-factor. The thin films of the recent ultra-thin devices are smoother, making it possible to produce 0.5 μm or thinner devices. The thinnest device (0.15 μm) with remarkable performance [39] is 5 % efficient. The best 1 μm CIGS device [8] has achieved efficiency of 17.1 %, which is only 4.6 % less than the record CIGS solar cell [5]. Even though the thin CIGS solar cells have shown remarkable improvement in open circuit voltage (V_{oc}) and fill factor (FF), current reduction still remains which is the main cause for the thin film solar cells' lower efficiency. So the challenge for thinning the absorber with minimal efficiency loss is still open and this challenge should be mainly directed towards the improvement of the current loss to improve the thin cells performance.

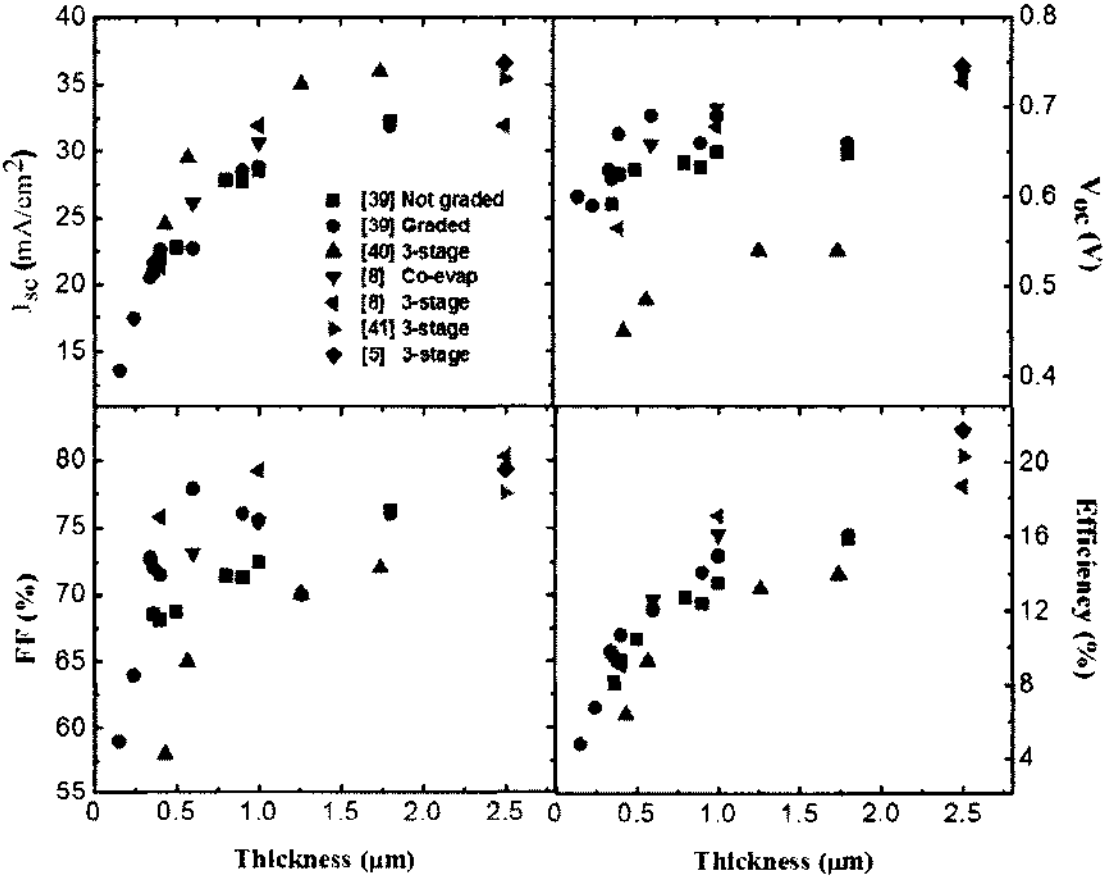

Figure 3.1 Review of experimental results of CIGS solar cells with thin absorbers layers (references mentioned next to the symbols).

3.3 Effect of CIGS thickness

CIGS thin films with various thicknesses were deposited by 1-stage co-evaporation process. The substrate temperature was maintained at 550°C while the targeted composition was a ratio of Cu/(In+Ga) = 0.85 and a ratio of Ga/(Ga+In) = 0.25. The thickness range targeted was from 2.0 μm down to 0.5 μm. The results are summarized in Table 3.1 below.

Table 3.1: Thickness and composition for the CIGS films deposited with the 1-stage process

Thickness (μm)	Cu (at %)	In (at %)	Ga (at %)	Cu/(In+Ga) (y)	Ga/(In+Ga) (x)
1.95	13.6	19.8	7.2	0.87	0.27
1.55	21.9	22.5	5.2	0.79	0.19
1.30	22.6	21.5	4.8	0.86	0.19
0.75	20.5	20.2	7.1	0.75	0.26
0.50	20.1	19.2	6.8	0.77	0.26

As one can see from Table 3.1, the thicknesses targeted were achieved while the compositions were slightly off, with a Cu-poor and Ga-poor tendency. Figure 3.2(a) shows the XRD patterns of CIGS films with various thicknesses. It was observed that all the peaks can be indexed by chalcopyrite polycrystalline $Cu(In_{0.7},Ga_{0.3})Se_2$ and molybdenum, which indicates that the CIGS films are single phase. Figure 3.2(b) and 3.2(c) are the XRD fine scans of the chalcopyrite (112) and (220)/(204) peaks of CIGS films with different thickness respectively. As can be seen from Figure 3.2(a), all the films tend to be (112) oriented while the FWHM did not show any specific trend even for the thinner films. This is confirmed in Figure 3.3 by cross sectional SEM images, where the grain size seems to be quite large for all films regardless of their thickness.

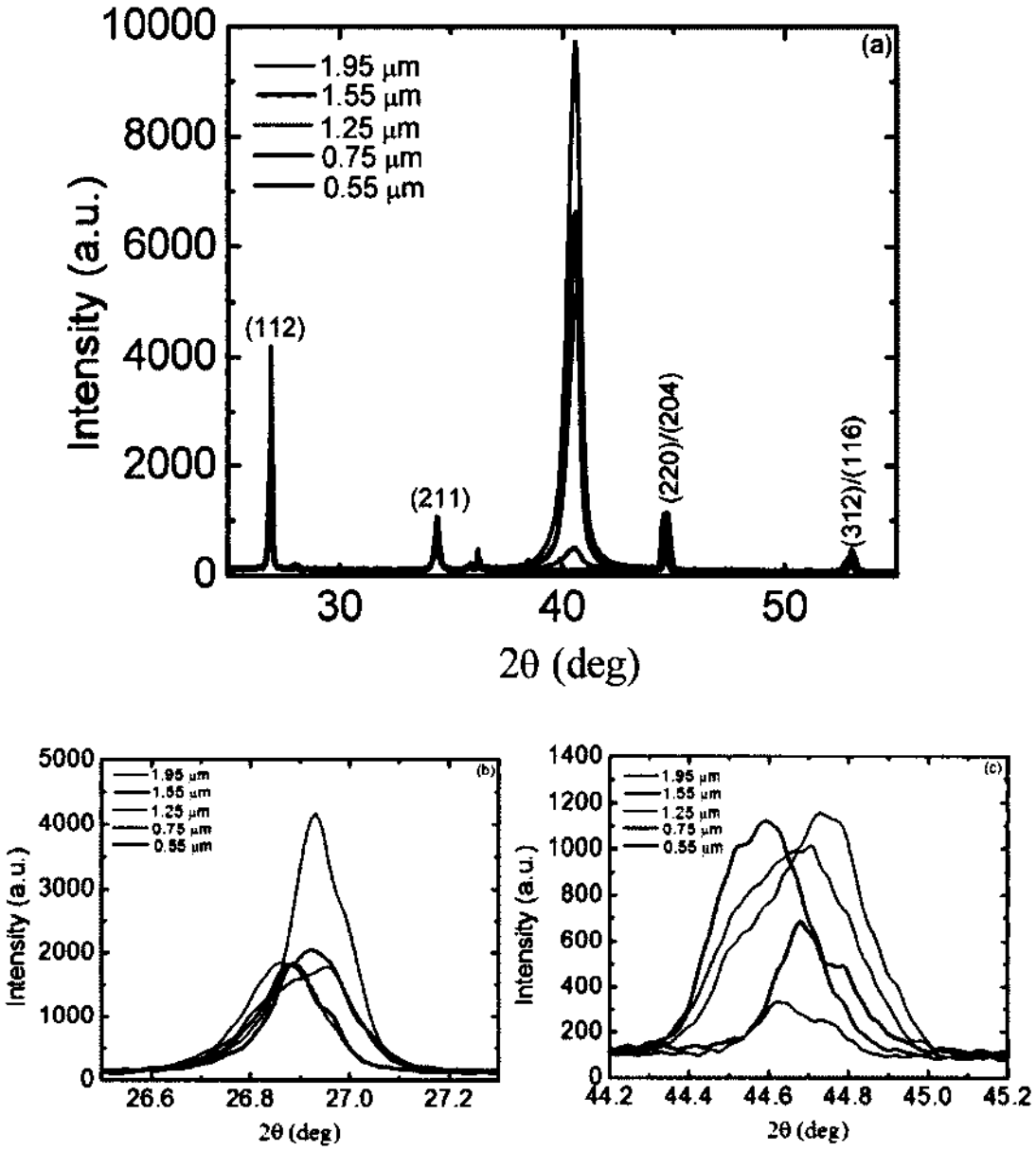

Figure 3.2(a) XRD patterns against the CIGS film thickness (b) XRD fine scans of (112) peaks of CIGS films with different thickness (c) XRD fine scans of (220)/(204) peaks of CIGS films with different thickness

It is known that x-ray diffraction intensity mainly depends on the thickness and material properties of the thin film. So the thickness of each of the layers must be taken into account in order to analyze the XRD spectra of the different layers more accurately.

The ratio of diffraction intensities of a specimen with finite thickness x to material with infinite thickness is given by [42]

$$G_x = \frac{\int_{x=0}^{x=x} dI_D}{\int_{x=0}^{x=\infty} dI_D} = [1 - e^{-\mu x(1/sin\alpha + 1/sin\beta)}] \quad (3.1)$$

For a flat specimen, $\alpha = \beta = \theta$ and equation 3.1 reduces to

$$G_x = \left(1 - e^{\frac{-2\mu x}{sin\theta}}\right) \quad (3.2)$$

Where α is the absorption coefficient, x is the thickness of the material and θ is angle of diffraction.

Since the mass absorption coefficient of a compound is the weighted fraction of the mass absorption coefficients of its constituents, the expression for the mass absorption coefficients of $Cu(In_{0.7},In_{0.3})Se_2$ is as follows [43].

$$\left(\frac{\mu}{\rho}\right) Cu(In_{0.7}, Ga_{0.3})Se_2 = \frac{M_{Cu}\left(\frac{\mu}{\rho}\right)Cu + 0.7M_{In}\left(\frac{\mu}{\rho}\right)In + 0.3M_{Ga}\left(\frac{\mu}{\rho}\right)Ga + 2M_{Se}\left(\frac{\mu}{\rho}\right)Se}{M_{Cu} + 0.7M_{In} + 0.3M_{Ga} + 2M_{Se}} \quad (3.3)$$

Where $\frac{\mu}{\rho}$ is the mass absorption coefficient of the $Cu(In_{0.7}, Ga_{0.3})Se_2$ film, ρ is the material density and M is the molar mass. The mass absorption coefficients and molar mass values for Cu, In, Ga and Se are given in the table 3.2. Hence from equation 3.3, the value of $\frac{\mu}{\rho}$ for $Cu(In_{0.7},Ga_{0.3})Se_2$ is 117.74 cm^2/g. The density of $Cu(In_{0.7},Ga_{0.3})Se_2$ film is 5.692 gcm^{-3} [44]. The absorption coefficient μ is obtained by multiplying with the density of $Cu(In_{0.7},Ga_{0.3})Se_2$ to be 117.74*5.692 = 670.17 cm^{-1}. Then, using equation 3.2 and the calculated values for the absorption coefficients of $Cu(In_{0.7},Ga_{0.3})Se_2$, the ratios of diffraction intensities G_x for (112) and (220/204) peaks of CIGS films are obtained, as

shown in table 3.3. It was observed that the values of G_x decrease significantly as thickness reduces. The values of G_x for the CIGS film with thickness 0.5 μm are only about one-third of those for the CIGS film with thickness 1.95 um. It clearly indicates that the diffraction intensity of X-ray will decrease for ultrathin films.

Table 3.2 The Mass absorption coefficients (μ/ρ) values and molar mass values for Cu, In, Ga and Se from [48].

Element	Cu	In	Ga	Se
μ/ρ (cm^2g^{-1})	52.7	252.0	63.30	82.80
M ($gmol^{-1}$)	63.54	114.8	69.72	78.96

Table 3.3 Calculated values of the ratio of the XRD peak intensities G_x for (112) and G_x (220/204) peaks of CIGS films with different thickness

Thickness (μm)	1.95	1.55	1.3	0.75	0.5
G_x(112)	0.675	0.591	0.528	0.351	0.251
G_x(220/204)	0.498	0.421	0.369	0.233	0.162
G_x(112)/G_x(220/204)	1.357	1.402	1.432	1.508	1.547

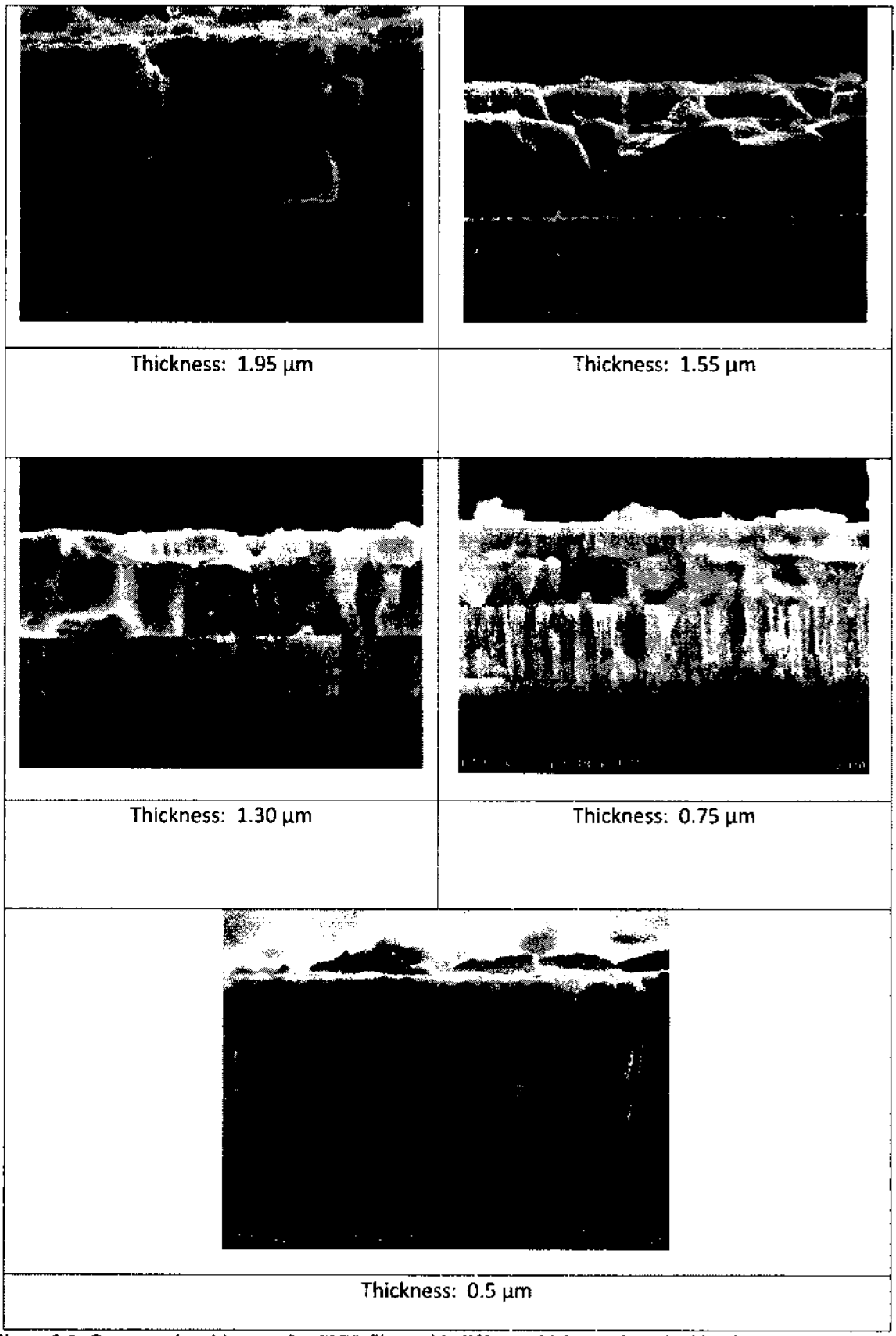

Figure 3.3: Cross-sectional images for CIGS films with different thickness deposited by the 1-stage process.

Transmission and Reflection measurements (Figure 3.4) correlate well with composition measurements, with a lower band gap for the 1.55 and 1.25 μm films, while one can observe above band gap transmission as expected for the ultrathin films (below 1 μm). These transmission spectra also confirm that each of the film with different thickness has low sub-band gap absorption, which indicates that all these films have minimum allowed impurities states in the band gap.

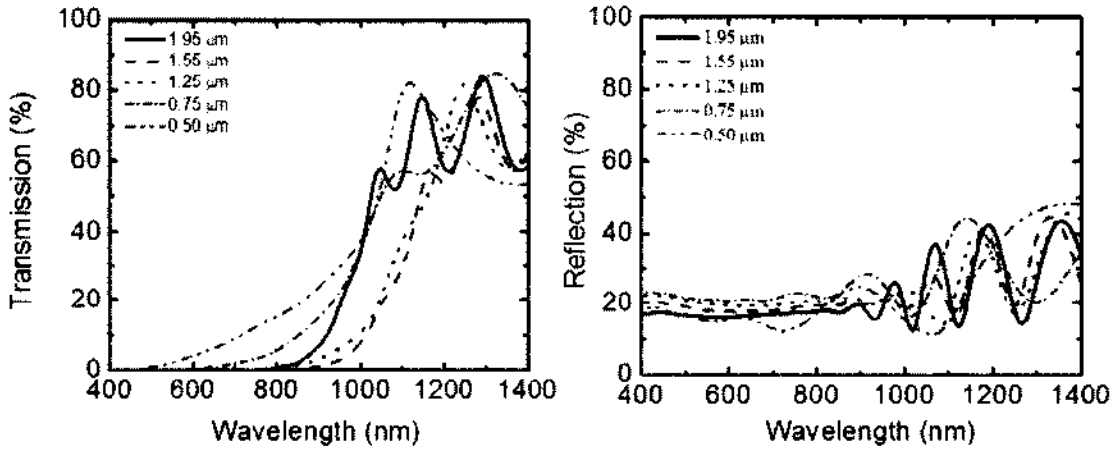

Fig 3:4 (a) Transmission (T) and (b) reflection (R) spectra CIGS films with different thicknesses

CIGS solar cells were then fabricated for the 5 different thicknesses with the following standard structure: glass/Mo/CIGS/CdS/ZnO/ITO/grid. Cells with total area of 0.50 cm^2 were defined by mechanical scribing. The efficiency of the completed device was extracted from J-V measurements under 100 mW/cm^2, and the currents confirmed by QE measurements under white light bias. Results for the devices are reported Table 3.4 and Figure 3.5. One can observe that the current and voltage are roughly constant as thickness reduced from 2 μm to 1.3 μm, while decreasing for 0.75 μm and 0.5 μm as shown in Figure 3.5. Similar trend of reducing the solar cell parameters was observed for the solar cells with

CIGS thickness below 1 μm [40]. The decrease in absorbance in long wavelength with decreasing the CIGS thickness would be the main reason of reducing J_{sc} [40]. As we can see in Figure 3.5 (right), there is the reduction in QE as thickness of CIGS is reduced. It was found that the reduction of QE is more than the reduction of absorbance in the short wavelength, which would be due to the electrical loss mechanism such as enhancement of the series resistance and recombination of photoelectrons in back contact [41]. The decrease in V_{oc} as absorber layer thinned down below 1 μm could be due to the increase in shunt conductance with reducing CIGS absorber layer thickness. The reduction in FF is also probably due to an increase in series and shunt conductance. These results will therefore be analyzed in the next section for enhanced understanding and to allow designing new experiments.

Table 3.4 Solar cells parameters for CIGS solar cells deposited by 1-stage process with various thicknesses

Thickness (μm)	V_{oc} (V)	J_{sc} (mA/cm^2)	J_{sc} from QE (mA/cm^2)	FF (%)	Efficiency (%)
1.95	0.52	28.8	28.5	61.3	9.2
1.55	0.55	27.6	28.5	66.0	10.1
1.30	0.52	28.9	28.6	68.5	10.3
0.75	0.50	25.4	25.0	70.0	8.9
0.50	0.44	22.5	21.0	56.6	5.6

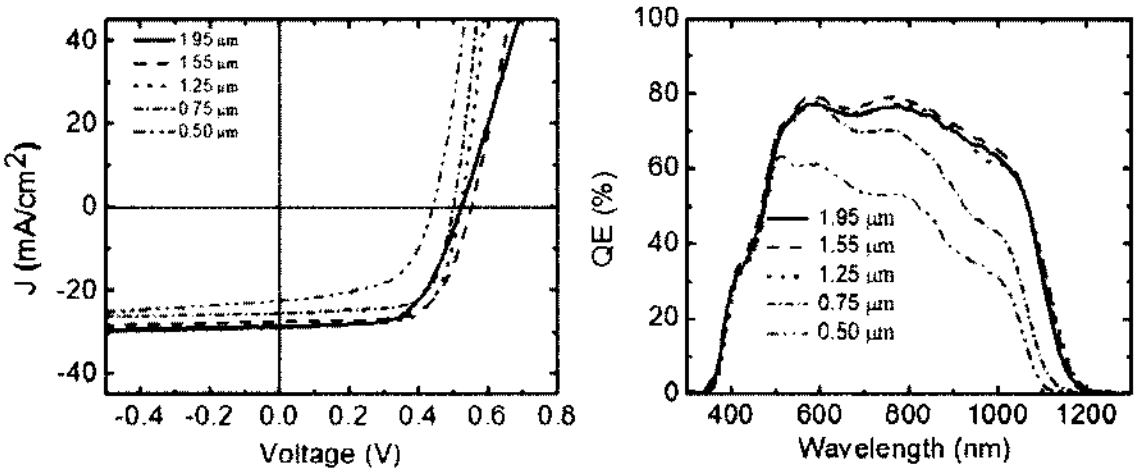

Figure 3.5: J-V measurements and Quantum Efficiency (QE) of devices fabricated by 1-stage process from $Cu(In,Ga)Se_2$ thin films with different thicknesses

3.4 Numerical Analysis of Ultra-thin $Cu(In,Ga)Se_2$ Solar Cell

3.4.1 Introduction and Motivation

A numerical modeling is a theoretical construct representing the real processes and parameters that influence them. Numerical models have become increasingly important tools to test the viability of proposed physical explanations and to predict the effect of changes in material properties and geometry on the solar cell performance. These models have become indispensable tools in order to design any kind of efficient solar cell. They can help the better understanding of cell operation and provide the manufacturers additional guidance to improve the product performance by optimizing their design. A good model, where only the most important parameters are considered, is a good representation of a real phenomenon and helps to enhance our understanding. As our understanding has increased, so has our increased need for complex models in order to provide the sufficient realistic descriptions of their operations. This added complexity has

exceeded our ability to solve the problems in analytical way. As a result, we need to have numerical solutions to avoid unrealistic assumptions to get the proper solutions. Carefully constructed models provide the need to push cell efficiency toward the absolute limit by optimizing the existing designs and compromising it with competing design proposals. A schematic of the numerical modeling for the best solar cells performance is shown in Figure 3.6. Once the cell is fabricated, complete characterization is needed to determine the losses. Careful analysis of characterization curves leads to hypothesis of where these losses come from. Numerical modeling tools can support the hypothesis and explain the physical mechanism behind these losses. In solar cells, numerical solution tools allow the inclusion of important materials characteristics such as mobility, life time and band-gaps which would predict the quantitative impact of changes in material properties on solar cell device performance and suggest better way to change the optimized deposition process and improve overall cell performance. It is clear that numerical modeling is a valuable technique to improve the solar cells performance but interpretation of modeling results needs to be done carefully.

The experimental results for ultrathin CIGS solar cells (as shown in Figure 3.5) indicates that the efficiency drops not only due to the decrease in J_{sc}, which is expected since the absorber layer gets thinner, but also due to decrease in V_{oc} and FF. The degradation of the overall performance of the ultrathin CIGS solar could be due therefore to the combination of reduction in thickness of the absorber layer as well as the presence of impurities in the absorber layer. It was found that the bulk defect in the CIGS absorber layer can affect the entire solar cell performance [32]. A deep defect, which lies in the upper part of the energy gap (0.8 eV from the valence band), was found to have a very

significant influence on the CIGS solar cells performance [36]. One of the purposes of this simulation is to help us increase the efficiency of the ultrathin CIGS solar cells by understanding the influence we can have on the defects within the band gap of the CIGS.

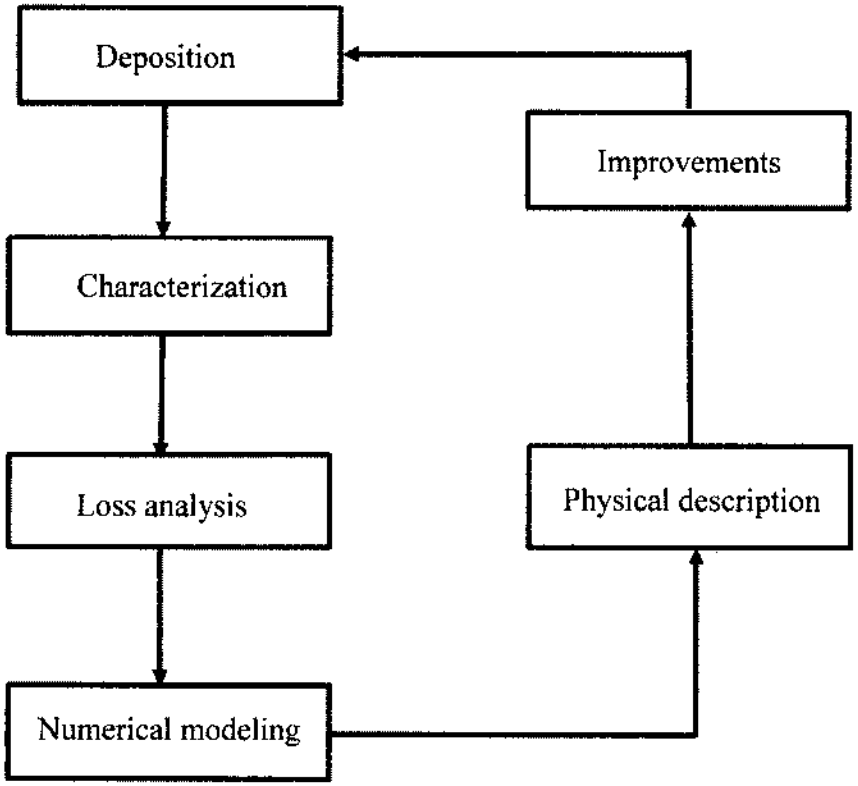

Figure: 3.6: A schematic of the numerical modeling to improve solar cells performance

3.4.2 Effect of CIGS Thickness

There are several software programs that have been written with a specific purpose of modeling solar cells. All of them have different unique features and limitations but they have the same basic principles. In this work, wx-AMPS [45] and SCAPS [46] have been used for the solar cell simulation. One advantage of SCAPS-1D over wxAMPS-1D is its capacity to simulate capacitance-voltage (C-V) and capacitance-frequency (C-F) characteristics. Inclusion of interfaces between layers is another advantage of SCAPS in

comparison of wx-AMPS. On the other hand, wx-AMPS has better plotting options, and it can perform multiple simulations at the same time.

3.4.3 Basic Concepts

The main equations of carrier transport in the semiconductors are Poisson's equation and the carrier continuity equations. Poisson's equation is mainly for the distribution of the electrical field inside the device whereas continuity equations for electrons and holes are basically the conservation equation of carrier currents. Wx-AMPS was mostly used in this work so its principles will be explained in details. In wx-AMPS, the steady state band diagram, recombination profile and carrier transport are estimated in one dimension based on the Poisson's equation and the hole and electron continuity equations. The Poisson's equation is [31]

$$\frac{d}{dx}\left(-\varepsilon(x)\frac{d\psi}{dx}\right) = q[p(x) - n(x) + N_D^+(x) - N_A^-(x) + p_t(x) - n_t(x)] \qquad (3.1)$$

where, ψ is the electrostatic potential, n, p are the concentrations of free electrons and holes, n_t and p_t are the concentrations of trapped electrons and holes, N_D^+ and N_A^- are the concentrations of ionized donors and acceptors, ε is the dielectric permittivity of semiconductor, and q is the electron charge.

The charge transport process of an electronic device is derived by the continuity equation for the holes and electrons. The continuity equations for holes and electrons are [31]

$$\frac{\partial p_n}{\partial t} = -p_n\mu_p\frac{\partial \xi}{\partial x} - \mu_p\xi\frac{\partial p_n}{\partial x} + D_p\frac{\partial^2 p_n}{\partial x^2} + G_p - \frac{p_n - p_{no}}{\tau_p} \qquad (3.2)$$

$$\frac{\partial n_p}{\partial t} = n_p \mu_n \frac{\partial \xi}{\partial x} + \mu_n \xi \frac{\partial n_p}{\partial x} + D_n \frac{\partial^2 n_p}{\partial x^2} + G_n - \frac{n_p - n_{po}}{\tau_n} \quad (3.3)$$

Where ξ is the electric field, G is the generation rate, D is the diffusion coefficient. All these parameters are a function of the coordinate position x. In this work, only steady state solutions are considered and hence:

$$\frac{\partial p_n}{\partial t} = 0 \; and \; \frac{\partial n_p}{\partial t} = 0 \quad (3.4)$$

The light intensity decreases exponentially with penetration into the material. The generation rate, which gives the number of electrons generated at each point in the cell, is highest at the surface of the material, where the majority of the light is absorbed. It is proportional to the remaining light intensity. So the generation rate G(x) equals:

$$G(x) = -\frac{dI(x)}{dx} = \alpha I(x_o) e^{-\alpha (x - x_o)} \quad (3.5)$$

Where I(x) is the light intensity at the point x, x_o is the point on the top of the particular layer and α is the absorption coefficient. The electrical potential (Φ) and the carrier concentrations (n and p) or, alternatively, the potential (Φ) and the quasi-Fermi levels for electrons and holes (E_{Fn} and E_{Fp}), are the unknown variables in the solar cell simulation.

3.4.4 Base Line Parameters for CIGS Solar Cells

Numerical modeling of CIGS solar cells is an efficient way in order to verify the viability of created hypothesis depending on the physical explanations and to predict the effects of these physical changes on the solar cell performance. Well-known input parameters should not be changed in any case, whereas input parameters that have only marginal effect on the output tested are kept constant. The remaining parameters should be available for further fitting purposes. Important guidelines that should be considered while

assigning input parameters for numerical simulations are discussed below and then baseline parameters for CIGS solar cells are proposed.

3.4.5 Base Line Parameters for CIGS Solar Cells

3.4.5.1 Front and Back Contact

The formation of stable, low resistance and non-rectifying contacts is critical for the performance and reliability of solar cell devices. The reflection at the back contact has noticeable influence on the achievable short-circuit current density (Jsc) for ultrathin CIGS solar cells. In general, simulation tools support a constant multiplicative reflection factor for the front surface (i.e. $R_F = 0.1$, 10% reflection) which decreases the quantum efficiency (QE) by this fraction. If interference effects are neglected, QE curves show a fairly flat response at intermediate wavelengths of ~ $(1 - R_F)$. Surface recombination can have a major impact on J_{sc} as well as V_{oc} in the solar cells. The surface recombination velocities at the top and rear contact are chosen to be equal to the thermal velocity.

3.4.5.2 Solar Cell Material Parameters

The minority carrier diffusion length is the average distance a carrier can diffuse from its point of generation until it recombines with the majority carriers. The relation between diffusion length and carrier lifetime is given by:

$$L = \sqrt{D\tau} \qquad (3.6)$$

Where L is the diffusion length, D is the diffusivity and τ is the lifetime of the carrier. The baseline value of electron lifetime for CIGS is 1.6 ns, which is slightly lower than the values used for standard CIGS (XX ns) since this work mainly deals with thinner cells, which may have higher defects density than the standard thickness (2 μm) [32].

The relation between diffusion constant D and carrier mobility μ is given by the Einstein equation:

$$D = \frac{kT}{q}\mu \qquad (3.7)$$

Carrier mobilities for polycrystalline material should be chosen lower than the values reported for crystalline materials [2]. Effective masses for direct band gap materials are m_e^* = $0.2m_o$ for electrons and m_h^* = $0.8m_o$ for holes. The ratio of the carrier mobilities, μ_e/μ_h should be approximately proportional to the ratio of the effective masses, m_e^*/m_h^* [2]. The reported values of electron mobilities for single crystal CIGS is in the range of 90 and 900 V/cm^2-s [33]. The value of electron mobility used in this study is 100 V/cm^2-s.

The effective densities of states in the conduction and valence band can be calculated using the following equation:

$$N_C = 2\left(\frac{2\pi m_e^* kT}{h^2}\right)^{3/2} \text{ and } \quad N_V = 2\left(\frac{2\pi m_e^* kT}{h^2}\right)^{3/2} \qquad (3.8)$$

If temperature dependent simulations are needed, the direct temperature dependence in N_C and N_V should be taken into account. Carrier concentrations can be determined by Hall effect measurement. The typical carrier concentration for CIGS is in the order of 10^{16} cm^{-3}.

3.4.5.3 Defect States

Schockley-Read-Hall (SRH) model is being used in most of the numerical simulators to describe carrier recombination currents. It is recommended to assign recombination defect states in a narrow distribution close to the middle of the band gap, since variations of the energetic defect distribution show negligible effects on the output. A defect state can change its state of charge only by one electronic unit of charge in SRH formalism [34]. So one can make the following distinctions: An acceptor-like (donor-like) defect state is able to accept (donate) one electron. The two possible charge states for acceptors (donors) are negative and neutral (positive and neutral). It always follow that free holes (electrons) will be coulomb-attracted to ionized acceptor-like (donor-like) defect states, whereas electrons (holes) will have no strong interaction with the acceptor-like (donor- like) defects giving very small electron (hole) cross-sections. An attractive cross-section is assigned corresponding to a radius at which the coulomb potential energy of the carrier in the field of the charged trap equals to kT [32].

$$\sigma_{att} = \frac{q^4}{16\pi\epsilon^2 k^2 T^2} \approx 10^{-13} - 10^{-12} cm^{-2} \qquad (3.9)$$

Neutral cross-sections can range between 10^{-18} and 10^{-15} cm^2. Smaller values will be reasonable if transitions are unlikely or to compensate for strong field effects.

3.4.5.4 TCO/CdS/Cu(In,Ga)Se_2 solar cells

CIGS solar cell mainly consists of three layers: n-ZnO Transparent contact, n-CdS window, and p-CIGS absorber. A single deep donor (acceptor) trap is used for the CIGS (CdS) layer. The high defect density in the CdS layer is responsible to generate the typical superposition failure in CIGS solar cells. Besides the band alignment, device performance is essentially independent of ZnO and only weakly dependent on CdS parameters. Most CIGS parameters have significant influence on solar cells performance. The mobilities for CIGS layer are assigned a factor of three below crystalline material values. For the effective masses in all layers, the default values of $0.2m_0/0.8m_0$ were used. The optical reflection at the front surface of the solar cell is taken to be 5% whereas the optical reflection from the back contact is set at 80%. The influence of the series resistance and shunt resistance are not taken into consideration for this simulation. The AM 1.5 solar spectrum is used during this simulation and the temperature is set at 300K. Base line case parameters are shown in Table 3.6.

Figure 3.7 shows a J-V curve of experimental and simulated data for the ultrathin CIGS solar cell with thickness 0.75 μm for our baseline. The ultrathin CIGS solar cell (0.75 μm CIGS) performance parameters such as open-circuit voltage (V_{oc}), short-circuit current density (J_{sc}), fill factor (FF) and efficiency from simulation and experimental results are shown in Table 3.5. The agreement between experiment and simulation is good for the J-V curve and validates our set of parameters as a baseline for simulating the influence of thickness variation of the absorber layer on the solar cell performance. In the simulation, the grain recombination boundaries have been taken into account by increasing the bulk defect density. The properties of the other layers in the solar cell are kept constant in order

to obtain qualitative information on the effect of the absorber layer thickness on the solar cell electrical parameters. The band gap of the CIGS absorber layer is also kept constant at 1.15 eV.

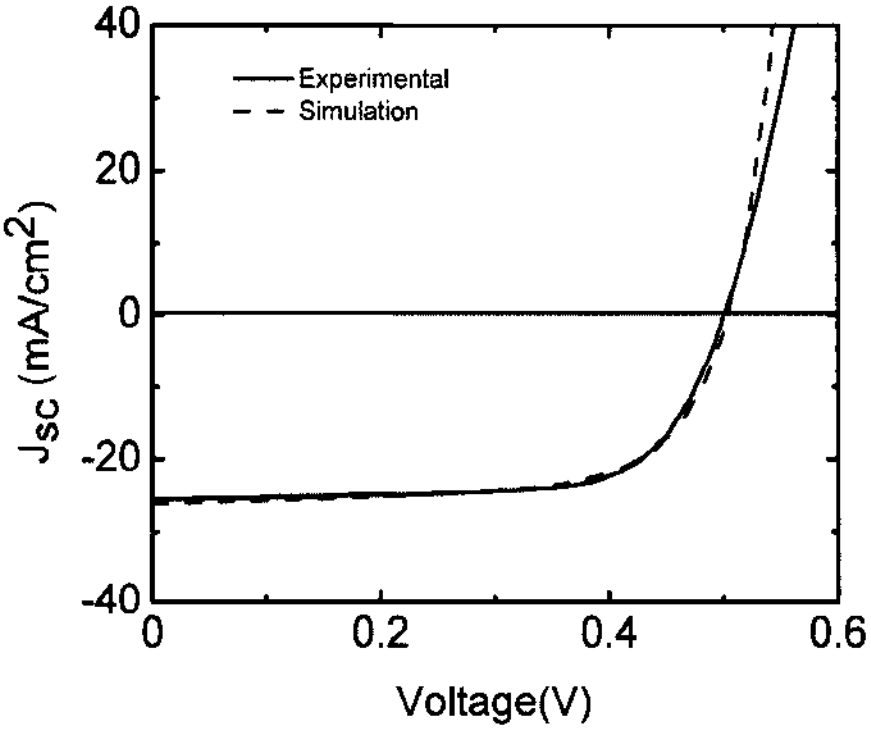

Fig 3.7: Comparison between the J-V curves for the simulated and the experimental result for 0.75 μm CIGS solar cell.

Table 3.5 Results from simulation compared with experimental results for 0.75 μm CIGS solar cell.

	Voc (V)	J_{sc} (mA/cm^2)	FF (%)	Efficiency (%)
Experimental	0.50	25.4	70.0	8.9
Simulation	0.52	25.7	69.5	9.2

Table 3.6: CIGS baseline parameters taken for the simulations

General device properties			Front	Back
Φ_b (eV)			$\Phi_{bn} = 0$	$\Phi_{bp} = 0.2$
S_e(cm/s)			10^7	10^7
S_h(cm/s)			10^7	10^7
Reflectivity			0.05	0.8
Layer properties	AZO	ZnO	CdS	CIGS
T (nm)	300	200	50	2000
$\varepsilon/\varepsilon_0$	9	9	10	13.6
μ_e (cm^2/Vs)	100	100	100	100
μ_h (cm^2/Vs)	25	25	25	25
$N_{D/A}$ (cm^{-3})	N_D: 10^{18}	N_D: 10^{18}	N_D:10^{18}	N_A:10^{16}
E_g (eV)	3.3	3.3	2.4	1.15
N_C (cm^{-3})	2.2 10^{18}	2.2 10^{18}	2.2 10^{18}	2.2 10^{18}
N_V (cm^{-3})	1.8 10^{19}	1.8 10^{19}	1.8 10^{19}	1.8 10^{19}
Defect States	AZO	ZnO	CdS	CIGS
N_{DG},N_{AG}(cm^{-3})	D: 10^{17}	D: 10^{17}	A: 10^{18}	D:10^{14}-10^{16}
E_A, E_D (eV)	Mid gap	Mid gap	Mid gap	Mid gap
W_G (eV)	0.1	0.1	0.1	0.1
σ_e (cm^2)	10^{-12}	10^{-12}	10^{-17}	5 10^{-13}
σ_h (cm^2)	10^{-15}	10^{-15}	10^{-12}	10^{-15}

3.4.6 Parameters Affected by the Thickness of the CIGS Absorber

Various thicknesses of the CIGS absorber layer were simulated to investigate their effect on CIGS based solar cells properties. The solar cell structure used was ZnO:Al/i-ZnO/CdS/CIGS. We studied how the absorber layer thickness, hole density and band gap influence the short-circuit current density (J_{sc}), open-circuit voltage (V_{oc}), fill factor (FF) and efficiency of the solar cell.

3.4.6.1 Effect of CIGS Absorber Layer Thickness on the Solar Cell Parameters

The standard thickness of the CIGS absorber layer is about 2 μm. CIGS absorber layer with various thicknesses, varying from 1.95 μm to 0.5 μm, were incorporated into the numerical simulation. The parameters of the other layers were kept constant.

We observed that all of the electrical parameters (J_{sc}, V_{oc}, FF and efficiency) decreased for thicknesses below 1 μm. The short circuit current density (J_{sc}) was the most affected due to the increasing transparency of the thin CIGS layers and to the recombination at the interface between the absorber layer and the back contact [35]. For ultrathin absorber layer, short wavelength penetrates deeply into the absorber and generates electron-hole pair near the back contact, which is the critical area for the recombination, resulting in the decrease of the current density. This recombination at the back contact also has a great effect on the V_{oc} and the FF.

However, the reduction in thickness itself was not enough to obtain a good agreement between our experimental results and our simulations. We also had to introduce a variation of the bulk defect density to allow for a better fit. As we mentioned earlier, in

the simulation, the grain recombination boundaries have been considered as increased bulk defect density. Attempts were therefore made to compare the simulation results with our experimental results by introducing an intentional higher defect density into the absorber layers, as shown Table 3.7. The results are shown in Figure 3.8 where the solid red circles denote the experimental results. Very good agreement was obtained between the simulated solar cell parameters (V_{oc}, J_{sc}, FF and efficiency) and the experimental results. The simulated current-voltage characteristics of the ultrathin CIGS solar cells suggest that the deep states defects that lye in the upper part of the energy gap are responsible for the deterioration of the overall solar cell performance of the ultrathin CIGS solar cells.

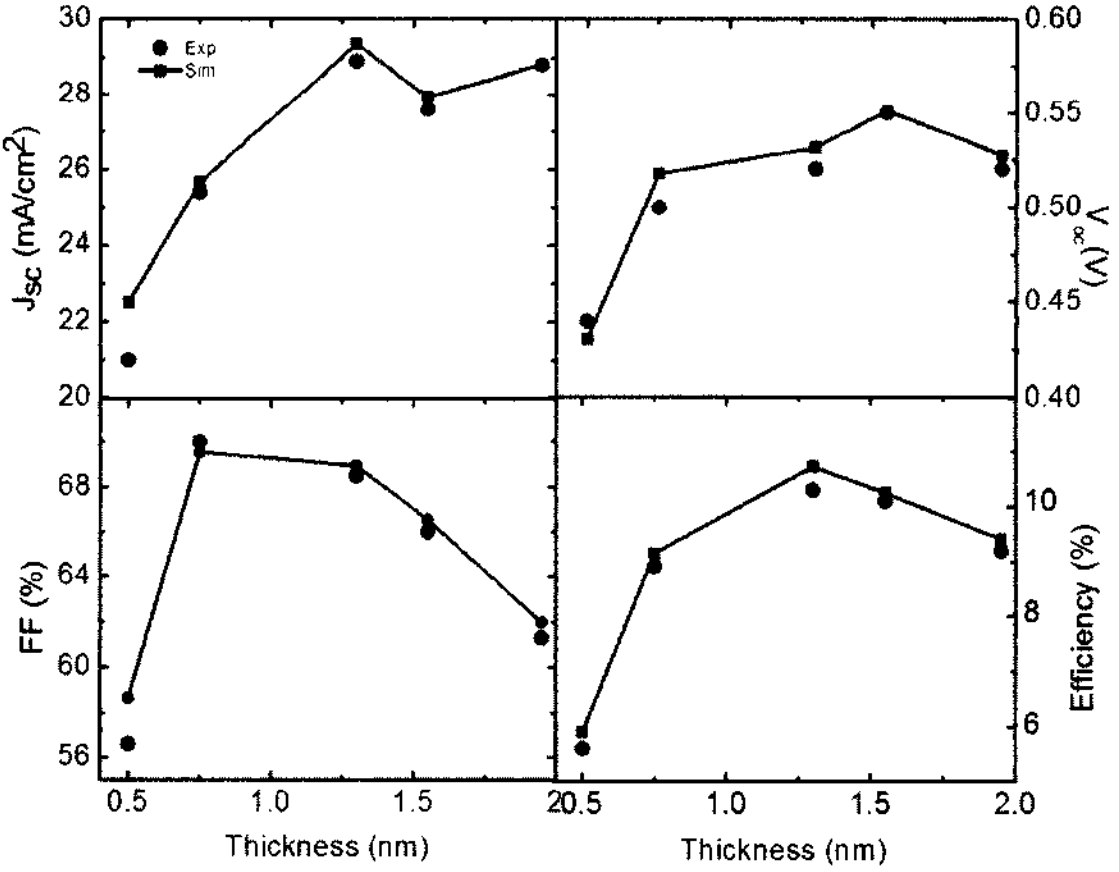

Figure 3.8: Simulated results on the effect of absorber layer thickness on the short circuit current (J_{sc}), open-circuit voltage (V_{oc}), fill factor (FF) and the efficiency, where the defect density for each thickness is modified (see Table 3.7)

Table 3.7 Results from the simulation for CIGS solar cell with different thicknesses and with different defect density whereas experimental results in parenthesis for comparison.

Thickness (μm)	V_{oc},(V) (exp.)	J_{sc}, (mA/cm^2) (exp.)	FF (%) (exp.)	Eff.(%) (exp.)	Defect density (cm^{-3})
1.95	0.54(0.52)	28.8 (28.8)	61.9 (61.3)	9.6 (9.2)	6.4 E+14
1.55	0.56(0.55)	27.9(27.6)	66.5(66.0)	10.3(10.1)	5.9 E+14
1.30	0.53(0.52)	29.3(28.9)	68.9(68.5)	10.7(10.3)	3.1 E+14
0.75	0.52(0.5)	25.7(25.4)	69.5(70)	9.2(8.9)	1.9 E+15
0.50	0.43(0.44)	22.5(21)	58.6(56.6)	5.9(5.6)	1.9 E+16

Figure 3.9 shows the simulated quantum efficiency curves, which indicate that the absorption of the incident light greatly decreases for thicknesses below 1 μm toward the wavelength greater than 500 nm. This could be due to the combined effect of light transmission and high recombination of electrons at the CIGS/Mo interface. The decrease in V_{oc} could be related to the degradation of the junction in the case of ultrathin thickness or back surface recombination. The overall cell performance for ultrathin CIGS is reduced due the decrease in J_{sc}, V_{oc} and FF. The decrease of the efficiency is more severe when the thickness of the absorber layer reduced below 500 nm due to the simultaneous action of degradation of the absorption, presence of defect density and electrons capture by the back contact.

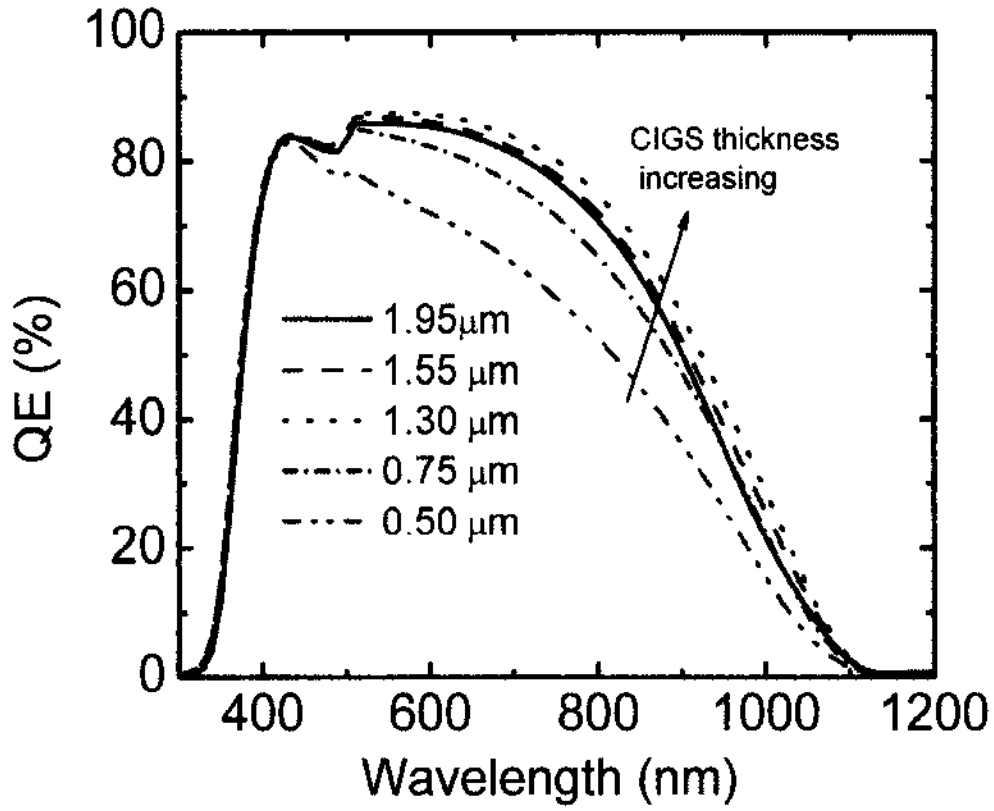

Figure 3.9: Simulated quantum efficiency of the cell with different CIGS absorber layer thickness.

3.4.6.2 Effect of Defect States on Ultrathin CIGS Solar Cell Parameters

The surface defect density and/or the bulk defect density are key factors limiting the overall performance of the CIGS solar cells [36]. A shallow defect with 0.3 eV was found to have little impact on the decrease of the solar cells performance [37], while a deep one lying in the upper part of the energy gap (0.8 eV from the valence band) was found to have a severe influence on the CIGS solar cell performance [38]. It was found that the defect states always harm the CIGS solar cells performance, but that when the defect state density is below 10^{14} cm^{-3}, they have less effect on the CIGS solar cell performance [36].

During the simulations, we fixed the thickness of the absorber at 0.75 μm to quantify the effect of the defect density on the solar cells parameters. The location of the defect state was fixed in the middle of the band gap. The defect state density was varied between 10^{13} cm^{-3} and 10^{16} cm^{-3}. The change in short-circuit current (J_{sc}) and fill factor (FF) with respect to defect density are shown in Figure 3.10. When the defect state is less than 10^{14} cm^{-3}, J_{sc} and FF change only slightly. As the defect density increases from 10^{13} to 10^{16} cm^{-3}, J_{sc} decreases from 29.0 mA/cm^2 to 22.3 mA/cm^2 while FF decreases from 77.5 % to 61.7 %, indicating a range where these two parameters are greatly affected by a change in the defect density.

The change in open circuit voltage (V_{oc}) and photoelectric conversion efficiency with respect to defect density is shown in Figure 3.11. When the defect state is less than 10^{14} cm^{-3}, the defect state has also very little effect on V_{oc} and hence on the efficiency of the ultrathin CIGS solar cell. When the defect state increases from 10^{13} cm^{-3} to 10^{16} cm^{-3}, V_{oc} decreases from 0.58 V to 0.43 V, while the efficiency of the cell decreases from 13.0% to 5.9%. Overall, it was therefore observed that the defect density always harm the performance of the ultrathin CIGS solar cells but that it is less pronounced when the defect state density is less than 10^{14} cm^{-3}. This is in good correlation with the results we obtained for varying thicknesses (Table 3.7) where we showed that the defect density increased with the reduced thickness, accelerating even more the decrease in efficiency. Finding the origin of these defects and a way to passivate them is therefore a key to improve ultrathin CIGS solar cell efficiency.

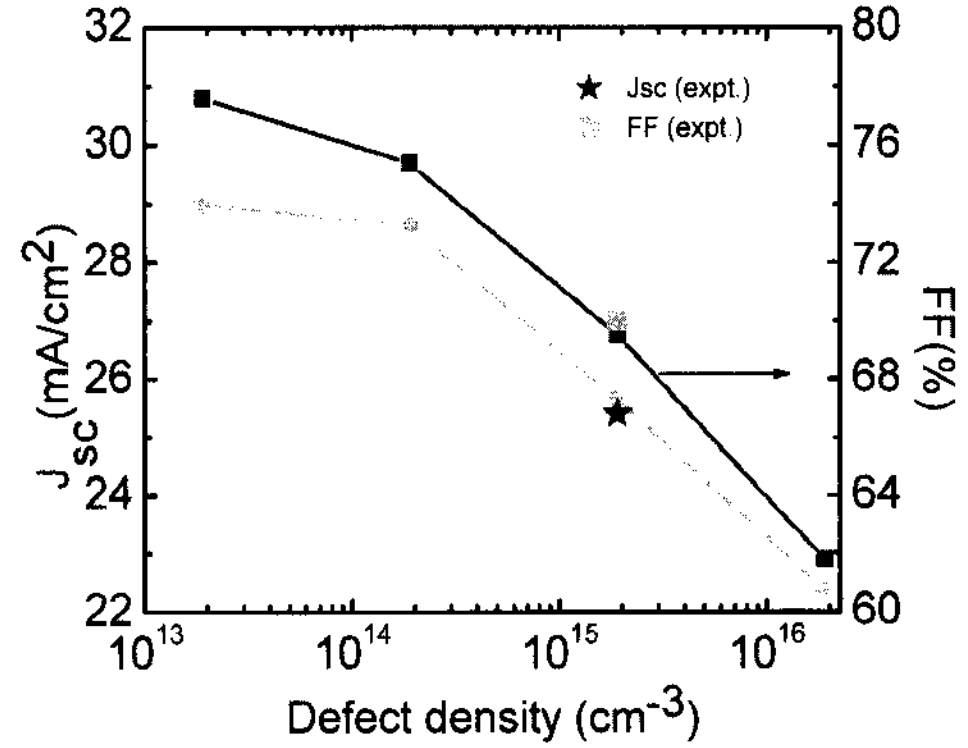

Fig 3.10: J_{sc} and fill factor (FF) with respect to defect density in the ultrathin (0.75 μm) CIGS solar cell.

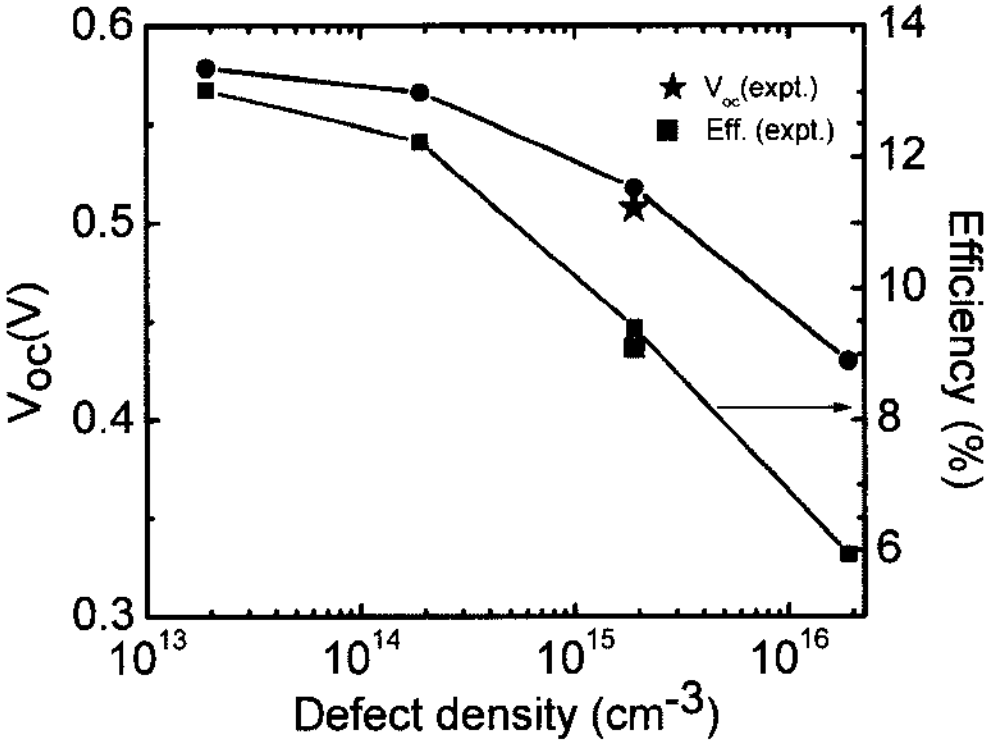

Fig 3.11: V_{oc} and efficiency with respect to defect density in the ultrathin (0.75 μm) CIGS solar cell.

3.5 Summary

CIGS thin films with various thicknesses from 1.95 μm down to 0.5 μm were deposited by co-evaporation. CIGS solar cells were then fabricated with the following standard structure: glass/Mo/CIGS/CdS/ZnO/ITO/grid. Cells with total area of 0.50 cm^2 were defined by mechanical scribing. The efficiency of the completed device was extracted from J-V measurements under 100 mW/cm^2, and the currents confirmed by QE measurements under white light bias. The current and voltage were roughly constant as thickness reduced from 1.95 μm to 1.3 μm, while decreasing for 0.75 μm and 0.5 μm. The reduction in J_{sc} is likely due to the reduction in absorbance in long wavelength. The observed decrease in V_{oc} could be due to the increase in shunt conductance with reduction of the CIGS absorber layer thickness. The experimental results for ultrathin CIGS solar cells indicate that the efficiency drops not only due to the decrease in Jsc, which is expected since the absorber layer gets thinner, but also due to decrease in Voc and FF. The degradation of the overall performance of the ultrathin CIGS solar could be due therefore to the combination of reduction in thickness of the absorber layer as well as the presence of impurities in the absorber layer. Numerical modeling of CIGS solar cells is an efficient way in order to verify the viability of created hypothesis depending on the physical explanations and to predict the effects of these physical changes on the solar cell performance. The simulated current-voltage characteristics of the ultrathin CIGS solar cells suggest that the deep states defects that lye in the upper part of the energy gap are responsible for the deterioration of the overall solar cell performance of the ultrathin CIGS solar cells.

CHAPTER 4

EFFECT OF DEPOSITION PROCESS ON ULTRATHIN CIGS FILMS AND DEVICES

4.1 Introduction and Motivation

With the highest small-area efficiency among the thin film photovoltaic (PV) technologies, $Cu(In,Ga)Se_2$ (CIGS) based solar cells have shown the greatest potential for success. CIGS technology is rapidly increasing its market share with the establishment of new CIGS solar cell companies. As this technology continues to expand, the scarcity and high price of indium can potentially hinder it from competing with other solar cell technologies. A potential solution to this problem is to decrease the amount of indium in the device by reducing the thickness of the film during fabrication [8], as we saw in the previous chapter. But ultrathin $Cu(In,Ga)Se_2$ films are grown by many different deposition techniques. The material properties of ultrathin $Cu(In,Ga)Se_2$ films are indeed different with different deposition processes. On a laboratory scale, the highest efficiency (21.7 %) [5] $Cu(In,Ga)Se_2$ solar cells are prepared by co-evaporation process. However, the co-evaporation process is not a straightforward technique and the characteristics of the grown films are different depending on the individual sources and substrate temperature. The properties of the ultrathin $Cu(In,Ga)Se_2$ film changes with the change in the atomic percentage (at.%) of Cu, In, Ga and Se, which depends itself on the evaporation conditions. Among the different co-evaporation techniques used to grow $Cu(In,Ga)Se_2$ films, the so-called 1-stage, 2-stage and 3-stage co-evaporation processes are the most successful processes. The highly efficient $Cu(In,Ga)Se_2$ solar cells are obtained with a particular

Cu/(In+Ga) ratio (0.90) and a particular Ga/(In+Ga) ratio (0.3). In order to achieve the required Cu and Ga at.% at the end of the 2-stage and 3-stage processes, it requires a precise control over the course of the deposition, the time of each sequence and the concentration of individual elements. Due to this complexity of these processes, and to study the material properties of ultrathin $Cu(In,Ga)Se_2$, we decided to evaluate the properties of ultrathin $Cu(In,Ga)Se_2$ thin films fabricated by 1-stage, 2-stage and 3-stage processes.

4.2 Deposition Process of CIGS

The co-evaporation process is the most successful technique used to fabricate high efficiency CIGS solar cell. This deposition process involves simultaneous evaporation of individual elements from multiple sources in a single or sequential process. The variation in Cu content strongly affects the film's growth, while there is only a minor change in the growth kinetics due to the variation of the Ga to In ratio during deposition process. So, many different co-evaporation growth techniques are categorized by their Cu evaporation profile. Ultrathin $Cu(In,Ga)Se_2$ films were deposited by 1-stage, 2-stage and 3-stage processes and the deposition processes of these ultrathin $Cu(In,Ga)Se_2$ films are explained in this section.

4.2.1 1-Stage Co-evaporation Process

This process is the simplest process in which all elementals flux as well as the substrate temperature is kept constant during the entire deposition process. During the deposition, the rate of individual elements is maintained almost constant without changing

the particular source temperature. In this process, ultrathin Cu(In,Ga)Se_2 films with different thickness are deposited by evaporating Cu, In, Ga and Se together by varying the deposition time. Ultrathin Cu(In,Ga)Se_2 films deposited by this process have uniform atomic percent for each of the elements all across the film.

4.2.2 2-Stage Co-evaporation Process

In this process, a Cu-rich growth phase is realized by supplying higher rate of Cu during the first stage. When the Cu(In,Ga)Se_2 is Cu-rich, a semi-metallic $Cu_{2-x}Se$ phase exists along with the Cu(In,Ga)Se_2 phase [47]. During the second stage, In and Ga are deposited at the same rate as in the first stage, without any Cu, to get a Cu-poor Cu(In,Ga)Se_2 thin film. The $Cu_{2-x}Se$ acts as the Cu sources in growing Cu(In,Ga)Se_2 during this stage and the film deposition is terminated whenever all the Cu from the $Cu_{2-x}Se$ is consumed. This process is the modified version of the Boeing process [48]. In the Boeing process, a Cu-rich Cu(In,Ga)Se_2 thin film is deposited during the first stage, followed by a stage with higher In and Ga, which is maintained until a Cu-poor Cu(In,Ga)Se_2 is obtained. So, only one transition occurs in this process. The End Point Detection (EPD) method is being used to identify the Cu-rich to Cu-poor phase's transition by monitoring the change in the substrate output power [49].

4.2.3 3-Stage Co-evaporation Process

In the 3-stage process, In, Ga and Se sources are first evaporated to form a (In,Ga)Se_x precursor. The Cu and Se sources are then used until a Cu-rich Cu(In,Ga)Se_2

film is obtained in a second stage. This Cu-rich $Cu(In,Ga)Se_2$ film is converted to Cu-poor $Cu(In,Ga)Se_2$ film in a third stage by evaporating In, Ga and Se. This process was first introduced by NREL and has been used to produce the highest-efficiency devices [49]. The $Cu(In,Ga)Se_2$ films deposited by three-stage process show relatively larger grain size and smoother surface morphology compared to 1-stage process. The smooth surface reduces the junction area, which tends to decrease the number of defects at the junction, yielding higher efficiency cells. The reaction pathway for the 3-stage co-evaporation is shown below [22]:

$$In\ (v) + Ga(v) + Se_n(v) \rightarrow (In_x,Ga_{1-x})_2Se_3(s)$$

$$Cu\ (v) + (In_x, Ga_{1-x})_2\ Se_3(s) + Se_n(v) \rightarrow Cu(In_xGa_{1-x})Se_2(s) + Cu_xSe(s)$$

$$Cu\ (In_xGa_{1-x})\ Se_2(s) + Cu_{2-x}Se(s) + In\ (v) + Ga(v) + Se_n(v) \rightarrow Cu(In_xGa_{1-x})Se_2(s)$$

A schematic of this process is shown in Figure 4.1. During the first stage, In, Ga and Se are deposited at a substrate temperature of 400 ^{0}C. Cu and Se are then evaporated until a Cu-rich $Cu(In,Ga)Se_2$ film is obtained in a second stage. The substrate temperature is raised to 570 ^{0}C for this second stage. Once the film becomes Cu-rich, the second stage is terminated. Then, in the absence of Cu flux, In and Ga along with Se are deposited at a substrate temperature of 570 ^{0}C until the film becomes Cu-poor. The first stage deposition time is chosen in such a way that the amount of In and Ga in the third stage should be around 10% of the total In and Ga deposited in the first and third stage [50]. As shown in figure 4.1 below, the thickness of the CIGS layer controlled by changing the duration of the first, second and third stages and the targeted composition leads to a ratio of $Cu/(In+Ga)=0.90$ and a ratio of $Ga/(Ga+In)=0.3$.

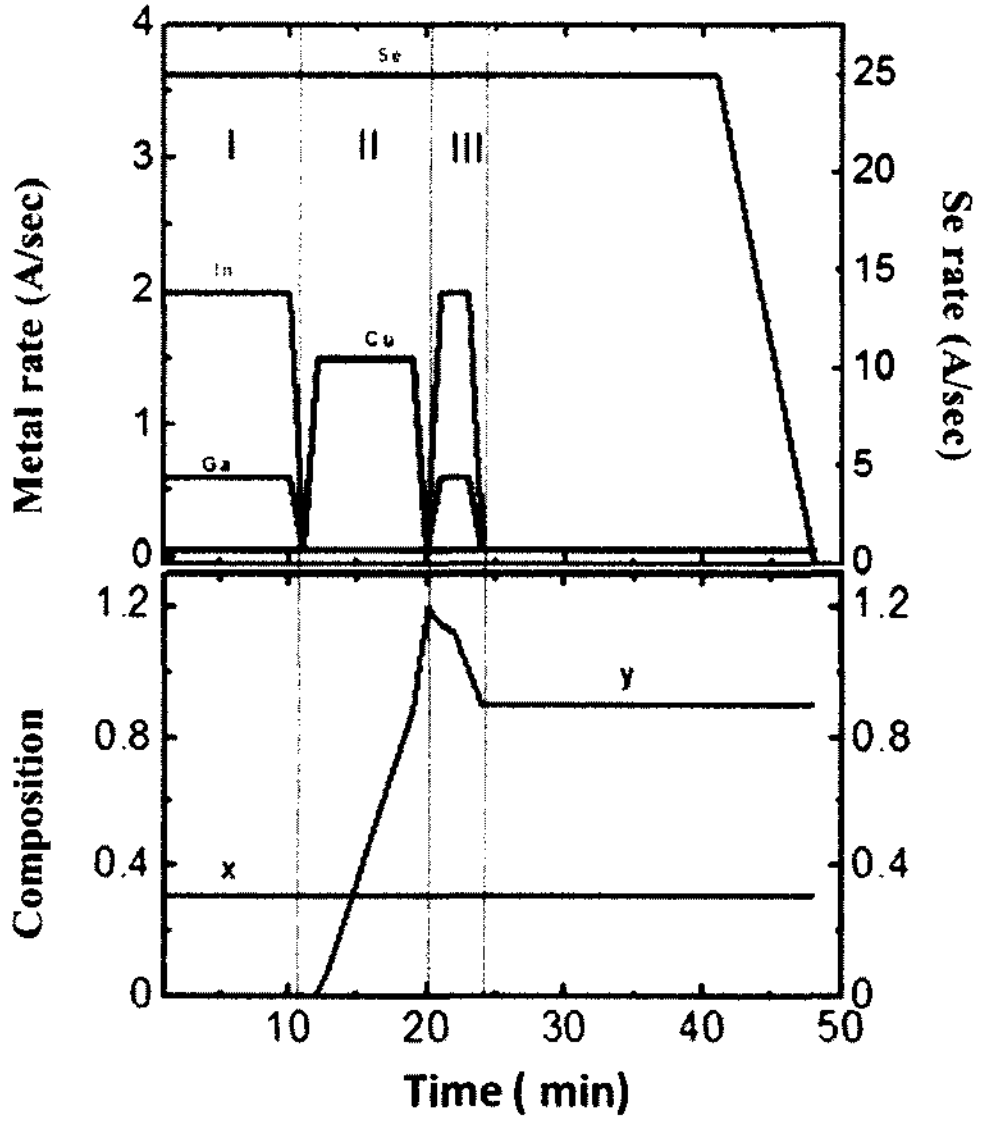

Figure 4.1 (Top) Rate of individual element during the 3-stage process; (bottom) Evolution of the composition of CIGS during the 3-stage process.

4.3 Characterization of Ultrathin CIGS Films and Devices Deposited by 1-Stage, 2-Stage and 3-Stage Co-evaporation Processes

Ultrathin CIGS films with similar thicknesses (~ 0.37 μm) were deposited by 1-stage, 2-stage and 3-stage co-evaporation processes. In the 1-stage process, all Cu, In, Ga and Se sources are co-evaporated simultaneously at a fixed rate for each and at a fixed

substrate temperature of T_{ss} = 550°C. In the 2-stage process, a Cu-rich growth phase is obtained by supplying a higher rate of Cu during the first stage. During the second stage, In, Ga and Se at the same rate as the first stage are deposited without any Cu to obtain a Cu-poor CIGS thin film. In the 3-stage process, In, Ga and Se are first co-evaporated to form a $(In,Ga)_xSe_y$ precursor film. Cu and Se are then co-evaporated until a Cu-rich CIGS film is obtained in a second stage. This Cu-rich CIGS film is converted to a Cu-poor CIGS film in the third stage by co-evaporating In, Ga and Se. The substrate temperature in first stage was kept at 400 °C and it was increased to 550 °C during the second and the third stages.

4.3.1 Studies of Ultrathin CIGS Films Deposited by 1-Stage, 2-Stage and 3-Stage Co-evaporation Processes by Real Time Spectroscopic Ellipsometer (RTSE)

The real time spectroscopic ellipsometry (RTSE) measurements were carried out in-situ during film growth using a rotating compensator, multichannel instrument with an energy range of 0.75 – 6.5 eV at an angle of incidence of 70°. Pairs of (ψ, Δ) spectra were collected with a 3-s acquisition time. The optical model for RTSE data analysis includes a continuous layer of thickness d_b with a bulk-like dielectric function, and a surface roughness layer of thickness ds whose dielectric function is determined from the Bruggeman effective medium theory as a 0.5/0.5 vol. fraction mixture of bulk material and void. The effective thickness or volume/area of film is defined as the bulk layer thickness plus one-half of the surface roughness layer thickness. The time evolution of (d_b, d_s) for ultra-thin films deposited by 1-stage, 2-stage and 3-stage co-evaporation is plotted in Fig. 4.2. For each process, film growth starts with the appearance of surface roughness in the

absence of a bulk-like layer. This behavior is interpreted in terms of nucleating clusters, associated with the Volmer-Weber growth mode. A comparison of the films in the nucleation stage reveals that the height of nuclei at the onset of coalescence is the lowest for films deposited by 2-stage process, where the Cu-rich growth phase is realized by supplying higher rate of Cu during the first stage. It is important to note that Cu-rich films are known to exhibit a semi-liquid $Cu_{2-x}Se$ phase at the substrate temperature used during deposition. The observed nucleation behavior therefore suggests that this semi-liquid phase increases the mass transport, enhancing the contact and coalescence of the nuclei, leading to a decrease in their height, hence smoothening the early-stage film surface [51].

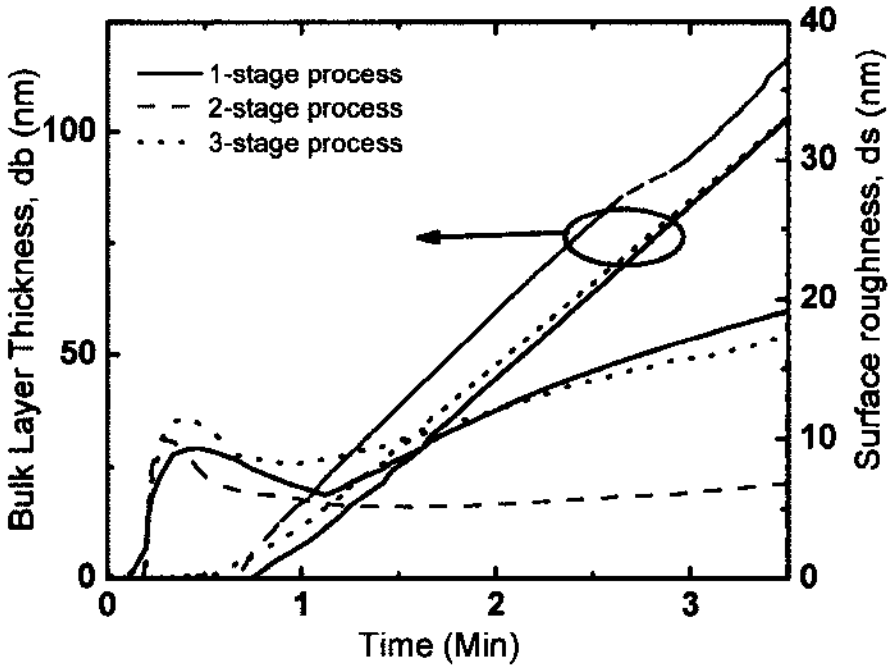

Figure 4.2 Evolution of the surface roughness d_s and the bulk layer d_b thicknesses with time obtained by RTSE for ultrathin $Cu(In,Ga)Se_2$ films deposited by 1-stage, 2-stage and 3-stage process.

Ex-situ measurements by variable angle SE were performed to extract the dielectric functions (ε_1, ε_2) versus energy for films deposited by 1-stage, 2-stage and 3-stage co-evaporation processes. Figure 4.3 shows the real and imaginary parts of the dielectric functions for $Cu(In,Ga)Se_2$ films deposited by these 3 different processes. The observed features in (ε_1, ε_2) in Figure 4.3 are associated with interband transitions that appear at the van Hove singularities or critical points (CPs) of the joint density of states [52]. These features were fitted assuming parabolic bands (PBs), yielding CPPB oscillators given by:

$$\varepsilon_j(\omega) = \begin{cases} C_j - A_j e^{i\phi_j}(\omega - E_j + i\Gamma_j)^n, & n = -1, -\frac{1}{2}, +\frac{1}{2} \\ C_j - A_j e^{i\phi_j}\ln(\omega - E_j + i\Gamma_j), & n = 0 \end{cases} \tag{4.1}$$

where A_j, ω_{ϕ}, E_j and Γ_j are the amplitude, phase, energy and broadening of the j^{th} oscillator The exponent n is -1, -1/2, 0, +1/2 for excitonic, 1D, 2D, and 3D critical points respectively. Here the fundamental transitions were fitted with excitonic CPs and the higher energy transition points were fitted with 2-dimensional CPs. The energy position of the lowest energy E_0(AB) CP (n=1) corresponding to the fundamental band gap is ~1.18 eV for CIGS films deposited by these processes (Table 4.1).

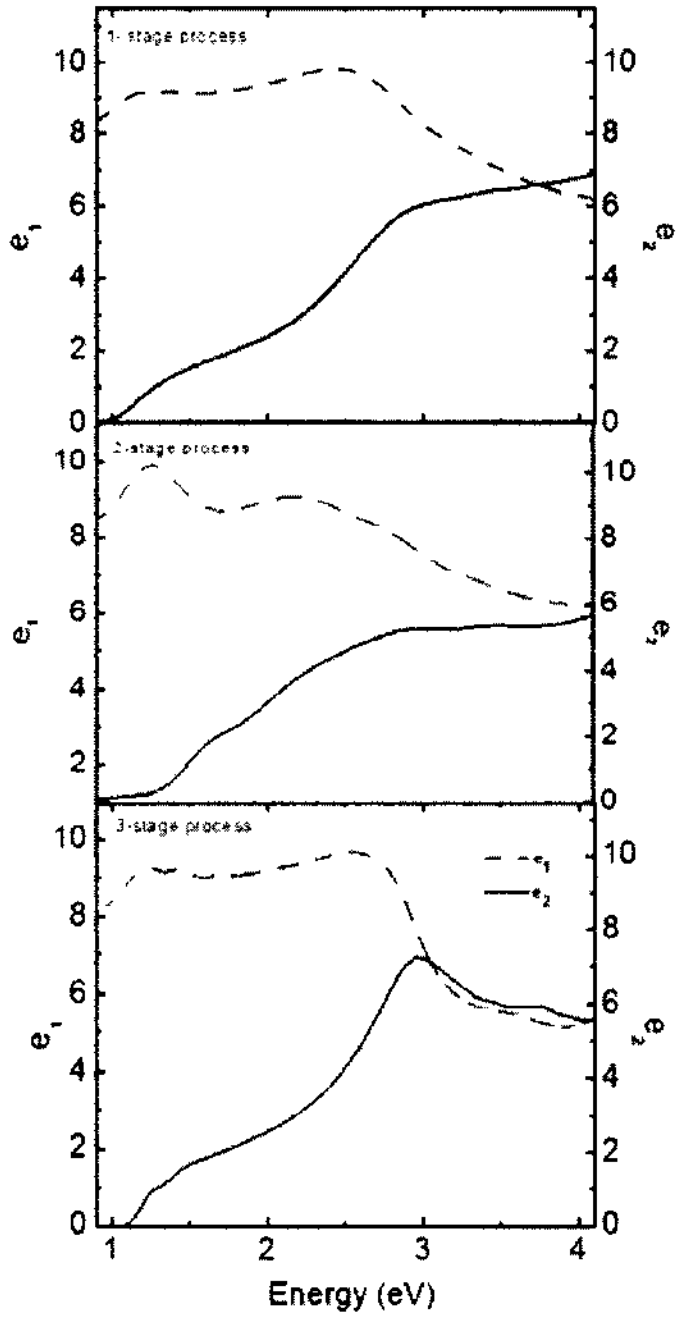

Figure 4.3 Real and imaginary parts of the dielectric functions for $Cu(In,Ga)Se_2$ films deposited by 1-stage and 2-stage process and 3-stage process

Another important parameter extracted from the same analysis is the broadening parameter of the CPPB oscillator, which is influenced by excited carriers interacting with phonons and other scatters such as grain boundaries. Hence the temperature and grain size can influence the broadening term. At constant temperature, the following equation relates the broadening and the grain sizes (R) [53]

$$\Gamma_C = \Gamma_g + \frac{hV}{R} \qquad (4.2)$$

where Γ_C is the broadening of the oscillator corresponding to the fundamental band gap, Γ_g is the corresponding parameter for a single crystal, V is the average group speed of the excited electron associated with the fundamental band gap and R is the grain radius. The values of broadening parameters and amplitude associated with the E_0(AB) critical point extracted by fitting the CPPB oscillators for Cu(In,Ga)Se_2 films prepared by 1-stage, 2-stage and 3-stage processes are shown in Table 4.1. The broadening values decreases from the 1-stage to the 3-stage process, which indicates that the grain size increases from the 1-stage to the 3-stage process. A large grain size is usually desirable for the best performance CIGS solar cells since grain boundaries are potential recombination centers for photogenerated electron-hole pairs.

Table 4.1 CP Energies, amplitude and broadening of CPs for Cu(In,Ga)Se_2 thin films

Processes	E_0(A,B) (eV)	Γ (eV)	Amplitude (eV)
1-stage	1.17	0.53	3.9
2-stage	1.17	0.34	4.0
3-stage	1.18	0.18	3.2

4.3.2 X-ray Fluorescence (XRF)

The compositions and thickness of each ultrathin CIGS films deposited by 1-stage, 2-stage and 3-stage processes were determined by using X-ray fluorescence (XRF). As explained in the previous chapter, XRF is the preferred technique for compositional analysis of CIGS thin films due to its ability to non-destructively measure the sample with excellent precision and less time requirement for the analysis. In addition to this compositional analysis, it can also be used to determine the thickness of the layers in thin multi-layer sample. Cu at.% around but less than 25, (In+Ga) at.% around 25 and Se at.% around 50 are required for high quality $Cu(In,Ga)Se_2$ films. Two main critical parameters extracted from these at.% are x = Ga/(In+Ga) and y = Cu/(In+Ga), where the x value determines the band gap of the ultrathin $Cu(In,Ga)Se_2$ films and the y value establishes the phase as well as the microstructure of the ultrathin $Cu(In,Ga)Se_2$ films. In Table 4.2 below, XRF measurements results for ultrathin $Cu(In,Ga)Se_2$ films deposited by 1-stage, 2-stage and 3-stage are listed.

Table 4.2 Typical XRF results for $Cu(In,Ga)Se_2$ thin films deposited by 1-stage, 2-stage and 3-stage processes

Process	Cu(at %)	In (at %)	Ga (at %)	Se (at %)	x=Ga/(In+Ga)	y=Cu/(In+Ga)
1-stage	22.2	17.4	7.3	52.1	0.33	0.90
2-stage	22.5	16.7	8.1	52.6	0.33	0.91
3-stage	22.8	17.5	7.8	51.8	0.31	0.90

The band gap of the CIGS thin film is calculated by the following relation [54]

$$Eg = 1.04 + 0.65\,x - 0.26x(1 - x) \qquad (4.3)$$

where the x values come from the XRF measurement as shown in Table 4.2, and where the band gap of $CuInSe_2$ is 1.04 eV, the one of $CuGaSe_2$ is 1.69 eV and the bowing parameter is 0.26. The band gap calculated from above equation (eq. 4.3) for the CIGS thin film deposited by 1-stage, 2-satge and 3-satge processes are ~ 1.18 eV which is fairly consistent with the band gap obtained using the spectroscopic ellipsometer (SE) analysis.

4.3.3 X-ray Diffraction (XRD)

X-ray diffraction (XRD) technique is used to find the structural properties of the films, the different phases present in the film, the crystallites orientation as well as the x values (x= Ga/(In+Ga)) in the films. X-ray diffraction in scanning mode of θ/2θ with Cu Kα-radiation (λ=0.15418 nm) was used for each of the $Cu(In,Ga)Se_2$ films deposited by 1-stage, 2-stage and 3-stage processes. Figure 4.4 compares the typical XRD spectra of $Cu(In,Ga)Se_2$ films deposited by 1-stage, 2-stage and 3-stage processes. All the films, within the limits of detection, were found to have a single phase tetragonal crystal structure.

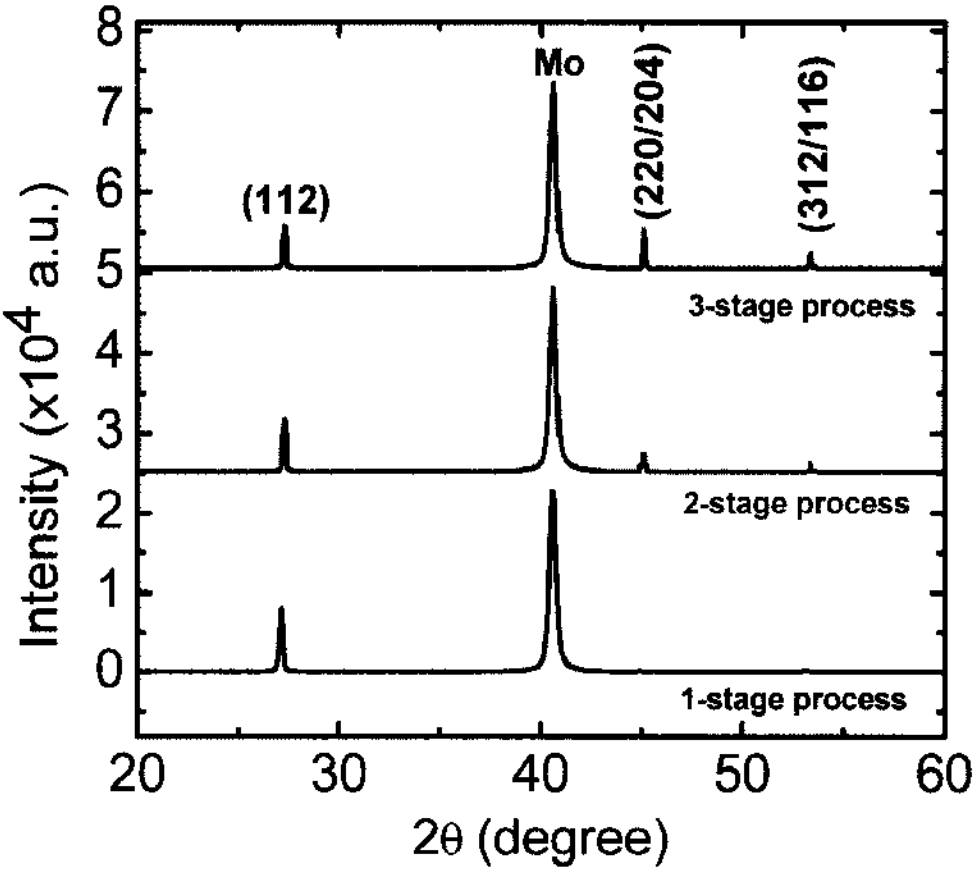

Figure 4.4 XRD pattern of ultrathin Cu(In,Ga)Se_2 films deposited by 1-stage, 2-stage, and 3-stage processes.

For tetragonal $Cu(In_{1-x}Ga_x)Se_2$ film, the lattice parameters a, c and their ratio c/a depend on the x=Ga/(In+Ga) values and follows the Vegard's rule [30]:

$$a(x) = (1 - x)a(0) + xa(1) \quad (4.4)$$

$$c(x) = (1 - x)c(0) + xc(1) \quad (4.5)$$

For the $CuInSe_2$ (x = 0), the lattice constants are a (0) =5.781 Å and c(0) = 11.619 Å while a(1) = 5.596 Å and c(1) = 11.003 Å for the $CuGaSe_2$ (x = 1). Since the lattice spacing d also changes with Ga concentration, a(x), c(x) and d(x) can be found for a given x and (h,k,l) values, whereas the experimental value of the lattice spacing for a particular peak

can be found by looking into the Joint Council for Powder Diffraction Studies (JCPDS) cards. So by matching the d values found from calculation for a given x to one found by matching the JCPDS card, we can correlate the x value to the XRD spectrum. The peak position, d-spacing and full width at half maximum (FWHM) for chalcopyrite (112) peaks are listed in Table 4.3.

The crystallites size can be predicted from XRD data using the Scherrer formula [55]:

$$D = \frac{K_s \lambda}{\beta \cos\theta} \qquad (4.6)$$

where D is grain size, Ks is Scherrer constant, β is the full width at half maximum of the peak in radians, λ is the wavelength of the X-ray beam and 2θ is the peak position. One can see that the FWHM decreases from 0.18 degree for the 1-stage process to 0.12 degree for the 3-stage process. For this work, λ is 1.54 Å corresponding to the Cu $K\alpha_1$ due to the use of a Cu source for the X-ray beam. Using the values of the FWHM from Table 4.3, the grain sizes calculated are 45 nm, 54 nm, and 58 nm respectively. This is in good correlation with the results obtained by RTSE (as shown in Figure 4.5). It was also observed that the $Cu(In,Ga)Se_2$ films deposited by the 1-stage process exhibited a preferred orientation along the (112) direction and that a slight (220)/(204) direction was observed for the films grown by the 2-stage or 3-stage processes. Researchers have found that the (220) preferred orientation can sometimes lead to higher efficiencies [56-57], which would explain in part why devices made with 2-stage and 3-stage are generally more efficient.

Table 4.3 XRD peak properties of chalcopyrite (112) for CIGS films deposited by 1-stage, 2-stage and 3-stage processes

Sample	Peak Position [deg]	d- spacing [A°]	Peak Height [cps]	FWHM [deg]
1- stage	27.04	3.2832	5634	0.18
2 -stage	27.07	3.2659	2295	0.15
3 -stage	27.08	3.2548	1985	0.12

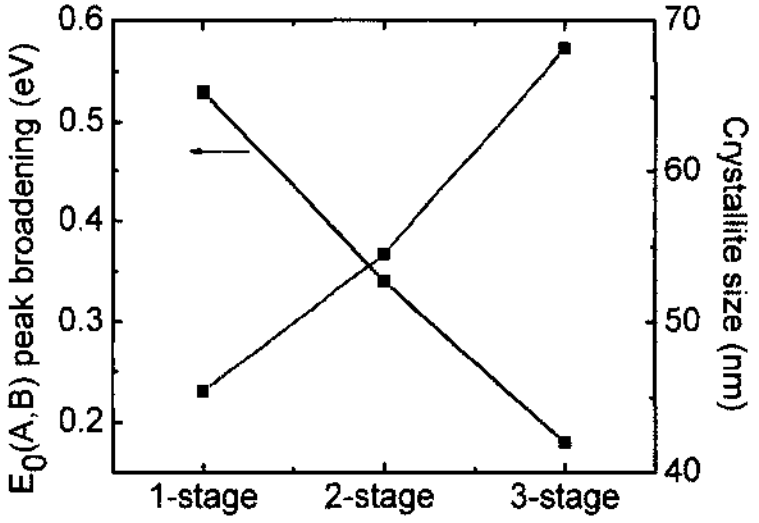

Figure 4.5 E_0 (A, B) peak broadening from RTSE data analysis and grain size calculated from XRD measurement.

4.3.4 Current Density –Voltage (J-V) Measurement

The efficiency of the completed solar cell device is extracted from the current and voltage measurement (J-V) measurement. The measurement is performed at room temperature and under a standardized "One Sun" illumination. Typical J-V results of ultrathin devices fabricated from CIGS thin films deposited by 1-stage, 2-stage and 3-stage

processes are plotted in Figure 4.6 and summarized in the Table 4.4 below. The device with ultrathin $Cu(In,Ga)Se_2$ deposited by a 1-stage process has the lowest V_{OC}. The lower V_{OC} for the devices with ultrathin CIGS deposited by 1-stage process may be attributed to large grain boundaries (GB) per unit volume as well as degradation of junction quality [31]. The decrease in fill factor and V_{oc} for the devices with ultrathin CIGS deposited by 1-stage process could also be due to the smaller grain sizes, more and higher defect densities. The grain boundaries act as a recombination center which would reduce the Voc.

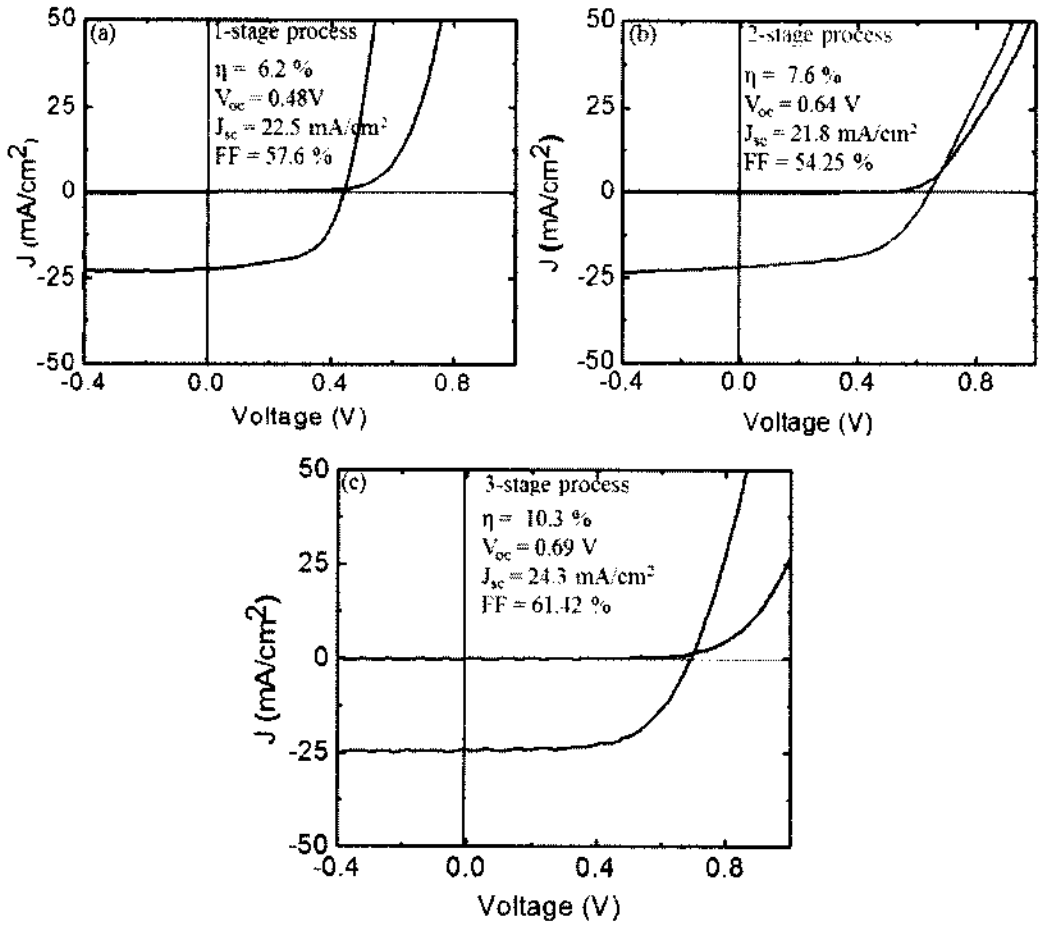

Figure 4.6 Typical light and dark J-V curve for device fabricated from ultrathin CIGS film deposited by (a) 1-stage process, (b) 2-stage process, and (c) 3-stage process. The thickness for all ultrathin CIGS layers is ~ 0.7 μm. There is no MgF_2 anti-reflecting coating.

Table 4.4 Summarized device parameters of ultrathin CIGS solar cell deposited by 1, 2 and 3-stage processes

Processes	V_{oc} (V)	J_{sc} (mA/cm^2)	Fill Factor (%)	Efficiency (%)
1-stage	0.48	22.5	57.6	6.2
2-stage	0.64	21.8	54.2	7.6
3-stage	0.69	24.3	61.4	10.3

As one can see in Table 4.4, the solar cell fabricated from ultrathin Cu(In,Ga)Se_2 deposited by 3-stage process has better device performance. This improved device performance has been attributed to a band gap gradient due to Ga (the Ga/(In+Ga) grading, which is achieved by varying the deposition time of Cu, In and Ga fluxes. The effects of Ga/(In+Ga) on the band gap of CIGS thin film is given by the following relation [54]:

$$E_g = 1.04 + 0.65x - 0.26x(1-x) \qquad (4.7)$$

Where x is Ga/(In+Ga). The band gap of $CuInSe_2$ is 1.04 eV, and $CuGaSe_2$ is 1.68 eV and the bowing parameter is 0.26. The ultrathin CIGS deposited by 3-stage process has a wider band gap at the front and back interfaces. The increase in the band gap at the CIGS and Mo interface is due to the up lift of the conduction band minima while the valance band maxima remain the same [24]. Due to the increment in the band gap toward the back interface (dEg/dx), there is an increase in the electric force due to an extra electric field, which pushes the electrons towards the p-n junction of the device. This in turns reduces the recombination towards the back interface and hence enhances the current collection and the V_{oc} [50].

The relation between V_{oc} and the short circuit current is given by the following equation [58]:

$$V_{oc} = \frac{E_g}{q} - \frac{AkT}{q}\ln\left(\frac{J_{00}}{J_{sc}}\right) \tag{4.8}$$

Where J_{sc} is the short circuit current density, J_{00} is the diode saturation current density. The V_{oc} in the above equation is correlated with the band gap in the space charge region. So an increment in the band gap near the junction is expected to enhance the V_{oc} [59], but a reduction in current can also occurred due to the decrease in the absorption of the solar spectrum. However, there was no loss in the current in our work due to the increase in the band gap for the ultrathin CIGS device deposited by 3-stage process. Similar results were observed by numerical simulation studies on CIGS [60]. It has also been observed that the J_{sc} in the graded band gap is correlated to the minimum band gap [60]. The schematic energy-band diagrams for a typical ZnO/CdS/CIGS solar cell with a uniform and graded CIGS are shown in figure 4.8. In figure 4.7 (b), a quasi-electric field [61] can be established by the band-gap gradient with higher band gap towards the back contact (Mo) region by reducing the back surface recombination and increasing the effective minority-carrier diffusion length. This would help to enhance both V_{oc} and J_{sc}. The front grading would increase the band gap in the space charge region (SCR) where the most of the recombination occurs. This would help to increase V_{oc}. So the improvement in the device performance of ultrathin CIGS deposited by 3-stage process would be due to the graded CIGS absorber layer.

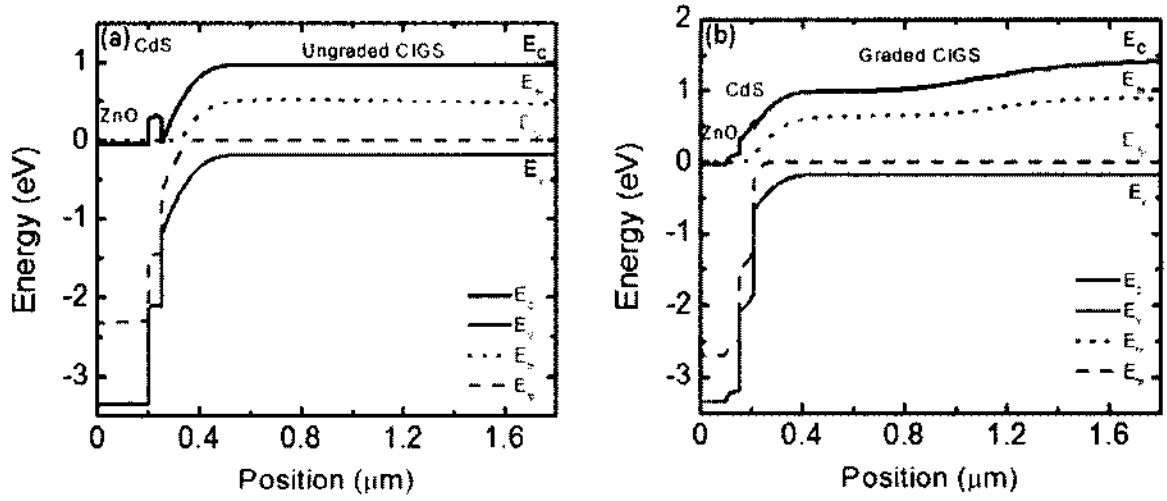

Figure 4.7: (a) The schematic energy band-diagram of a CIGS solar cell with (a) ungraded CIGS and (b) graded CIGS.

4.3.5 Quantum Efficiency (QE) Measurements

Through spectrally resolving the current yield of a solar cell device, quantum efficiency provides a closer understanding of the short circuit current and the loss mechanisms restricting it. The quantum efficiency of the standard CIGS solar cells is controlled by the band gap of the CIGS absorber layer, the CdS buffer layer and ZnO window layer and a series of loss mechanisms such as reflection, grid shading, incomplete collection, and incomplete generation. The light-generated current is the integral of the product of the quantum efficiency and the illumination spectrum, which is given below [27]:

$$J_{sc} = q\int \Phi_{AM1.5}(\lambda) QE(\lambda) d\lambda \qquad (4.9)$$

where $\Phi_{AM1.5}$ is the photon flux at AM1.5 condition and QE is the ratio of the number of electrons collected to the number of photons incident. Real QE measurements are generally

lower than the one we get from the above equation under ideal condition. In Figure 4.8 are shown QE measurements for solar cells deposited by 1, 2 and 3-stage processes.

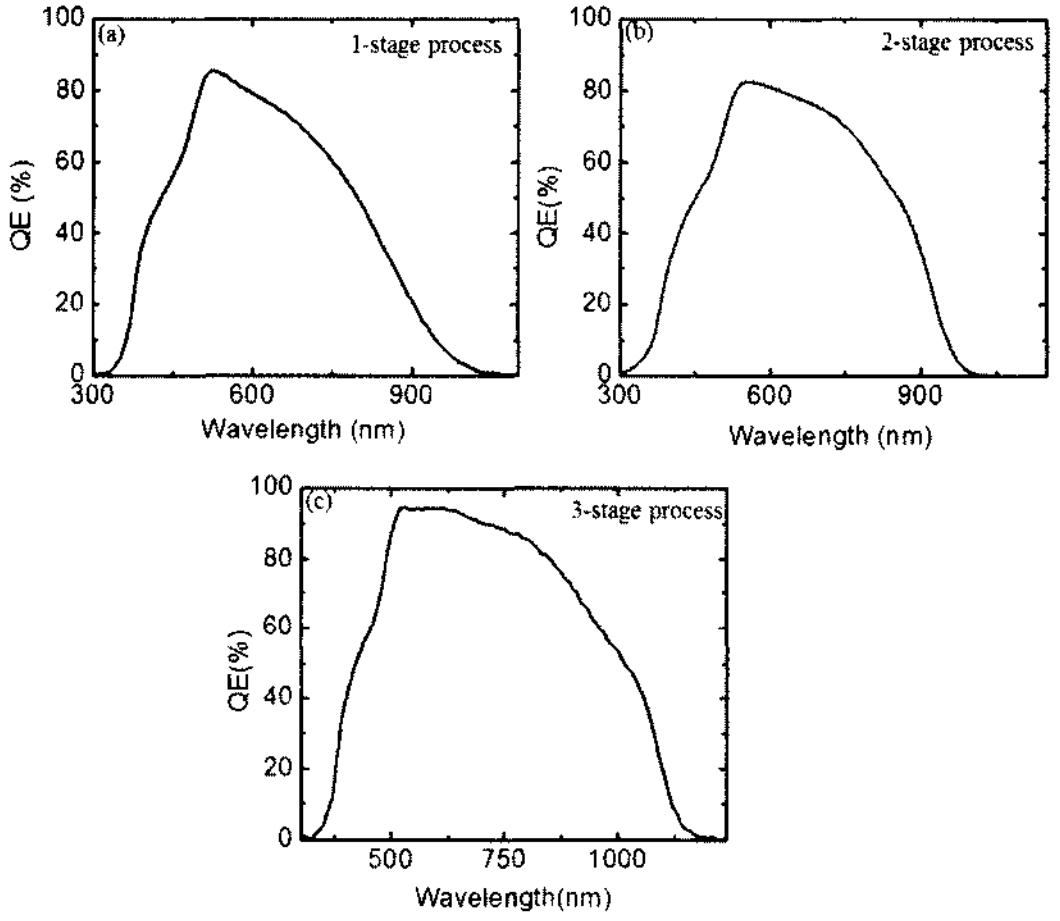

Figure 4.8 Quantum efficiency curve for device fabricated from ultrathin CIGS film deposited by (a) 1-stage process (b) 2-stage process, and (c) 3-stage process. Thicknesses of the ultrathin CIGS layers are ~ 0.7 μm.

The losses in the current as shown in Figure 4.8 include the following [17]:

i) Front surface losses are introduced by partial coverage of the front surface by the metal contact fingers or by reflection from the material interface. Such losses can

be reduced by depositing a thin anti-reflecting coating or by thinning down the size of the fingers.

ii) Absorption in the window layer (ZnO/AZO) region is not significant due to the high band-gap energy of ZnO/AZO. There is 1-3% absorption through the visible wavelengths which increases in the near IR region (>900 nm) where free-carrier absorption becomes significant and for UV region (<400 nm) near the ZnO band gap. Such losses can be reduced by thinning the layers. If the thicknesses of the window layers are reduced significantly there are chances of damaging the junction between CdS and CIGS, shunting through i-ZnO layer and reduction in current collection due to increase in sheet resistance in the AZO layer. So there must be a balance between the optical losses and the electrical losses.

iii) Absorption in CdS is one of the major losses in thin-film solar cells (CIGS). This loss becomes appreciable at wavelengths below ~ 520 nm which corresponds to the band gap of CdS (2.42 eV). The loss in QE for $\lambda < 500$ nm is directly proportional to the thickness of the CdS since electron-hole pairs generated in the CdS are not collected in the device. Figure 4.8 shows QE for the solar cell device with a CdS ~ 50 nm thick. Reducing the thickness of the CdS or replacing it with a higher band-gap material such as ZnS would be the possible alternatives to reduce the loss in the device.

iv) Optical loss in the ultrathin CIGS is more pronounced than the standard CIGS device (~ 2 μm) due to the incomplete absorption near the band gap of the CIGS. Long wavelength photons needs to penetrate deep into the CIGS thin film before being absorbed. This loss can be reduced in ultrathin CIGS by making high quality

material since CIGS thickness should be reduced to lower the indium consumption as well as to the production cost. As shown in the Figure 4.8 (a), there is the significant loss in the current after 800 nm in the ultrathin CIGS device deposited by 1-stage process in comparison to the ultrathin CIGS device deposited by 3-stage process. This could be due the improvement in the material quality of the ultrathin CIGS deposited by 3-stage process [40].

v) Electrical loss in the ultrathin CIGS layer is due to the incomplete collection of the charge carrier. This loss is also called the recombination loss since it is introduced due to traps or due to a low diffusion length of the absorber layer. QE in CIGS is given by [27]

$$QE_{ext}(\lambda, V) = [1 - R(\lambda)][1 - A_{ZnO}(\lambda)][1 - A_{CdS}(\lambda)]QE_{int}(\lambda, V) \quad (4.10)$$

Where R is the total reflection including the grid shading, A_{ZnO} is the absorption in the ZnO layer, A_{CdS} is the absorption in the CdS layer, QE_{int}, the internal quantum efficiency which is the ratio of photo generated carriers collected to the photon flux that arrives at the absorber layer and can be approximated by assuming that all carriers generated in the space charge region are collected without recombination loss [17]:

$$QE_{int}(\lambda, V) = 1 - \exp[-\alpha(\lambda)(W(V) + L_{diff})] \quad (4.11)$$

Where α is the CIGS absorption coefficient, W is the space charge width in the CIGS (which varies from 0.1- 0.5 μm for typical cells at 0V) and L_{diff} is the minority-carrier

diffusion length. If the effective collection length, L_{eff} = W (V) + L_{diff} is smaller than 1 μm, carriers are not collected and the QE decreases at longer wavelength since a significant fraction of electrons is generated deeper in the CIGS layer than the collection length due to the decreasing absorption coefficient [17]. As observed in Figure 4.8, the current loss due to incomplete absorption at long wavelength becomes significant for the ultrathin CIGS device with 0.7μm thick CIGS layer. With these ultrathin absorber layers, the back contact can significantly affect the device behavior. Using an alternative back contact with high reflection on the ultrathin CIGS would help to increase the current closer to the values for 2 μm thick films.

4.4 Effect of Selenium Pressure on Ultra-thin CIGS Solar Cell Thin Films

4.4.1 Introduction and Motivation

As explained in the previous chapter, many different methods for depositing CIGS thin films have been tried until now but co-evaporation of elemental sources is the most successful process for achieving high quality material for CIGS. This process requires a precise control of the elemental compositions in the vapor flux. To achieve high quality in ultrathin CIGS films, this can be a challenge due to the low sticking coefficient of selenium. The texture of CIGS thin films also depends on the selenium flux as well as on the Na supply during the deposition process [62]. CIGS thin film prepared with low selenium flux exhibited very low Cu content, small grain size and poor solar cell performance [63]. Stoichiometry is one of the major concerns in ultrathin CIGS solar cell fabrication and can affect significantly the cell performance. It is therefore very important to find the minimal selenium flux for obtaining good quality CIGS thin films. CIGS films, with thicknesses of

2.1 μm and 0.3 μm, were deposited by a 2-stage co-evaporation process under various selenium/metal flux ratios, varying from 3 to 9. The elemental fluxes were calibrated before each deposition. The Se effusion flux was adjusted by changing the Se source temperature to obtain selenium/metal flux ratios (SMR) of 3, 5 and 9. The target composition ratios of Cu/(In+Ga) and Ga/(In+Ga) were kept near 0.9 and 0.3, respectively.

4.4.2 Selenium Flux Effect on Ultra-thin CIGS Solar Cell Thin Films analyzed by Real Time Spectroscopic Ellipsometry (RTSE)

The real time spectroscopic ellipsometry (RTSE) measurements were carried out *in-situ* during CIGS thin film growth under various selenium/metal flux ratios using a rotating compensator, multichannel instrument with an energy range of 0.75–6.5 eV at an angle of incidence of 70°. Pairs of (ψ, Δ) spectra were collected with a 3-s acquisition time. The optical model for RTSE data analysis includes a continuous layer of thickness d_b with a bulk-like dielectric function, and a surface roughness layer of thickness d_s whose dielectric function is determined from the Bruggeman effective medium theory as a 0.5/0.5 vol. fraction mixture of bulk material and void. The effective thickness or volume/area of film is defined as the bulk layer thickness plus one-half of the surface roughness layer thickness.

Ex-situ spectroscopic ellipsometry data were acquired after film growth using a rotating-compensator multichannel ellipsometer with a photon energy range of 0.75 - 6.5 eV at angles of incidence of 50°, 60° and 70°. Pairs of (ψ, Δ) spectra were collected with an acquisition time of 3 s. Analyses of the spectra involved numerical inversion and least-squares regression algorithms. The optical model for the film in this case also consisted of

a bulk layer whose dielectric function is determined in the analysis and a surface roughness layer whose dielectric function is determined from an effective medium theory as a 0.5/0.5 volume fraction mixture of the bulk layer and void.

The time evolution of (d_b, d_s) for ultra-thin films deposited by varying the Se/metal flux ratio from 3 to 9 is shown in Fig 4.9. Initial growth of all films is in the form of islands and then these islands continue to grow until the beginning of coalescence, as indicated by a decrease in d_s with a commensurate increase in d_b. Subsequently, the films continue to smoothen as d_b increases. During this process, film growth commences with the appearance of surface roughness in the absence of a bulk-like layer. This behavior is interpreted in terms of nucleating clusters, associated with the Volmer-Weber growth mode. In figure 4.9, it was observed that the growth rate decreases as the Se flux rate increases. This could be due to gas phase scattering during the growth of CIGS with higher Se flux. As the Se flux rate increases, the Se atoms in the gas phase scatter the metal atoms before they are able to reach the surface, resulting in the observed decrease in the film growth rate [64].

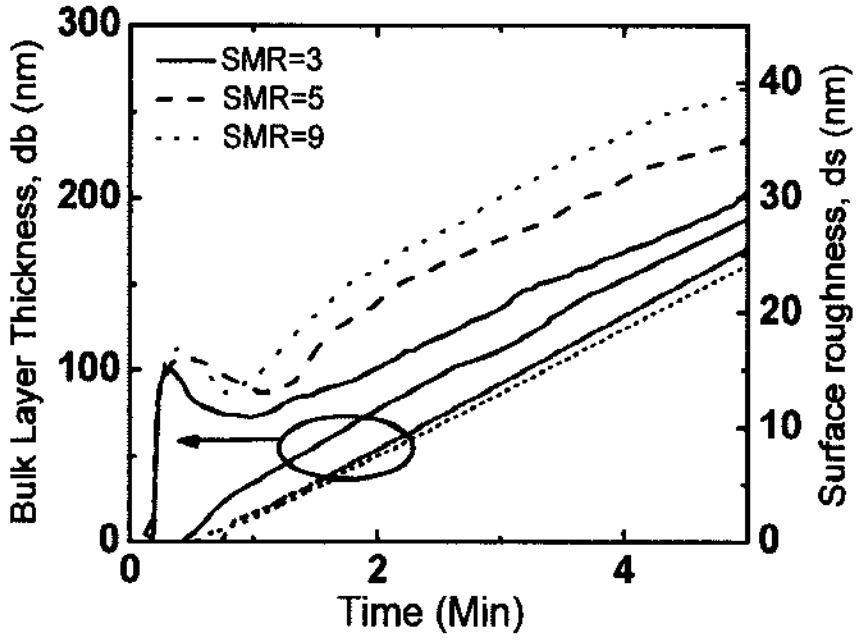

Figure 4.9: Time evolution of the surface roughness thickness, d_s, and the bulk layer thickness, d_b, for $Cu(In,Ga)Se_2$ ultrathin films deposited at different SMR.

The complex dielectric functions (ε_1, ε_2) for CIGS thin films deposited at SMR = 3, 5 and 9 are shown in Figure 4.10. The observed features in (ε_1, ε_2) in Fig. 4.10 are associated with interband transitions that appear at the van Hove singularities or critical points (CPs) of the joint density of states [65]. These features were fitted assuming parabolic bands (PBs), yielding CPPB oscillators given by:

$$\varepsilon_j = \begin{cases} C_j - A_j e^{j\varphi_j}(\omega - E_j + i\Gamma_j)^n \\ C_j - A_j e^{j\varphi_j} \ln(\omega - E_j + i\Gamma_j), \end{cases} \qquad (4.12)$$

where A_j is the amplitude, E_j is the energy, Γ_φ is the broadening, and ϕ_j is the phase, all for the j^{th} critical point. The exponent n is $-1, -1/2, 0$ (ln), or $+1/2$ for excitonic, 1-dimensional, 2-dimensional, or 3-dimensional CPs, respectively. Here the fundamental transitions were fitted with excitonic CPs and the higher energy transition points were fitted

with 2-dimensional CPs. In Fig. 4.10, it was observed that there is no significant shift in the E_0(A,B) or E_0(C) CP energies for the different Se fluxes. This is consistent with transmission and reflection measurements whereby no change was observed in the absorption onset for these films. The broadening parameter of the CPPB oscillator, which is influenced by excited carriers interacting with phonons and other scatterers, such as grain boundaries was extracted. At constant temperature, the following equation relates the broadening and the grain sizes (R) [53]:

$$\Gamma_C = \Gamma_g + \frac{hV}{R} \tag{4.13}$$

Where Γ_C is the broadening of the oscillator corresponding to the fundamental band gap, Γ_g is the corresponding parameter for a single crystal, V is the average group speed of the excited electron associated with the fundamental band gap and R is the grain radius. The extracted values of broadening parameters and amplitudes associated with the E_0(A,B) critical point are shown in Table 4.5. These results were obtained by fitting the CPPB oscillators for Cu(In,Ga)Se_2 films prepared by varying Se flux rate, The extracted values of broadening parameters associated with the E_0(A,B) critical point for CIGS films prepared at SMR = 3, 5 and 9 are 0.57 eV, 0.32 eV and 0.27 eV, respectively. These values indicate that the grain size increases with increasing Se flux. The same trend was also corroborated by inspection of both SEM cross-sectional images and the full width at half maximum (FWHM) of the diffraction peaks in XRD analysis.

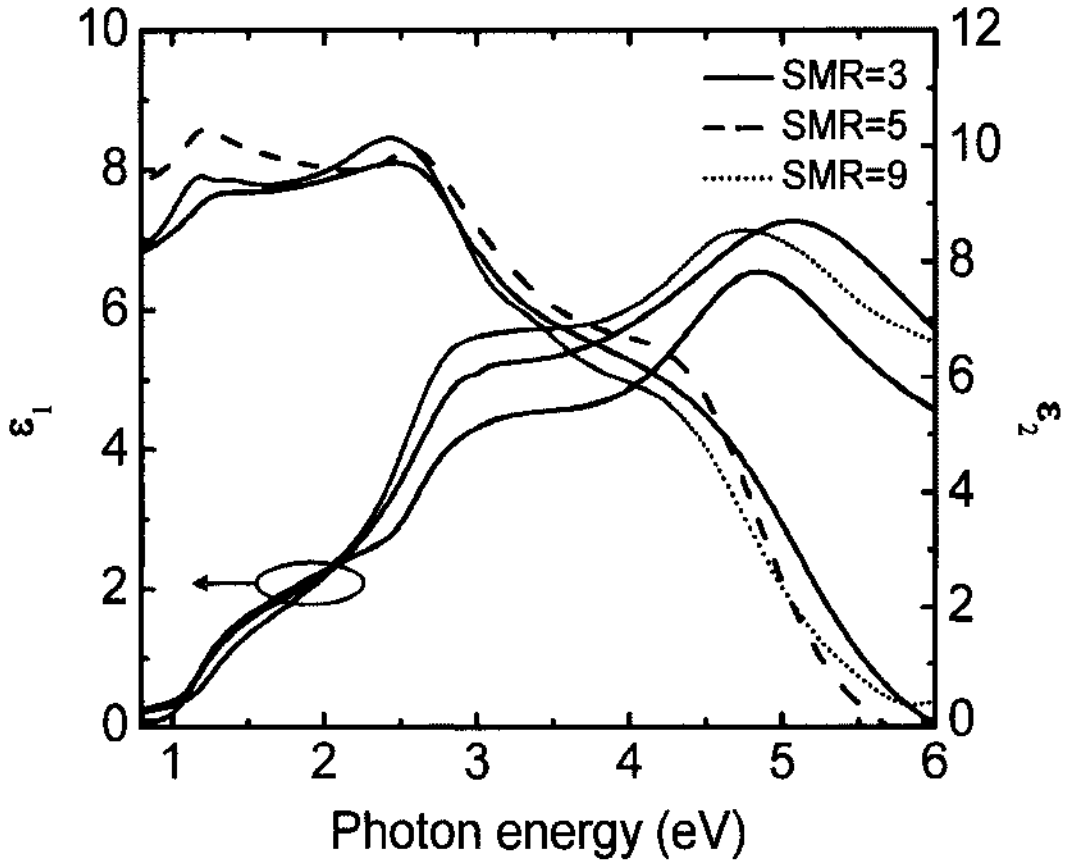

Figure 4.10 Real and imaginary parts of the dielectric functions for ultra-thin Cu(In,Ga)Se_2 films deposited at different SMR.

Table 4.5 CP energies, broadenings and amplitudes of CPs for Cu(In,Ga)Se_2 ultrathin films

Samples	E_o(A,B) (eV)	Γ (eV)	Amplitude (eV)
SMR = 3	1.19	0.57	2.2
SMR = 5	1.18	0.32	1.5
SMR = 9	1.17	0.27	2.0

4.4.3 Characteristics of CIGS thin films as a Function of SMR

The composition of each of the films was determined by XRF technique as described earlier. XRD measurements were also used to determine the x=Ga/(In+Ga) ratio in the films from the lattice parameters. Figure 4.11 shows the surface and cross-sectional SEM images of $Cu(In,Ga)Se_2$ thick film (thickness ~ 2.1 μm) deposited by varying the Se/metal flux ratio from 3 to 9. In these surface images, the small crystallite size of the CIGS film deposited with low Se is apparent. The medium and high Se CIGS thin films have similar grain sizes even though the texture of the high Se is slightly rougher. From the cross-sectional images, ordered columnar grains were observed for the CIGS film deposited under higher Se flux. Grains are smaller in size for the film grown with low Se flux. The variation in grain size with Se flux can notably affect the electrical properties of the CIGS film [66]

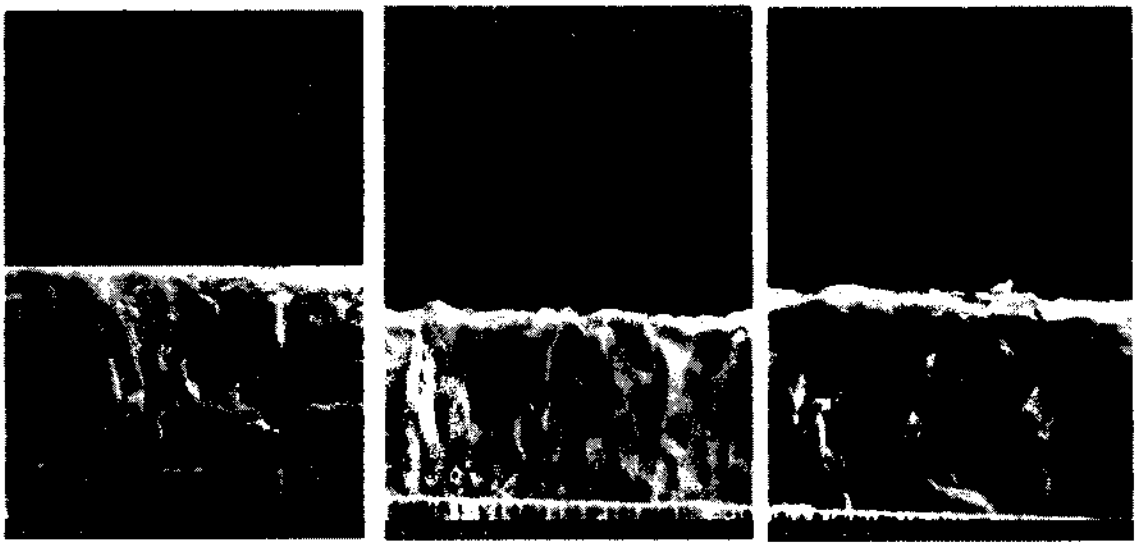

Figure 4.11 Surface and cross-sectional SEM images of CIGS thin films deposited with different SMR

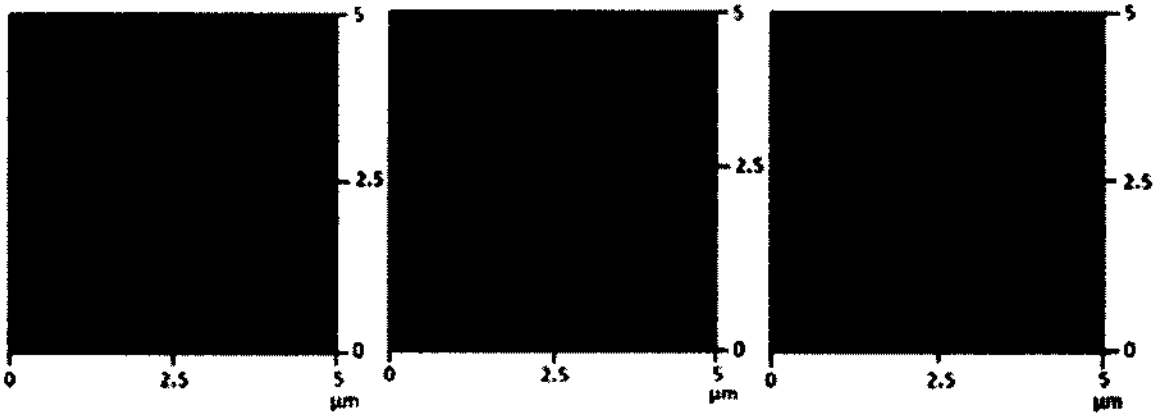

Figure 4.12 AFM images of CIGS films deposited with different SMR

Figure 4.12 shows the surface morphology measured by AFM of the CIGS thin films deposited by varying the Se/metal flux ratio from 3 to 9. The surface roughness thicknesses extracted from RTSE data were not the same as those measured by AFM but a linear correlation is observed. This is shown in Figure 4.13 and mathematically expressed as $d_s(SE) \sim 1.2\ d_{rms}(AFM)$.

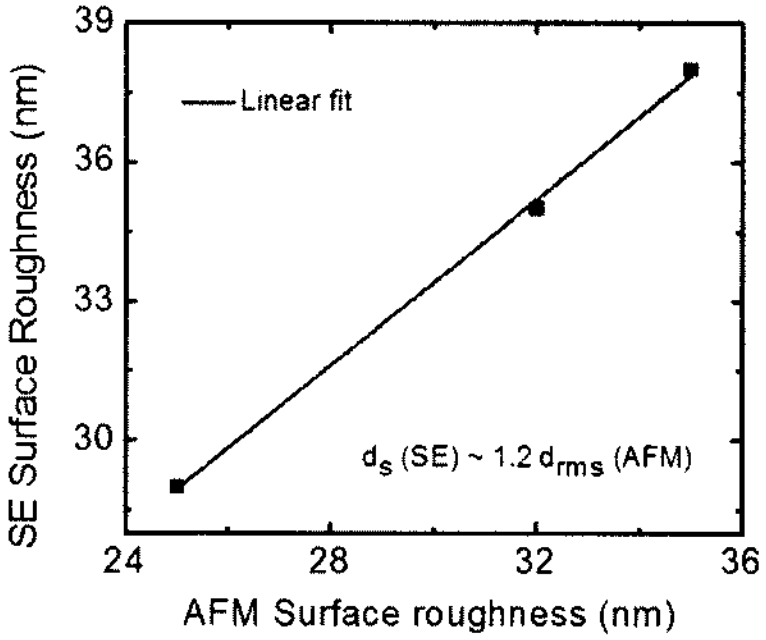

Figure 4.13 Surface roughness ds from RTSE plotted as a function of the root mean square roughness d_{rms} measured by AFM

Figure 4.14 shows the XRD patterns of CIGS thick films (thickness ~ 2.1 μm) deposited on glass substrates by 2-stage co-evaporation at SMR = 3, 5 and 9. The main peaks appearing correspond to the (112), (220)/(204) and (312/116) planes of the chalcopyrite structure. The peak position, d-spacing and full width at half maxima (FWHM) for the chalcopyrite (112) peaks are listed in Table 4.6. The FWHM decreases from 0.31 degree to 0.18 degree when the SMR increases from 3 to 9. This indicates that the grain size increases as Se rate increases in CIGS thin film, as observed by SE. It was also observed that the preferred orientation was (220) for the film with higher Se flux while it tended to be (112) with lower Se flux. These results indicate that the Se flux rate significantly influences the crystal growth of CIGS.

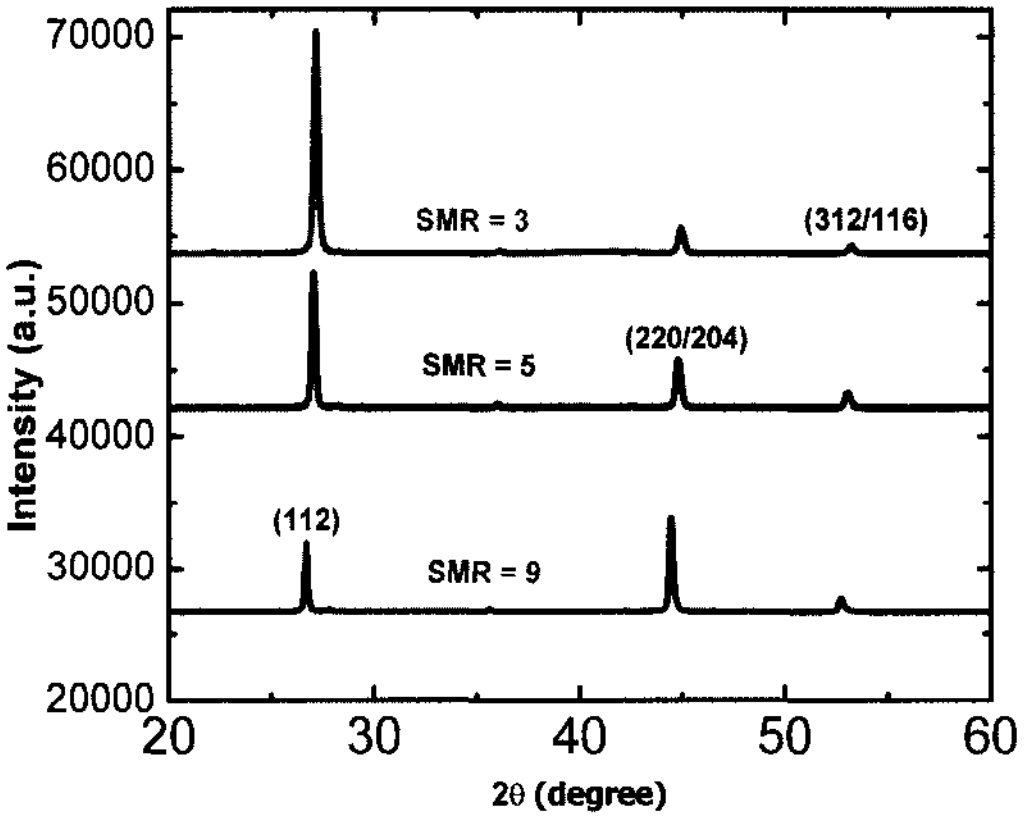

Figure 4.14 Typical XRD pattern for $Cu(In,Ga)Se_2$ thick film deposited under different selenium metal flux ratios

Table 4.6: XRD chalcopyrite (112) peak properties of CIGS films deposited under different Se rate

Sample	Peak Position [deg]	d- spacing [A°]	Peak Height [cps]	FWHM [deg]
SMR=3	27.09	3.24	5413	0.319
SMR=5	27.03	3.27	7243	0.205
SMR=9	26.68	3.31	2234	0.189

Figure 4.15 shows the electrical resistivity and carrier concentration of CIGS films as functions of SMR. All CIGS films showed p-type conductivity. It was observed that the hole concentration of the CIGS film increased and resistivity decreased with increasing Se

flux. It was reported that the anion vacancy, V_{Se}, which acts as a donor, may be created in the CIGS film due to a Se deficiency [66]. V_{Se} is therefore one of the probable reasons for the decreasing hole concentration in the CIGS film grown with decreasing SMR. The higher SMR was found to be preferable in order to obtain better material properties to enhance the CIGS solar cell performance.

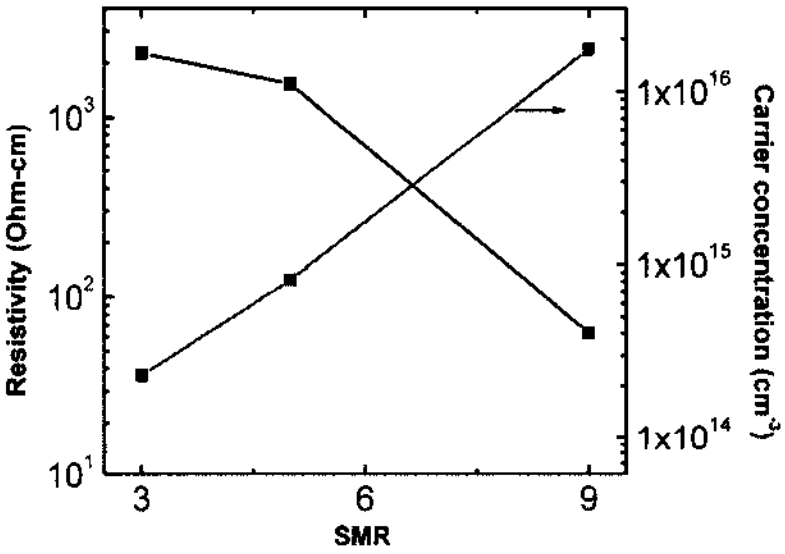

Figure 4.15 Resistivity and hole concentration of CIGS thin films as a function of SMR

4.5 Summary

The ultrathin CIGS films deposited by 1-stage, 2-stage and 3-stage co-evaporation processes were explored by in-situ spectroscopic ellipsometry via the real time monitoring of the dielectric functions, the thickness, and the roughness. Ultrathin CIGS with thickness ~ 0.7 μm were deposited by 1-stage, 2-stage and 3-stage co-evaporation processes and spectroscopic ellipsometry data were acquired with an energy range of 0.75–6.5 eV. Irrespective of the process, the initial nucleation stages of these ultrathin films show island growth or the Volmer-Weber (V-W) growth process. A comparison of the films in the

nucleation stage reveals that the height of nuclei at the onset of coalescence is the lowest for films deposited by 2-stage process, where the Cu-rich growth phase is realized by supplying higher rate of Cu during the first stage. The observed nucleation behavior therefore suggests that this semi-liquid phase increases the mass transport, enhancing the contact and coalescence of the nuclei, leading to a decrease in their height, hence smoothening the early-stage film surface. Material properties of these ultrathin Cu(In,Ga)Se2 films deposited by 1-stage, 2-stage and 3-stage co-evaporation processes were characterized and compared using different optical and electrical characterization techniques such as spectroscopic ellipsometry (SE), XRD and AFM. Out of these three processes, the 3-stage process proved to be the best for growing device quality ultrathin $Cu(In,Ga)Se_2$ films. The solar cells processed from these ultrathin CIGS films with thickness ~ 0.7 μm were also characterized to compare the efficiency, voltage and current. Current-voltage (J-V) and quantum efficiency (QE) measurements on these ultrathin CIGS solar cells helped us in understanding the reason for different efficiencies. Larger grain size, improved junction interface as well as Ga grading were some of the reasons for better efficiency of the solar cells processed from ultrathin CIGS deposited by 3-stage process.

Ultrathin and thick CIGS films deposited under various Se effusion rates were also studied by real time spectroscopic ellipsometry (RTSE) and ex-situ measurement. The surface morphology of the CIGS film was affected by Se flux rate. The grain size increases as Se rate increases. It was observed that the preferred orientation became (220) for the film with higher Se flux while it tended to be (112) with lower Se flux. These indicate that the Se flux rate significantly influences the crystal growth of CIGS. It was also observed that the hole concentration of the CIGS film increased and resistivity decreased with increasing Se

flux. The higher SMR was found to be preferable in order to obtain better material properties to enhance the CIGS solar cell performance.

CHAPTER 5

CHARACTERIZATION OF ULTRA-THIN CIGS DEPOSITION USING SPECTROSCOPIC ELLIPSOMETRY

5.1 Introduction and motivation

In order to achieve high efficiency ultrathin CIGS solar cells, the key materials characteristics that must be controlled are the band gap profile, the phase purity and Cu stoichiometry, and the grain size. Since the band gap of CIGS can be tuned from 1.02 to 1.65 eV by increasing the atomic ratio x = Ga/(In+Ga) from 0 to 1, band gap engineering via variations in the deposition process has become one of the key parameters for high efficiency ultrathin CIGS solar cells [33]. As explained in the previous chapter, ultrathin CIGS films for high performance solar cells can be grown at high temperature by a 1-stage, 2-stage and 3-stage process. During 1-stage co-evaporation process, the deposited CIGS film is always Cu-poor whereas in the 2-stage and 3-stage co-evaporation processes, the CIGS film becomes Cu-poor only at the end of the deposition. It has already been demonstrated that, in order to obtain high quality materials with large polycrystalline grains size, the thin film must transition through a Cu-rich growth stage consisting of mixed phases of CIGS and $Cu_{2-x}Se$ [67]. CIGS solar cells with CIGS absorber layer deposited by the 3-stage co-evaporation exhibit the highest small-area efficiency among several others low-cost thin film polycrystalline photovoltaic (PV) technologies. However, this deposition method requires greater efforts in process optimization, monitoring, and control, and significant challenges exist in scale-up of the process to large areas. In order to understand the overall growth mechanisms and hence optimize CIGS solar cell

performance, real time analysis of the variations in the structure and composition throughout each of the three stages of the CIGS deposition process is beneficial. Real time spectroscopic ellipsometry (RTSE) has been developed specifically for in-situ monitoring and potential control of each stage of CIGS deposition by three-stage co-evaporation process. The fundamental optical transitions for the CIGS films do not vary with Cu content; however, sub-band gap absorption appears for the Cu-rich films due to the occurrence of a semi-metallic phase. Because this absorption is also observed directly in the ellipsometric parameters (ψ, Δ), one can use the RTSE to control the Cu threshold in a CIGS device in real time, a capability essential for avoiding shunted devices.

In this chapter, we will look at ultra-thin CIGS films deposited by 3-stage process and focus on the RTSE study for all three process stages in order to monitor and control the CIGS deposition process. In addition, the focus will be specifically on the transitions from Cu-poor to Cu-rich CIGS near the end of the second stage, and the transitions from Cu-rich to Cu-poor CIGS near the end of the third stage, by directly monitoring changes in the ellipsometric parameters (ψ, Δ) obtained by RTSE.

5.2 Fundamentals of Spectroscopic Ellipsometry (SE)

5.2.1 Introduction of Spectroscopic Ellipsometry (SE)

Spectroscopic Ellipsometry has emerged as a non-destructive, non-invasive optical technique for the characterization of thin-film solar cell materials and devices [68-70]. Ellipsometry derives its name from the measurement of the output polarization ellipse which is generated after a beam of light with a known input polarization ellipse interacts specularly with the sample [71-72]. It measures a change in polarization as light reflects

or transmits from samples. Because it uses the polarization state as a probe rather than only the intensity of the photon itself, it is a very sensitive measurement technique and is capable of unmatched ability to measure thin film materials. The change in polarization is represented as an amplitude ratio (Ψ) and the phase difference (Δ) between light waves known as p- and s-polarized light waves. (Ψ, Δ) spectra are measured by changing wavelength of light in spectroscopic ellipsometry. It generates information about thin films that are thinner than the wavelength of the probing light itself, and theoretically down to a single atomic layer [69]. Ellipsometers have been designed to collect spectroscopic data, from the near infrared (NIR) to the deep ultraviolet (DUV) wavelengths, in time periods short enough to track sub monolayer changes in materials systems in-situ during dynamic processes. This approach is commonly referred to as real time spectroscopic ellipsometry (RTSE).

The main key feature of ellipsometry is that it measures the change in polarized light upon light reflection on a sample (or light transmission by a sample). For the measurement, p and s- polarized light waves are directed onto a sample at Brewster angle and the optical constants and film thickness of the sample is measured from the change in the polarization state by light reflection or transmission after measuring the two values (Ψ, Δ) [73].

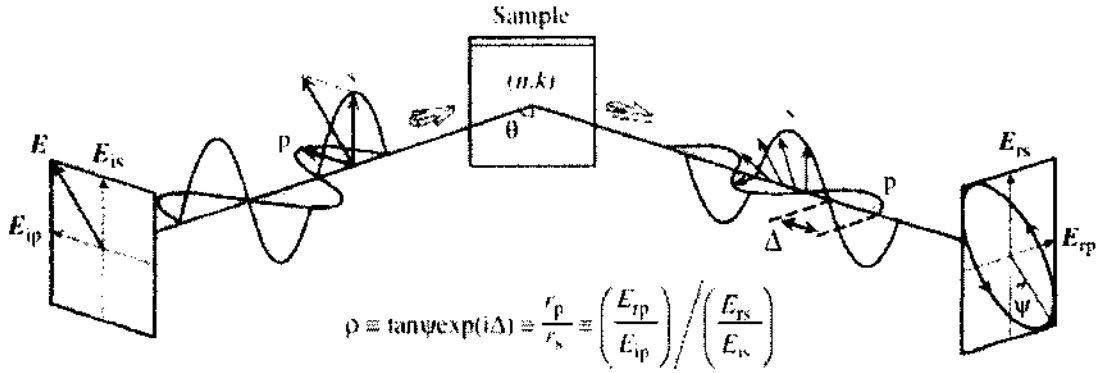

Figure 5.1 Measurement principle of ellipsometry [73]

5.2.2 Interaction of Light with Matter

Light is an electromagnetic wave that is described by Maxwell's equations for electromagnetic fields. In isotropic, homogeneous, and non-magnetic media, one solution of Maxwell's equations for the electric field is the electromagnetic plane wave given by [74]:

$$\vec{E}(\vec{r}, t) = \vec{E}_0 \exp\left[i\left(\frac{\vec{q}.\vec{r}}{c} - \omega t\right)\right] \tag{5.1}$$

where ω is the angular frequency of the wave, $\vec{q}$ is the complex wave vector along the propagation direction, and $\vec{E}_0$ is the complex electric field vector perpendicular to $\vec{q}$, which defines the amplitude and polarization state of the wave. The complex wave vector $\vec{q}$ is defined as:

$$q^2 = \left(\frac{\omega}{c}\right)^2\left[\varepsilon_r + i\left(\frac{4\pi\sigma}{\omega}\right)\right] \tag{5.2}$$

In equation 5.2, the right hand side term can be equated to the complex index of refraction N by:

$$N^2 = \left[\varepsilon_r + i\left(\frac{4\pi\sigma}{\omega}\right)\right] \tag{5.3}$$

where the complex index of refraction, N in Equation 5.3 is defined by N ≡ n + ik. Thus equation 5.1 can be rewritten as [75]:

$$\vec{E}(\vec{r},t) = \vec{E}_0 \exp\left[-\omega\frac{\vec{k}.\vec{r}}{c}\right]\exp i\left[\omega\frac{\vec{n}.\vec{r}}{c} - \omega t\right] \tag{5.4}$$

In equation 5.4, the exponential factor containing k outlines the amount of photons absorbed in the material as light propagates through it and k is called the extinction coefficient. The term which describes the photons absorption is called the absorption coefficient (α). The relation between α and k is given by:

$$\alpha = \frac{2\omega k}{c} = \frac{4\pi k}{\lambda} \tag{5.5}$$

In equation 5.4, the second exponential factor term represents the traveling wave with phase velocity c/n, where c is the velocity of light in vacuum and n is the refractive index of the material. The right hand side of equation 5.3 is the complex dielectric function (ε). The complex dielectric function, ε, is also used to define the optical properties of a material, similarly to N. Equation 5.3 in terms of n and k yields:

$$(n + ik)^2 = (n^2 - k^2) + i(2nk) = \varepsilon_1 + i\left(\frac{4\pi\sigma}{\omega}\right) = \varepsilon_1 + i\varepsilon_2 \tag{5.6}$$

where the term $\frac{4\pi\sigma}{\omega}$ is the imaginary part of the dielectric function (ε_2). By equating real and imaginary parts separately gives the relationship between the real refractive index, the absorption coefficient, and the real and imaginary parts of the dielectric function:

$$\varepsilon_1 = n^2 - k^2 \tag{5.7}$$

$$\varepsilon_2 = 2nk \tag{5.8}$$

$$n = \left[\frac{1}{2}\left\{\left(\varepsilon_1^2 + \varepsilon_2^2\right)^{1/2} + \varepsilon_1\right\}\right]^{1/2} \tag{5.9}$$

$$k = \left[\frac{1}{2}\left\{\left(\varepsilon_1^2 + \varepsilon_2^2\right)^{1/2} - \varepsilon_1\right\}\right]^{1/2} \tag{5.10}$$

If the complex wave vector, $\vec{q}$, is along the z axis then the complex electric field vector $\vec{E}_0$ of equation 5.1 can be expressed as:

$$\vec{E}_0 = E_{0x}\exp(i\delta_x)\hat{x} + E_{0y}\exp(i\delta_y)\hat{y} \tag{5.11}$$

where δ_x, δ_y represents the absolute phase of E_x, E_y at z = 0 and t = 0 respectively. In order to describe the state of polarization, only the phase different $\delta_x - \delta_y$ (or $\delta_y - \delta_x$) is required but not the absolute values of the initial phases. Figure 5.2 shows the various phase differences and the corresponding polarization states. In ellipsometry experiments, a coordinate system based on the plane of incidence of the obliquely reflecting light is used instead of using orthogonal x-y axis. In this coordinate system, the electric field is resolved into components parallel (p) and perpendicular (s) to the plane of incidence. These p and s components of the electric field of the reflected wave are connected to the p and s components of the incident wave through reflection coefficients, which are called the Fresnel coefficients [76-77].

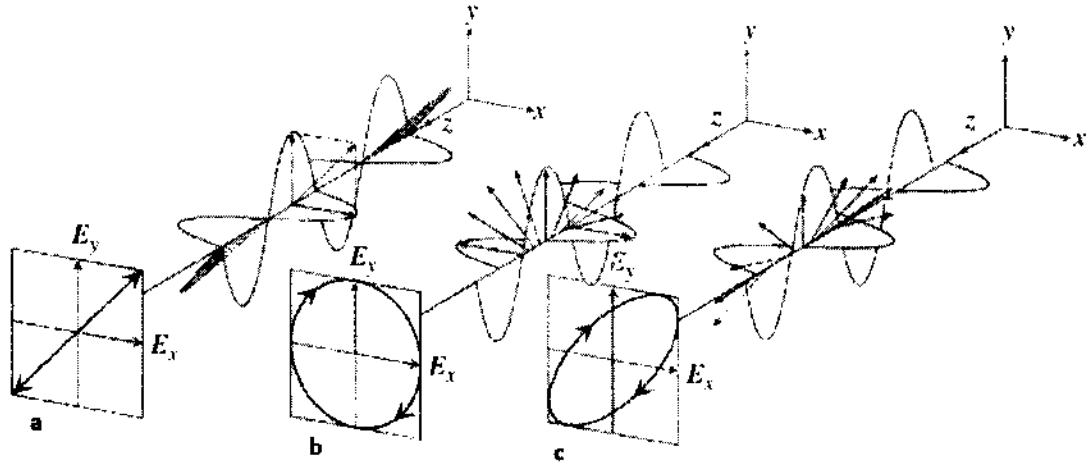

Figure 5.2 Representation of the variation of the polarization state with the phase difference a) δ_x- δ_y=0 represents the linearly polarized light and the orientation of the resultant vector of E_x and E_y is always oriented at 45^0 in the x-y plane, b) δ_x- δ_y=$\pi/2$ represents the circularly polarized light and the resultant vector of E_x and E_y rotates in the x-y plane as light propagates, c) δ_x- δ_y=$\pi/4$ represents the elliptically polarized light and the resultant vector rotates in the x-y plane. As shown in the figure, if the direction of rotation is clockwise for light traveling along the positive z axis, the polarization is called right circular/elliptical polarization. For each of the figure, E_x = E_y [73].

$$r_p = |r_p|\exp(i\delta_p) = \frac{E_p^r}{E_p^i} \tag{5.12}$$

$$r_s = |r_s|\exp(i\delta_s) = \frac{E_s^r}{E_s^i} \tag{5.13}$$

Here, "i" and "r" are used to indicate the incident wave and reflected wave respectively. The p-and s-polarizations undergo different changes both in amplitude and phase when the linearly polarized light is reflected from a surface. Ellipsometry always measures the amplitude ratio and phase difference between the p- and s-polarizations during the measurement. These two important quantities are represented by ψ and Δ, respectively. These two quantities, ψ and Δ are written as:

$$\rho_r \equiv \tan\psi \exp(i\Delta) = \frac{|r_p|}{|r_s|}\exp\left[i(\delta_p - \delta_s)\right] \tag{5.14}$$

where the angles ψ and Δ are defined as:

$$\tan\psi = \frac{|r_p|}{|r_s|} \tag{5.15}$$

$$\Delta = \delta_p - \delta_s \tag{5.16}$$

ψ is confined between 0 and 90^0 since ψ represents the angle determined from the absolute value of the amplitude ratio. In the meantime, Δ is the phase difference and hence it ranges from 0^0 to 360^0. When the sample structure is simple, ψ is characterized by the refractive index n and Δ by the extinction coefficient k.

5.2.3 Data Collection and Analysis

The main tools to collect the ellipsometry data include the following: light source, polarization generator, sample, polarization analyzer, and detector. Polarizers, compensators and phase modulators are the optical components used to manipulate the polarization. Common ellipsometer configurations include rotating analyzer (RAE), rotating polarizer (RPE), rotating compensator (RCE) and phase modulator (PME). A light source produces unpolarized light, which is then sent through a polarizer to generate the linearly polarized beam of light over a desired spectral range. These linearly polarized photons then pass through a rotating compensator, which shifts the relative phase of orthogonal vector components resolved along the fast and slow axes of the compensator. This in turn yields a phase shift between the p and s components of the electric field vector incident on the compensator. This phase shift depends on the angle of the fast axis of the compensator with respect to the plane of incidence. The beam of light then reflects from the sample surface, thus inducing a change in the nature of the polarization state modulation. Upon specular reflection, the beams then pass through a polarizer which

functions as the analyzer and then are collected by the spectrograph. Within the spectrograph, a beam splitter directs the low energy photons to an InGaAs photodiode array and the high energy photons to a CCD detector. The detector converts light to electronic signal to determine the reflected polarization. This information is compared to the known input polarization to determine the polarization change caused by the sample reflection. This is the data collection in terms of Psi (ψ) and Delta (Δ).

Ellipsometry does not directly provide information about the specimen; however, ψ and Δ are functions of the material properties such as thickness and dielectric function. Analyses of these (ψ, Δ) pairs are required to extract these characteristics. A simple schematic of the analysis procedure for data taken by real time spectroscopic ellipsometry is shown in Figure 5.3. In ellipsometry, developing an appropriate optical model for the sample is the starting point for the data analysis. When the component materials of the sample structure and their dielectric functions are known, the first step in building an optical model is by placing the right sequence of different layers, including each layer's thickness and optical properties as shown in Figure 5.4. If the dielectric functions of the composite material are not known then different dielectric function models should be used. There are many dielectric function models for ellipsometry analysis. For dielectric function modeling in a transparent region, the Cauchy or Sellmeier model is used. When there is free-carrier absorption, the Drude model is used. To express the electric polarization in the visible/UV region, various models such as Lorentz model, Tauc-Lorentz model, Critical-Point Parabolic-Band oscillators (CPPB), harmonic oscillator approximation (HOA) and model dielectric function (MDF) have been used [71]. Complexity can be added to the

model during the sample analysis, such as intermix layers and voids fraction, to improve the fitting and can be correlated with other theoretical and experimental techniques.

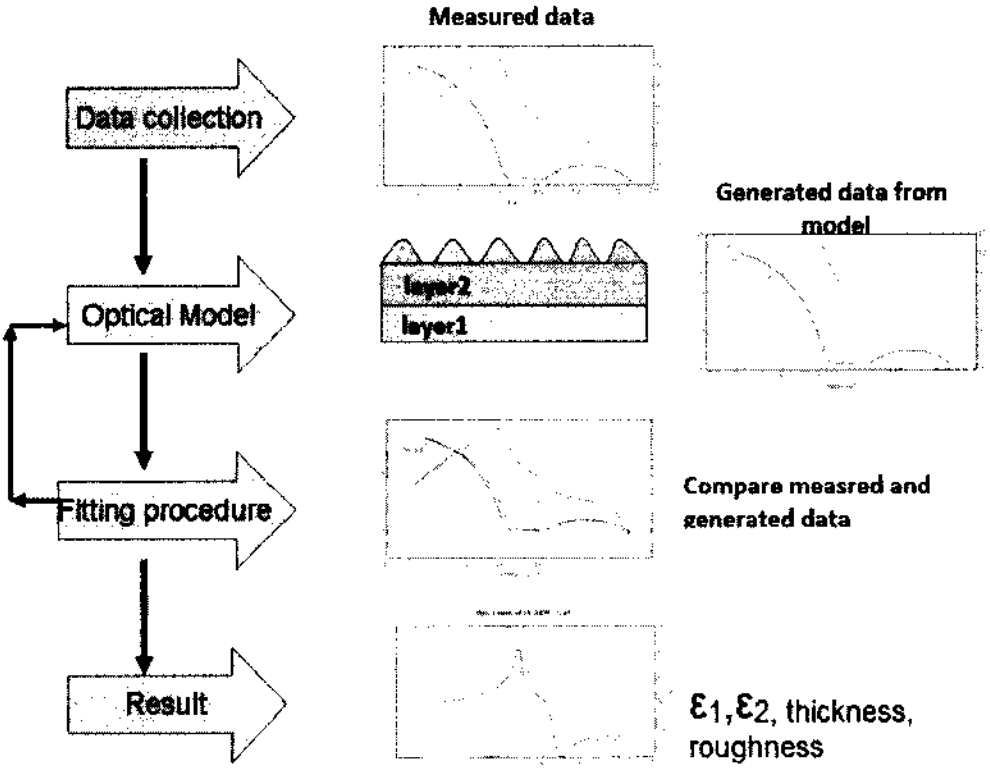

Figure 5.3 Simplified algorithm for data analysis from data acquired during RTSE measurement

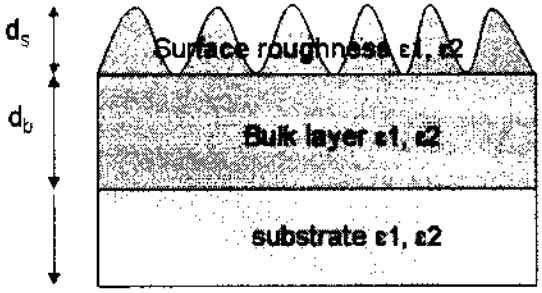

Figure 5.4 A simple optical model for a sample [30].

After developing the optical model, (ψ, Δ) are generated by assigning "first guess" values to the various energy–independent unknown parameters such as bulk layer

thickness, surface roughness. These generated (ψ, Δ) are then fitted to the experimental data. A least square regression algorithm i.e. numerical algorithm is used to minimize the differences between the generated spectra and the experimental data by adjusting the variable parameters in the model. Similarly to any numerical fitting procedure, a figure of merit is used to accept the fitted data from a set of many fitted data. One of the two choices used as a figure of merit for ellipsometry data analysis is called unbiased estimator or the mean square error (MSE), which is written as:

$$MSE = \sqrt{\frac{1}{2N-M}\sum_{i=1}^{N}\left[\left(\frac{\psi_i^{mod}-\psi_i^{exp}}{\sigma_{\psi,i}^{exp}}\right)^2+\left(\frac{\Delta_i^{mod}-\Delta_i^{exp}}{\sigma_{\Delta,i}^{exp}}\right)^2\right]} \qquad (5.17)$$

where N is the number of (ψ, Δ) pairs, M is the variable parameters in the model and σ is the standard deviation of the experimental data. The fitting process is stopped whenever MSE is minimized. This process of finding the lowest MSE is called least square regression.

If the dielectric function is unknown, the different dielectric function modeling can be used to extract the dielectric function of unknown material. A complete modeling of the dielectric function over a wide wavelength range is sometimes tedious due to the complex nature of the layers. In order to mitigate such complexity, the data analysis can be performed within a short range of wavelength, where the dielectric function is calculated with a reasonable fitting in that range for a specific value of the thickness. Now, this thickness is fixed and the measured (ψ, Δ) of the layer is then converted into optical functions. As an example, consider the optical model of thin film on semi-infinite substrate as "air(N_{air})/film(N_{film})/Substrate(N_s) ". The measured (ψ, Δ) are defined as:

$$\tan\psi \exp(i\Delta) = \rho(N_{air}, N_{film}, N_{substrate}, d, \theta) \qquad (5.18)$$

where N_i represents the complex refractive index of i^{th} layer (i.e. if i^{th} layer is air, N_i becomes N_{air}), d is thickness of the film and θ is the incidence angle in air/film interface. Let's assume that N_{air}, N_s, and θ are known and the N_{film} along with d is unknown. If the dielectric function of the film is expressed by Cauchy model parameters within a short range of wavelength and a good fitting is obtained by using specific ds, then N_{film} will be the only unknown parameter within the full range of measured energy. Now if equation 5.18 is solved, the measured (ψ, Δ) will be converted into N_{film} by solving the equation 5.18 [71]. This type of procedure is called mathematical inversion.

Ex-situ SE measurements can be performed at multiple angles of incidence and the resulting spectra can be analyzed together. During the data acquisition at multiple angles, the number of unknown parameters is the same but the number of measured quantities is 1412 (706 values of ψ, 706 values of Δ) multiplied by the number of angles of incidence. In this case, the total number of measured quantities is larger than the total number of unknown parameters to be determined and so more easily modeled by using the least square regression analysis. During the RTSE measurement, the angle of incidence is fixed and this approach is not readily applicable; a least square regression is therefore combined with mathematical inversion. If the bulk layer is being deposited on an already fully characterized substrate, then RTSE analysis can be performed during the growth even if the dielectric function is unknown. To extract the dielectric function and analyze the growth of any bulk layer, an optical model similar to Figure 5.4 with a bulk layer and a surface roughness layer made up of 50% bulk layer (film) / 50% Void can be used. At any particular time of deposition, the thickness of the growing film can be estimated from the growth rate and so the dielectric functions (ε_1, ε_2) can be obtained by mathematical

inversion trial, as shown in Figure 5.5. Using these trial dielectric functions as a reference for the growing film, a least square regression analysis can now provide a good estimation of the thickness. This method enables therefore one to determine the dielectric functions and the structure of the sample simultaneously [30].

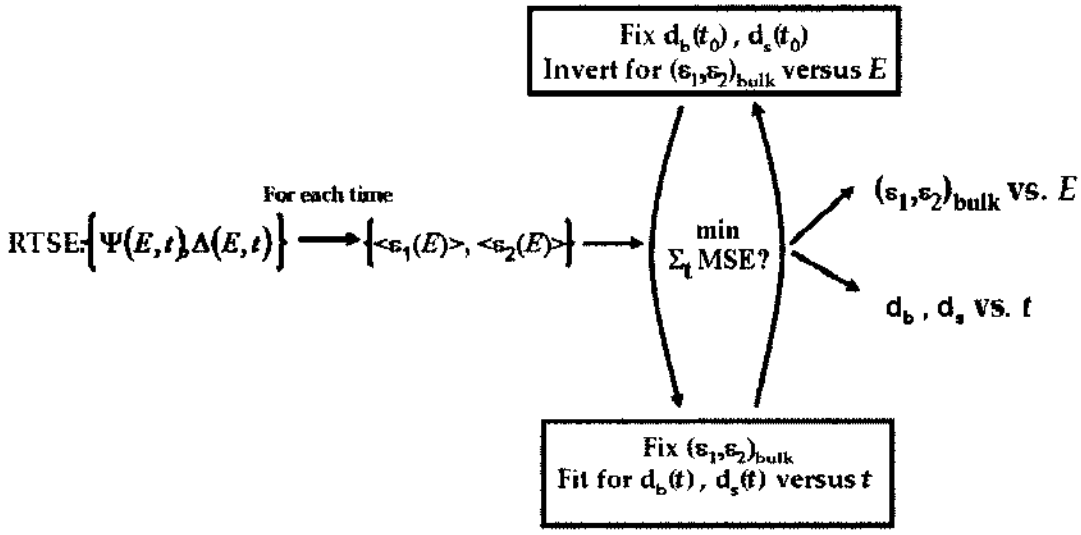

Figure 5.5 RTSE data analysis algorithm [30].

5.3 RTSE Studies of Ultrathin CIGS Films Deposited by 3-stage Co-evaporation Processes

The optical technique of real-time spectroscopic ellipsometry (RTSE) is becoming popular as the interest in developing and optimizing thin-film photovoltaic materials and devices grows. RTSE allows one to study the properties of thin film growth ranging from the initial nucleation and coalescence stage to the final film structural depth profile. Using a dielectric function database obtained from RTSE measurements, one can characterize completed solar devices ex-situ for relevant information such as component layer thicknesses and compositions. The precise control over deposition process is possible only

if the changes in the material properties during deposition process are monitored. There are different methods to monitor the deposition process in-situ. Most of these in-situ product monitor can fulfill the minimum requirement of monitoring the composition and thickness but to achieve higher efficiency, in-situ monitoring of electrical and optical properties are necessary. Once the optical properties of $Cu(In,Ga)Se_2$ (CIGS) as a function of the composition, temperature and other deposition conditions are known, RTSE can become one of the most suitable *in*-situ sensor to monitor the thickness, roughness, optical and electrical properties, and growth temperature. RTSE has also been used to study the effect of the copper content, a key compositional variable in CIGS PV technology, on the microstructural evolution and optical properties of CIGS thin films.

As we discussed in the previous chapter, 3-stage thermal co-evaporation process has proven to produce high quality CIGS materials for solar cells. This process provides a high level of flexibility but also generates greater challenges in the process optimization, monitoring and control [17]. Available methods to control the three stage CIGS process involve measuring elemental fluxes using electron impact emission spectroscopy (EIES) and observing the emissivity using IR sensor (pyrometer) or indirectly using the heater power required to maintain the constant substrate temperature [17]. Due to the limitation of these existing process monitoring and control capabilities, which limits the real-time correction of process fluctuations from the targeted final layer composition, the industry has adopted readily controllable CIGS deposition process compared with multisource co-evaporation process [78-79]. In general, the potential device efficiency is traded for the process stability, even though improved control of 3-stage CIGS process is sought so that high quality materials can be fabricated for industrial-scale process. In 3-stage CIGS

deposition, three sequent deposition processes proceed to get the final CIGS film. A first stage is the deposition of In, Ga and Se at relatively low substrate temperature (~400 °C). The second stage includes deposition of Cu and Se at high substrate temperature (~550 °C). During this stage, the film composition changes from $(In_{1-x}Ga_x)_2Se_3$ to the Cu-rich $Cu(In,Ga)Se_2$ composition through the stoichiometric $Cu(In,Ga)Se_2$ composition. When the CIGS film becomes Cu-rich, a semi-liquid $Cu_{2-x}Se$ phase is believed to form on the bulk layer which consists of mixed phases of $Cu(In,Ga)Se_2$ and $Cu_{2-x}Se$. Due to the presence of a semi-liquid $Cu_{2-x}Se$ phase, a large grain growth is known to occur [38]. At the third stage, the Cu-rich CIGS film is transformed into a Cu-poor film by the deposition of In, Ga and Se. Fabricating the high quality CIGS for photovoltaic application depends on manipulating the CIGS stoichiometric composition during the segregation of $Cu_{2-x}Se$. In order to control the stoichiometric composition of CIGS, several methods are developed such as monitoring the substrate temperature under constant substrate heater power by a thermocouple [80], monitoring IR emissivity of a $Cu_{2-x}Se$ surface layer formed at the end of stage [81] and a spectroscopic light scattering method [82]. Unfortunately, these commonly used methods for monitoring the presence of this phase are based on the observing changes on the emissivity of the film and lack quantitative capabilities. Spectroscopic ellipsometry is a very interesting method because it measures the complex dielectric function based on the state of the light polarization of the reflected light. The measurements of the ellipsometric parameters (ψ, Δ) during the deposition processes based on the change of the dielectric function are useful to control the process [83]. The second stage and third stage of three stage CIGS deposition method are very interesting since the film changes from Cu-rich transition to Cu-poor transition during the deposition process.

It is expected that the dielectric function changes according to the respective phases which enables to study the phase and the stoichiometric composition by means of the in-situ, real time spectroscopic ellipsometry (RTSE) measurements.

Detailed studies were performed to describe (i) the use of RTSE for analysis of $(In_{1-x}Ga_x)_2Se_3$ (IGS) formation during stage I of the deposition process, (ii) the conversion of IGS into CIGS during stage II and the rapid development of bulk $Cu_{2-x}Se$ during the end of stage II and (iii) Cu-rich to Cu-poor CIGS thin film transition during stage III in order to maintain the stoichiometric composition of the final CIGS thin film.

5.3.1 Experimental Details

Figure 5.6 shows the schematic of the experimental setup used in this study for co-evaporation of CIGS with optical monitoring by RTSE. A multichannel ellipsometer based on a single rotating compensator (model M2000-DI, J. A. Woollam Company, Lincoln, NE) was used to collect ellipsometric spectra in situ, during processing in ~3-s intervals. The angle of incidence was 70° with respect to the normal to the sample surface. The start of the first stage (I) involves co-evaporation of In, Ga, and Se at a substrate temperature of 400 °C. Films were deposited having compositional values of x = 0 (In_2Se_3), 0.25, 0.31, 0.45, 0.56, 0.69, and 1 (Ga_2Se_3), as measured by energy-dispersive x-ray spectroscopy (EDS). The results are given in Table 1. For the stoichiometry $(In_{1-x}Ga_x)_2Se_3$, the Se composition should be x = 0.6. The lower values in some cases may be attributed to either an excess of the group III elements or additional $(In_{1-x}Ga_x)Se$ phases. After an IGS precursor film of intended thickness (~ 65% of the desired final absorber layer thickness) is deposited, the In and Ga source shutter were closed to stop In and Ga co-evaporation.

The substrate temperature is then increased to 550°C and stage II is started. In this stage, Cu and Se are evaporated till the Cu-poor to Cu-rich transitions occurred. At the beginning of stage III, the In, Ga and Se sources are evaporated at the same rate as in the first stage. At the end of stage III, as defined by the Cu-rich to Cu-poor transition, the In and Ga sources were closed to terminate co-evaporation and the substrate temperature was steadily decreased.

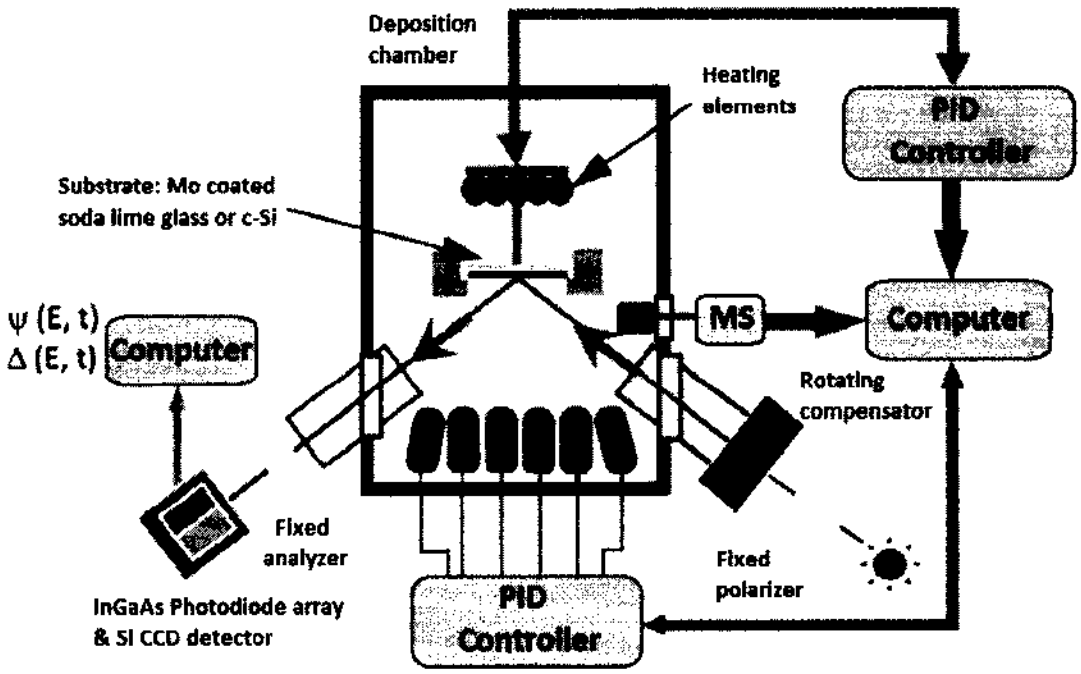

Figure 5.6. Schematic diagram of experimental setup for the deposition of CIGS thin-film materials with optical monitoring by RTSE.

Table 5.1: Chemical compositions obtained from EDS for the IGS layers deposited in this study. For the stoichiometry $(In_{1-x}Ga_x)_2Se_3$, the Se composition should be x = 0.6.

In (%)	Ga (%)	Se (%)	Ga/(In+Ga) (x)
41.7	----	58.3	0.00
33.8	11.2	55.0	0.25
28.9	13.1	58.0	0.31
25.3	20.4	54.3	0.45
18.5	23.8	57.7	0.56
12.3	27.5	60.2	0.69
----	41.2	58.8	1.00

5.3.2 RTSE of the First Stage

About 65% of the final CIGS absorber layer thickness is generated in the first deposition stage that yields $(In_{1-x}Ga_x)_2Se_3$ (IGS). Thus, it is critical to study this stage and ensure the desired initial composition (x=Ga/In+Ga) and, thus, its ultimate profile throughout the absorber layer after all three stages, are complete. In order to study this stage and develop a dielectric function database for future characterization of IGS materials - in real time, in situ and ex situ - films were deposited having compositions x = 0.00 (In_2Se_3), 0.25, 0.31, 0.45, 0.56, 0.69, and 1.00 (Ga_2Se_3). All depositions were performed at the first-stage substrate temperature of 400°C. The RTSE data for the growing IGS samples were analyzed using the three layers model shown in Figure 5.7. The layers consist of (i) a Mo/IGS interface roughness layer, having a fixed thickness assumed equal to the roughness

layer thickness determined for the Mo surface, (ii) an IGS bulk layer of thickness d_b, and (iii) an IGS surface roughness layer of thickness d_s, the latter two determined individually at each time point in the analysis. Considering (i) and (iii), the Bruggeman effective medium approximation (EMA) was applied to extract the real and imaginary parts of the complex dielectric function for the roughness layers, given by $\varepsilon = \varepsilon_1 + i\varepsilon_2$. A multi-time analysis approach was used in this study to generate a smooth ε for IGS using B-spline functions. These dielectric functions were then parameterized using critical point (CP) and Tauc-Lorentz (TL) oscillators representing the band gap and the higher energy regions, respectively. This parameterization provides information that can be interpreted in terms of compositional variations and grain size. The resulting dielectric functions are shown in Figure 5.8. The change in behavior of these dielectric functions at $x \sim 0.45$ is consistent with a well-defined hexagonal crystal structure for $x \leq 0.45$ and a disordered structure for $x > 0.5$.

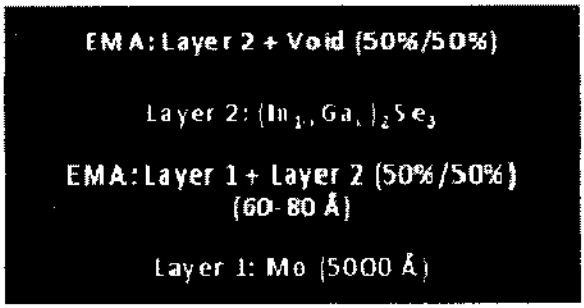

Figure 5.7 Multilayer model used for the analysis of RTSE data acquired on IGS thin films prepared in the first stage of CIGS co-evaporation.

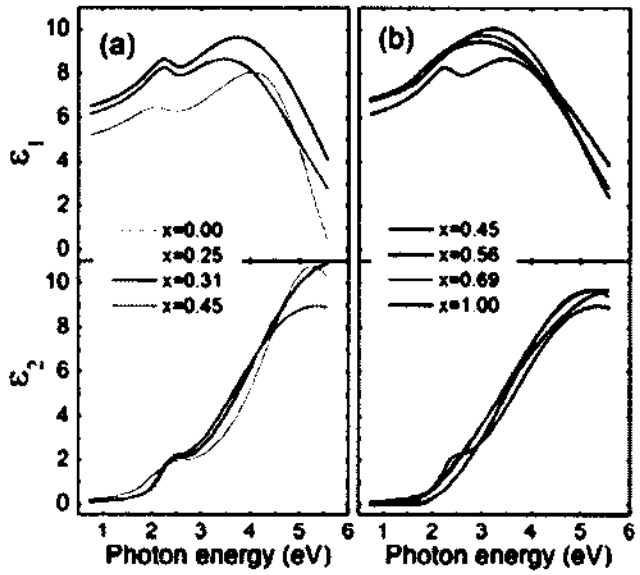

Figure 5.8 Parameterized dielectric functions of IGS films measured at 400°C for (a) $x \leq 0.45$ and (b) $x \geq 0.45$. The dielectric function model includes a critical point oscillator near the fundamental band gap and a Tauc-Lorentz oscillator with a resonance at high-energy.

Figure 5.9 shows the evolution of stage I IGS with x = 0.31 obtained by RTSE. The ~ 50 vol.% voids of the ~ 76 Å thick roughness layer on the underlying Mo are filled in by IGS, leading to a rapid increase in the IGS vol.% in the layer from t = 0. Simultaneously, the surface roughness thickness d_s on the IGS increases from $d_s = 0$ as the Mo is covered by IGS. After the interface composition is stabilized, a bulk layer can be incorporated into the model. During initial bulk layer growth, the roughness thickness on the IGS decreases indicating suppression of substrate-induced roughness and apparent wetting of the Mo surface. Later, the IGS roughness increases due to enlarging crystallites protruding above the surface. In addition to the film's structural evolution, its dielectric function can be obtained as a compositional fingerprint.

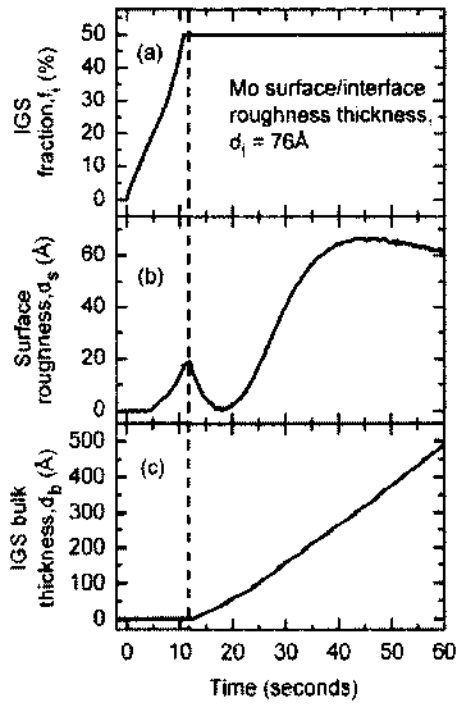

Figure 5.9 Early stage structural evolution of IGS with x = 0.31 on Mo-coated soda-lime glass. (a) IGS vol.% filling the voids (assumed 50 vol% at t= 0) in the Mo surface roughness layer (b) IGS surface roughness thickness, and (c) IGS bulk layer thickness.

The intermediate stage surface roughness evolution, i.e. over the range from 1000 to 2000 Å, is presented in Fig. 5.10(a) for selected samples. The results for all samples including the later stage of growth are shown in Fig. 5.10(b). The latter figure shows different behaviors for alloyed films with x ~ 0.2-0.4 and those with lower and higher x. In fact, the films with x = 0.25 and 0.31 are the only ones that show continued roughening throughout the growth process, all other films show stabilized or smoothening surfaces at the end of deposition. For x = 0.25 and 0.31, continuous roughening suggests continuous crystallite growth which generates growing protrusions at the surface, whereas for lower and higher x, smoothening effects are observed, ultimately (in the limit of thick IGS) yielding flatter surfaces characteristic of the stabilization of a finer grained structure. Figure 5.11 shows the monotonic trend in roughness layer thickness at the end of deposition --

near the bulk layer thickness of 9000 Å. The surface roughness thickness shows a rapid decrease when the x value increases above x ~ 0.31, which is likely to suggest a rapid reduction in the grain size, leading to smaller, stable protrusions above the surface.

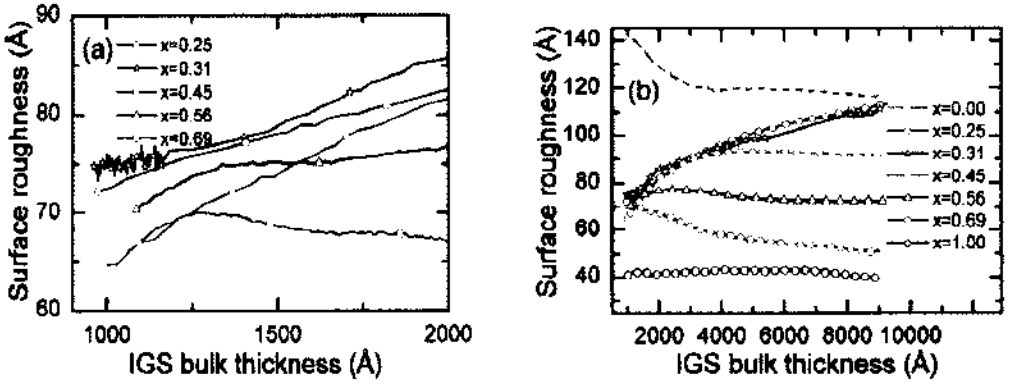

Figure 5.10 (a) Surface roughness evolution for IGS films of selected Ga composition x over the bulk layer thickness range of 1000 - 2000 Å; (b) expansion of the results of (a) to the full sample set and a wider bulk layer thickness range.

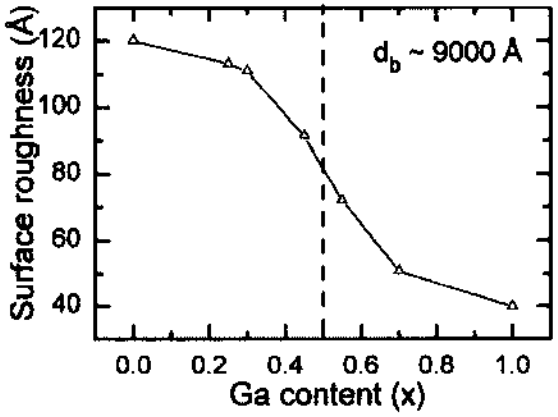

Figure 5.11: Variation of surface roughness with Ga content x at the bulk layer thickness (d_b) of ~ 9000 Å.

Figure 5.12 shows the variations of the band gap, amplitude, and broadening of the bandgap critical point oscillator versus alloy composition. The In- and Ga- rich sides of IGS have different properties as reflected in the Figure. For x < 0.5, the band gap critical

point is clearly visible at E = 2.15 - 2.35 eV in (ε_1, ε_2) and sharpens with increasing x up to x = 0.3. In contrast, for x > 0.5, the amplitude of this critical point drops to low values, indicating a suppression of the fundamental band gap structure. In its place, a very broad low energy absorption tail is observed that can be simulated with the onset of the Tauc-Lorentz oscillator.

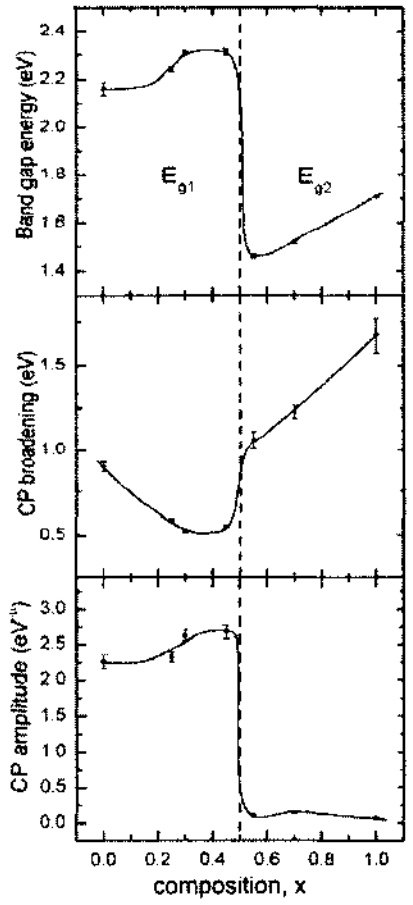

Figure 5.12: Variation of the (top) critical point resonance energy Eg_1 (x < 0.5) or Tauc-Lorentz band gap Eg_2 (x > 0.5), (center) critical point resonance broadening Γ_1 and (bottom) critical point resonance amplitude A_1 as functions of x.

Scanning electron micrographs of the same set of IGS films as was measured by RTSE are shown in Figure 5.13. These reveal trends that support the structural and optical behavior from RTSE. First, a strong reduction in grain size is observed between x=0.31

and x=0.54, which is consistent with the reduction in surface roughness in Figures 5.11 and 5.12. In addition, the finer grain structure of x = 0 relative to x = 0.31 is reflected in the stabilization of the roughness in Fig. 5.10(b) for x = 0, as compared to a continuous roughening effect consistent with continuing growth of large grains for x = 0.31.

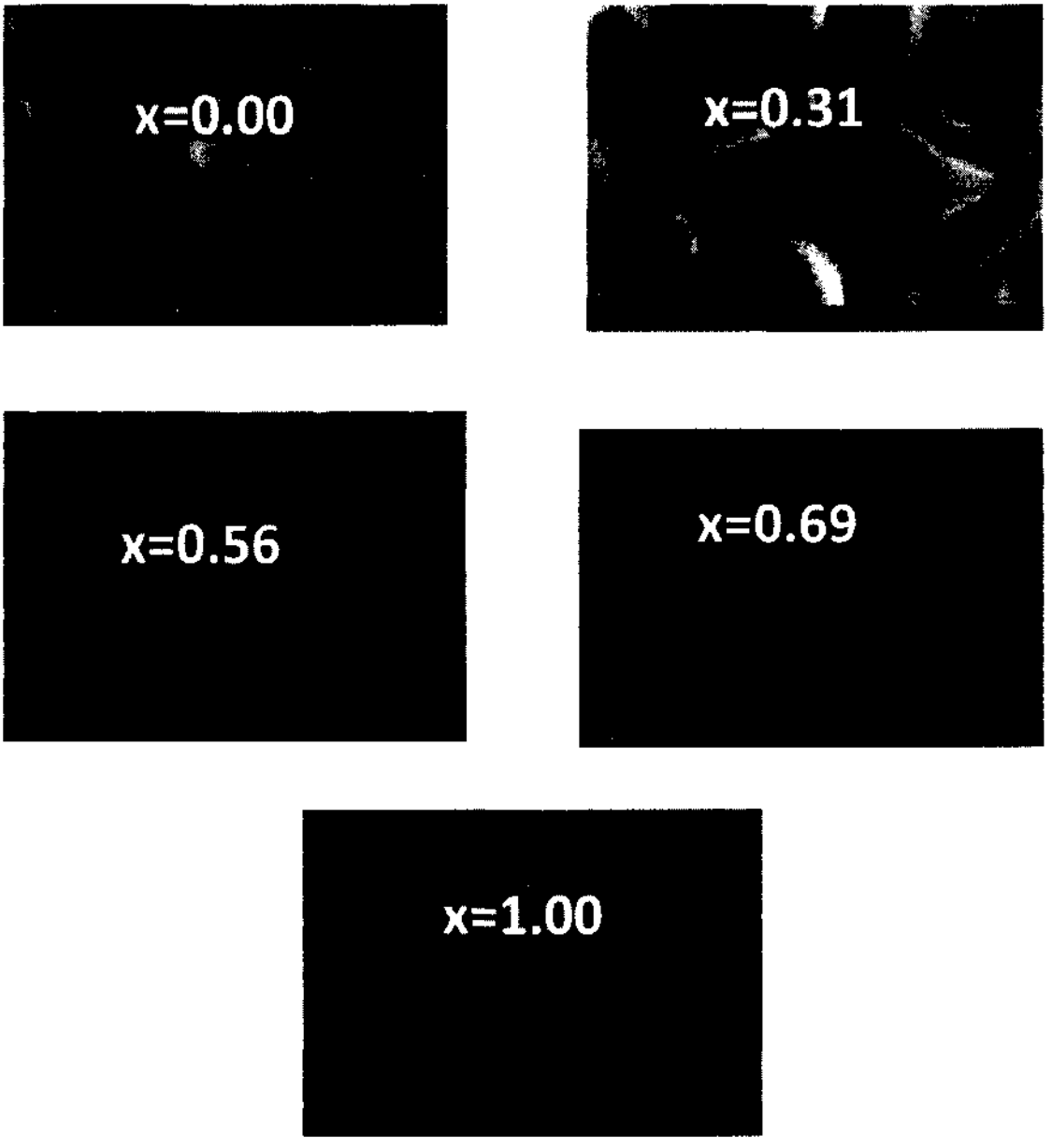

Figure 5.13: Scanning electron micrographs for IGS films of different alloy compositions which were also measured by RTSE.

5.3.3 RTSE of the Second Stage

In this initial analysis of stage II RTSE data, a bulk conversion model, in which the entire IGS layer is converted into CIGS uniformly throughout its thickness via an increase in CIGS volume fraction at the expense of IGS was used (Figure 5.14). In the bulk conversion model, CIGS nucleates uniformly with depth within the bulk IGS layer, and the grain size and the concentration of grains increase with time at the expense of the surrounding IGS material until the entire IGS layer is consumed. In this process, the bulk layer thickness increases as the Cu is incorporated. Thus, it is assumed that IGS, CIGS and $Cu_{2-x}Se$ components of the bulk layer are resolvable at any time during Cu exposure, and as a result the film is modeled with a uniform bulk layer according to a three-component Bruggeman EMA.

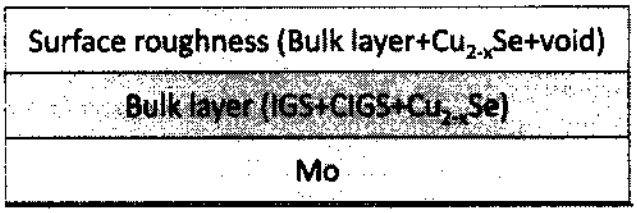

Figure 5.14: Bulk conversion model for the analysis of stage II RTSE data

Fig. 5.15(a) shows bulk thickness evolution at the end of stage I and throughout stage II, obtained on the basis of the bulk conversion model. The plot shows that there is a rapid increase in IGS thickness during stage I. The growth stops due to the cool down of In and Se sources at the beginning of stage II. When the evaporation of Cu starts, the bulk thickness starts to grow again due to the conversion of IGS into CIGS. In the bulk

conversion model, the process starts as small inclusions of CIGS in IGS and the volume fraction of CIGS then increases with time until all the IGS material is converted into CIGS. A plot of CIGS content vs. time is shown in Fig. 5.16 (b). The initial analysis of stage II shows the presence of some $Cu_{2-x}Se$ even during the Cu poor part of stage II. Figure 5.16 shows a plot of $Cu_{2-x}Se$ content vs. time derived from the bulk conversion model. The rapid increase in $Cu_{2-x}Se$ content towards the end is due to the Cu-poor to Cu-rich transition, and shows that our analysis yields the correct result.

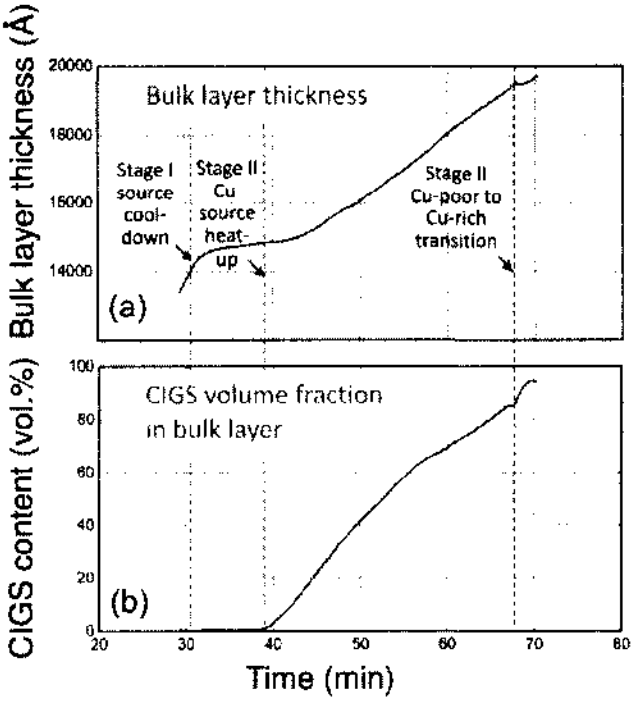

Fig 5.15: Evolution of (a) bulk thickness and (b) CIGS volume % during stage II obtained on the basis of the bulk conversion model

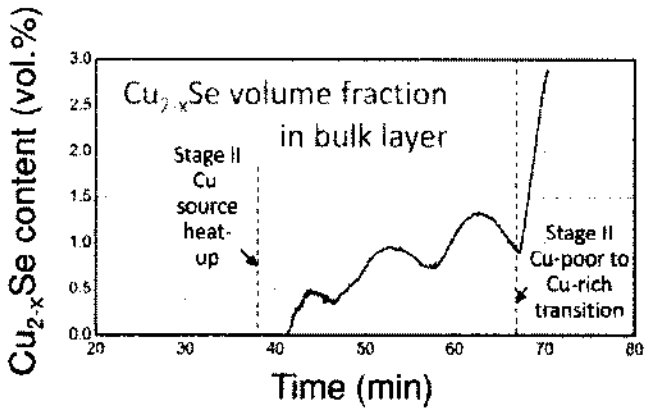

Figure 5.16: A plot of $Cu_{2-x}Se$ content in vol. % within the bulk layer vs. time based on the bulk conversion model.

5.3.4 RTSE of the Third Stage

During the third stage, Cu-rich CIGS film is transformed into a Cu-poor film by the deposition of In, Ga and Se, to provide a suitable absorber layer for the CIGS solar cell. An optical model of two surface layers consisting of CIGS surface roughness (consisting of crystallites protruding above the surface), as well as an underlying layer consisting of $Cu_{2-x}Se$, CIGS, and voids was used to monitor the Cu-rich to Cu-poor transition. Figure 5.17 shows RTSE analysis results for a CIGS film near the end of stage III, along with an optical model that provides quantification of the effective thickness of the Cu_{2-x} Se phase, which is present near the surface when the film is Cu-rich. With this model, the Cu-rich to Cu-poor transition can be identified as the time at which the $Cu_{2-x}Se$ volume fraction (also its effective thickness) decreases to zero. Termination of the deposition can then be determined by the additional effective thickness of $(In_{1-x}Ga_x)_2Se_3$ deposition forming after the complete elimination of the $Cu_{2-x}Se$ phase. For this 0.7 μm film, the addition of an extra ~ 200 Å of $(In_{1-x}Ga_x)_2Se_3$ starting from the transition is estimated to lead to a Cu stoichiometry decreasing from 0.25 to ~0.22, as desired. Thus, the RTSE capability not

only provides an indication of the Cu-rich to Cu-poor transition, but it also enables one to identify and control the thickness increase after this transition in order to achieve the desired Cu-poor stoichiometry.

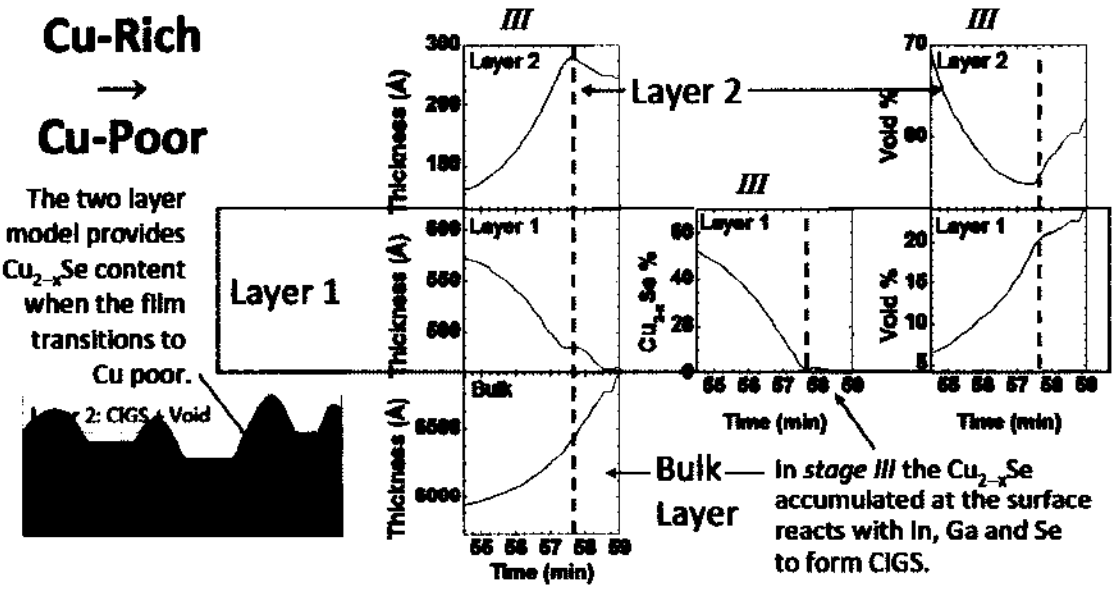

Figure 5.17: Optical model for real time analysis of the third stage of three stage CIGS deposition. Two surface layers describe the roughness as well as the Cu-rich phase at the surface of the film. The thicknesses of these two layers along with the bulk thickness, and the layer volume fractions are given in the three panels at the right.

5.4 Summary

Ultrathin CIGS films were deposited using a 3-stage process and detailed study was performed to describe (i) the use of RTSE for analysis of IGS during stage I of the deposition process; (ii) the conversion of IGS into CIGS during stage II and the rapid development of bulk $Cu_{2-x}Se$ during the end of stage II; and (iii) Cu-rich to Cu-poor CIGS thin film transition during stage III in order to maintain the stoichiometric composition of the final CIGS thin film. For x = 0, the initial roughness is very large but smoothening

occurs via coalescence. In contrast, for x = 1, the initial surface is quite smooth and stable with time. Only for x ~ 0.25-0.3, does the roughness increase throughout deposition, indicating continuous growth of grains that protrude above the surface. A significant change in roughness evolution is observed for x > 0.5 as the final surface roughness thickness decreases rapidly with x. RTSE enables therefore analysis of the structural evolution, grain growth processes, dielectric functions during CIGS fabrication. It also enables tracking of the IGS-to-CIGS conversion and the transitions between Cu-poor and Cu-rich films during CIGS growth. The RTSE method also proves to be a potentially important tool for end-point detection in each of the three stages of the CIGS growth.

CHAPTER 6

ADVANCES IN CIGS FABRICATION PROCESS

6.1 Introduction

Impurities in the CIGS absorber layer can have a strong influence on the performance of the CIGS solar cell [84-85]. Impurities can be introduced unintentionally in many ways into the CIGS layer: using impure source material, impure liners for the deposition sources, and other non-appropriate supporting parts for the evaporation sources. Most of the impurities in the absorber layer degrade the cell performance by introducing recombination centers. We therefore paid specific attentions to all the materials used in our chamber to enhance the solar cells efficiency.

The CIGS absorber layer is a compound made of Cu, In, Ga, and Se. In order to obtain high conversion efficiency CIGS solar cell, the compositional depth profile of each element in the CIGS absorber layer must be well-controlled. An in situ process monitor is therefore a very important tool that allows producing repeatable, high-quality CIGS coatings. The process monitor for a CIGS co-evaporation system should meet the following critical requirements: 1) The process monitor must work both in situ and in real time; 2) The process monitor must be operated at high temperatures (the surrounding temperature range from 350 °C to 550 °C); and 3) The process monitor must be able to sustain Se corrosion during evaporation. A novel non-contact method based on detection of infrared (IR) emission by I-R sensor (pyrometer) has several advantages over the well-established contact thermocouple method and over other optical methods, and was implemented in our chamber.

6.2 Modification of the co-evaporation system

The evaporation equipment that has been used for co-evaporation of the CIGS absorber is shown in Figure 6.1. The deposition chamber is evacuated to the lower part of the high vacuum regime, 10^{-7} torr, by using a Pfeiffer turbo molecular pump, backed by an Edwards dry scroll pump. The system consists of 6 individual sources. The system is equipped with several individual crystal monitors to monitor the rate of individual source during the deposition. The substrate heater is a stainless steel box equipped with halogen lamps for IR heating. Between the evaporation sources and the substrate there is a substrate shutter. When the substrate shutter is closed it prevents the flux of all metal vapors to reach the substrate. Initially, the distance between the individual source and the substrate was very high (~ 30 inches). During the deposition process, it consumed a lot of source materials such as copper (Cu), indium (In), gallium (Ga) and selenium (Se), which wasted a lot of product during each deposition process. The system was then modified by raising each source in order to reduce the distance between the individual source and the substrate. After this modification, the consumption of each source was reduced significantly and led to better quality films as the rates were more constant over time.

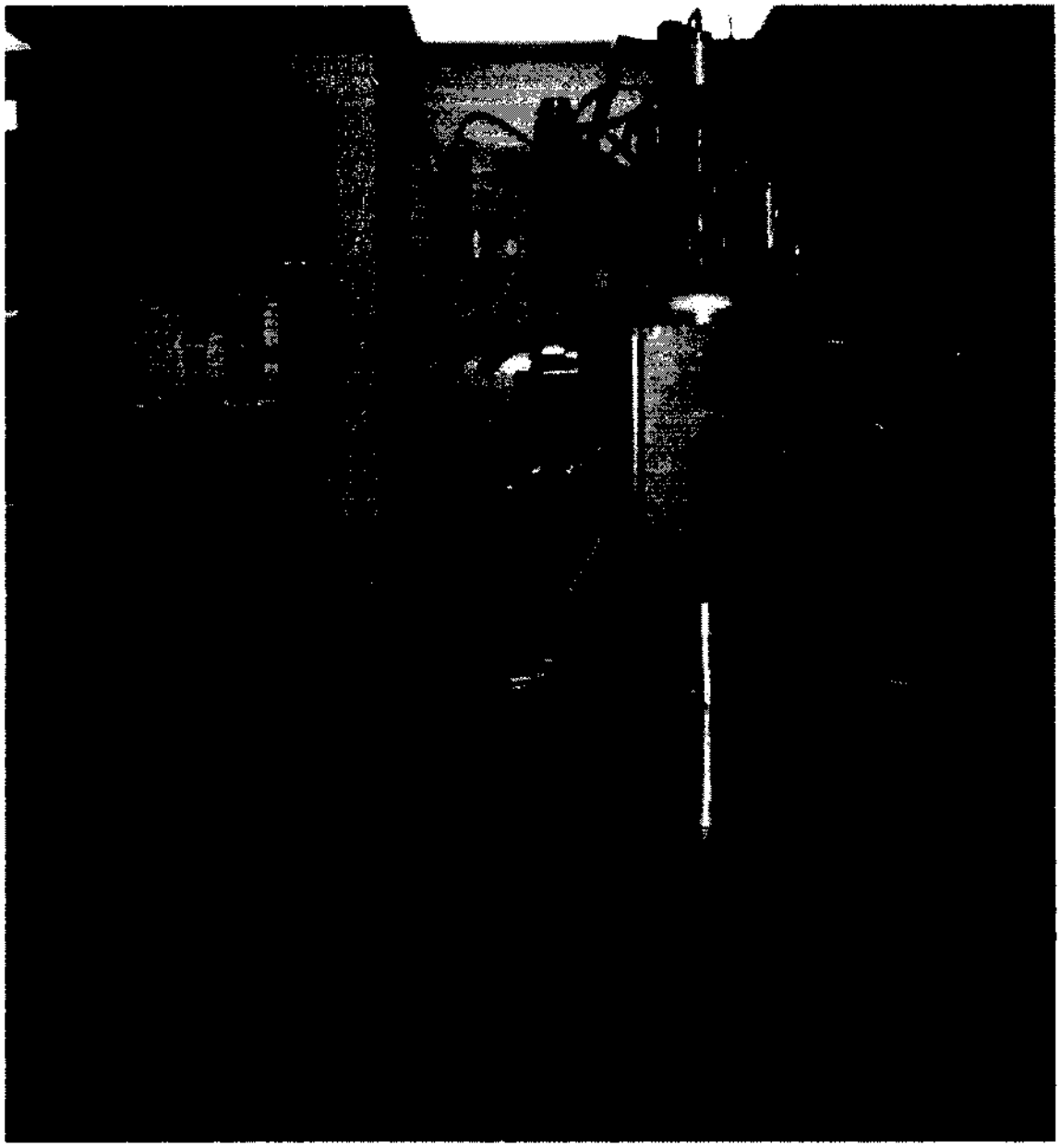

Figure 6.1 Front view of the co-evaporation chamber, with the controller unit for the system on the left.

6.3 I-R sensor for end point detection

As we discussed earlier, co-evaporation of CIGS via 2-stage and 3-stage processes has been used to fabricate small-area devices with efficiencies greater than 20 % [5]. Control of the Cu/(In+Ga) ratio throughout film growth constitutes one of the most critical aspects during the co-evaporation process. A slightly Cu-rich growth period has been found to increase grain size and device quality [86]. The relative impact of the Cu-rich growth period is a function of deposition time and temperature, which can directly impact throughput and cost in manufacturing [86]. In addition, the final Cu/(In+Ga) ratio should also be within acceptable range, which is generally between 0.80 and 0.95 [87].

Currently available flux sensors are not suitable to control the Cu/III ratio within an acceptable degree since the requirements for flux control during CIGS co-evaporation are rigorous. The sensor should be able to distinguish between simultaneous rates of different species, and to operate reproducibly in a high-temperature environment with significant Se pressure. Even though a wide variety of methods for rate control have been utilized, including electron impact emission spectroscopy (EIES) [88], atomic absorption spectroscopy [89], effusion source temperature control [89] and mass spectroscopy [90], none of these tools is sufficient to independently control the Cu ratio within the desired accuracy.

On the other hand, the increase in emissivity which occurs when the CIGS transitions into a Cu-rich regime [91-92] has been utilized as an endpoint indicator, successfully showing precise control of the Cu/III ratio. Such emissivity increase can be detected as a drop in the substrate temperature measured by contact thermocouple [93] or as an increase in heater power required to keep the substrate at a constant temperature [94].

The contact thermocouple method of sensing the Cu-rich transition is problematic from a manufacturing perspective for several reasons. First the thermal contact between thermocouples and the substrate is unreliable for continuous processing of moving substrate. Furthermore, the expected temperature change may be only a fraction of a degree Celsius depending on system thermal and control parameters. Finally, this method cannot be used for flexible substrate that allow low-cost, roll-to-roll processing due to low thermal mass and inability to sustain the mechanical pressure of a thermocouple. So non-contact, optical methods of probing the growing CIGS thin film emissivity have become of increasing interest. Such methods include in situ measurement of reflected [95], transmitted [92] and emitted light [96]. Each of these optical techniques shows some advantages. Measurements of specularly reflected light produce a large signal, but require precise sample-to-optics alignment in each deposition period. Transmitted light measurements offer a very high sensitivity, which is very good for low-emissivity films, but require deposition of the film onto a transparent substrate. Emission measurements are appealing, since no light source is required which simplifying the sensor apparatus.

A novel non-contact method based on detection of infrared (IR) emission by I-R sensor (pyrometer) has several advantages over the well-established contact thermocouple method and over other optical methods. Compared with the thermocouple method, it is more applicable to moving and lightweight substrates.

We installed such a pyrometer in our chamber. We used it as a guide for maximum and final Cu/III ratio, as a large signal change occurs at the Cu-poor to Cu-rich transition, as well as at the Cu-rich to Cu-poor transition. Figure 6.2 shows the typical growth plot depicting the development of the substrate temperature as measured by pyrometer (T_{pyro})

with respect to deposition time. During the first stage, only In, Ga and Se were deposited at approximately 400 °C, forming a $(In,Ga)_2Se_3$ (IGS) precursor film. At the beginning of the second stage, the substrate temperature was ramped up slowly to around 555 °C, the PID temperature controller was cut out and a constant heating power was supplied. Only Cu and Se were deposited and the overall cation ratio [Cu]/[In+Ga] of the growing CIGS film was continuously increasing. At the process point, $t_{stio,1}$, the temperature of the substrate drops, which is an indication of the surface segregation of $Cu_{2-x}Se$. The $Cu_{2-x}Se$ phase has a higher emissivity towards the IR region than the Cu-poor CIGS and the increased emission of heat radiation leads to a lower substrate temperature [93]. The relative incorporation rate of Cu and (In+Ga), rr_{inc} is deduced after assuming that (i) the growth rate or incorporation rate of In, Ga and Se into the thin film are constant during the process and (ii) the substrate temperature drop corresponds to the overall stoichiometric composition [Cu]/[In+Ga] = 1, giving:

$$rr_{inc} = \frac{r_{inc}(Cu)}{r_{inc}(In)+r_{inc}(Ga)} = \frac{t_{stoi,1}}{t_1} \qquad (6.1)$$

where t_1 is the duration of first stage.

After $t_{stio,1}$, the entire film composition becomes more and more Cu-rich, leading to a [Cu]/[In+Ga] ≈1.1 at the end of stage 2. The purpose of this high ratio is that the Cu-rich film is beneficial for the film morphological and electronics properties [85]. The presence of $Cu_{2-x}Se$ in the Cu-rich film would help in the better intermixing of Ga and In due to their high diffusivity and also provide extra nucleation and growth site for CIGS [97]. Then, $Cu_{2-x}Se$ provides the transportation medium for these grains towards the solid liquid interface which help in the growth of larger CIGS grains normal to the substrate [98]. In stage 3, only In, Ga and Se evaporate until the target composition [Cu]/[In + Ga]

~ 0.9 is reached. During this stage, at $t_{stio.2.}$ the stoichiometry is passed starting from Cu-rich to Cu-poor side as the indication of the increase in the substrate temperature. Thus I-R sensor has been used to track the transitions between the Cu- rich and Cu-poor surfaces during CIGS deposition process in order to obtain high quality CIGS absorber layer.

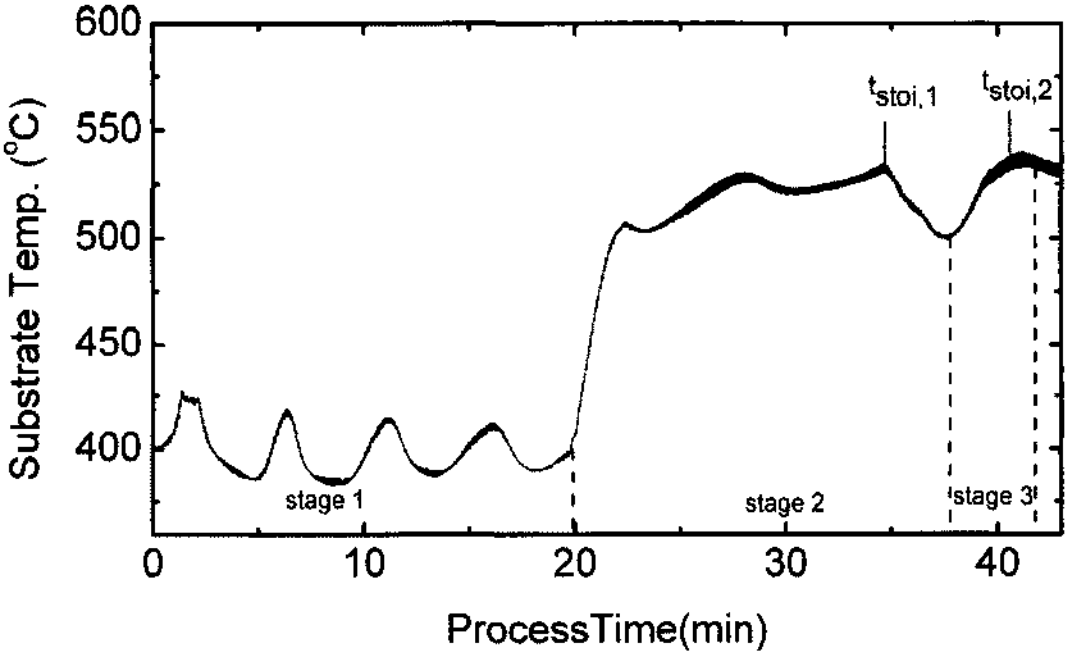

Figure 6.2 Typical substrate temperature profiles, T_{pyro} during the three-stage-growth of $Cu(In,Ga)Se_2$

6.4 Advances in CIGS solar cell fabrication

6.4.1 CIGS solar cell structure

CIGS cell structure as shown in Figure 6.3 consists of the following layers: n-ZnO:Al as a window layer, i-ZnO, CdS as a buffer layer, p-CIGS as a absorber, Mo as the metal contact and glass as the substrate. A molybdenum layer deposited by magnetron sputtering serves as the back contact and reflects most unabsorbed light back into the absorber. Following molybdenum deposition a p-type CIGS absorber layer is grown by co-evaporation process. The co-evaporation process is the most successful technique used to fabricate high efficiency CIGS solar cell. This deposition process involves simultaneous evaporation of individual elements from multiple sources in a single or sequential process. A thin cadmium sulfide (CdS) deposited by chemical bath deposition (CBD) is added on top of the absorber. CdS thin films (~ 50 nm) deposited by CBD process yield the most efficient Cu(In,Ga)Se2 thin film based devices since this process is conformal for very thin films. This process also helps in cleaning the CIGS layer and in intermixing the Cd by chemically driven ion-exchange mechanism [99-100]. However, there is the loss of current in the solar cell due to the absorption in the CdS layer at and below ~520 nm. So CdS thickness optimization is very crucial in CIGS solar cell. A thin, intrinsic zinc oxide layer (i-ZnO) and aluminum-doped zinc oxide (AZO) are deposited on top of the CdS. The i-ZnO layer is used to protect the CdS and the absorber layer from sputtering damage while depositing the ZnO:Al window layer. The AZO serves as a transparent conducting oxide to collect and move electrons out of the cell. It is therefore crucial to optimize each layer of the CIGS solar cell structure to produce the best performance CIGS solar cells. The optimization process for each layer is described below.

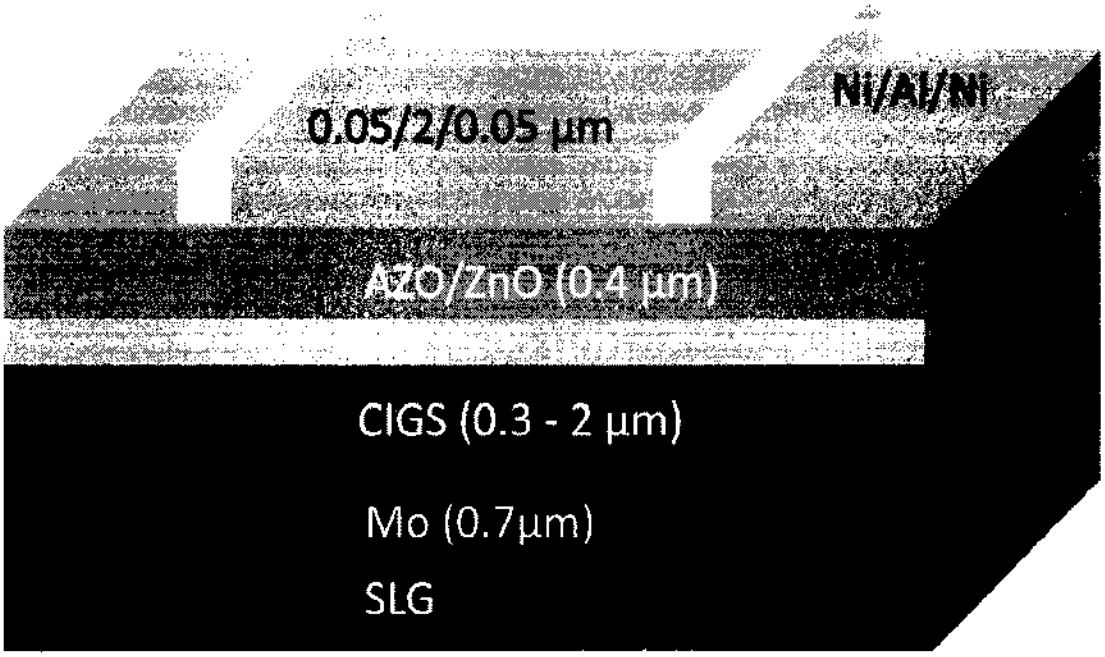

Figure 6.3: CIGS solar cell structure

6.4.2 Molybdenum back contact deposition

Molybdenum back contacts were deposited on soda lime glass (SLG) by DC magnetron sputtering with base pressure of ~ 2 x 10^{-6} Torr. Molybdenum targets with 2 inches diameter, ¼ inch thickness, and 99.95% purity were used. Uniform film thickness (±5% error) was achieved using a rotatable substrate holder. The argon pressure was varied between 3 and 16 mTorr while keeping a constant sputtering power of 150 W. The resistivity of the films was found to increase with increasing working pressure (Figure 6.4). At higher working pressure in the system, the kinetic energy of Mo ions is decreased due to the increased particle scattering. The deposited film tends then to be less dense with some porous column boundaries, and cannot be crystallized well. As a result, the resistivity of the film increases. The sputtering DC power was also optimized and it was found that the resistivity of Mo film was inversely proportional to the sputtering power. So, the

pressure and power during the deposition was kept at optimized value to obtain the better quality back contact Mo layer. However, in order to obtain an optimal Mo film, with a lower resistivity and good adhesion, a new process was needed and the Mo layer film was deposited using a sequentially changing working pressure. We observed, as had been previously reported [101], that films deposited at high pressure leaded to high resistivity while films deposited at low pressure leaded to poor adhesion. In order to ensure optimum properties for the Mo bilayer, the 1st layer was deposited at 10 mTorr (with a thickness ~100 nm), and the 2nd layer was deposited at 3 mTorr (with a thickness ~600 nm), which ensures good adhesion, low resistivity and high reflectance. The power used was 150 W. The thickness of the Mo layer was proportional to the sputtering time with an observed deposition rate of 7nm/min. The thickness for all depositions was kept constant at ~ 0.7 μm. Adhesive tape test was performed on each film by using scotch tape to determine the adhesion strength of the films.

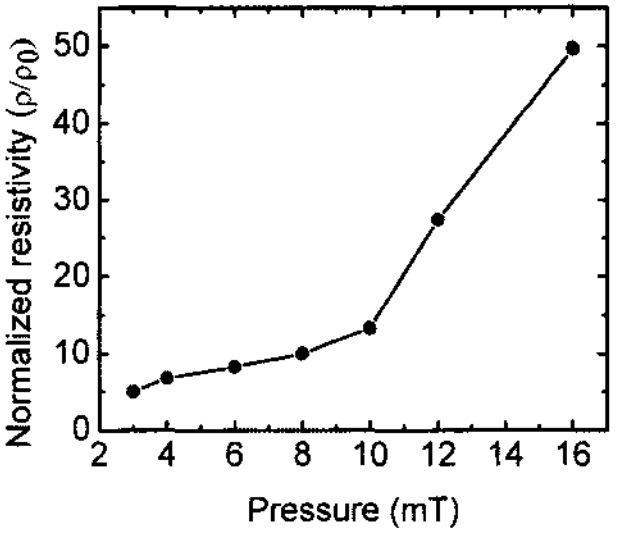

Figure 6.4 Normalized resistivity as a function of pressure for Mo thin film

6.4.3 CdS buffer layer deposition

Cadmium sulfide (CdS) was deposited by chemical bath deposition (CBD) process as a buffer layer and heterojunction partner for CIGS. The chemical used in the CBD process consists of Cadmium Acetate ($Cd(CH_3COO)_2$) as a Cadmium source, thiourea ($CS(NH_2)_2$) as a Sulphur source and Ammonium Hydroxide (NH_4OH) as a complexing agent. The deposition process consists of an external bath with a heater attached to it. Different recipes were implemented to optimize the CdS layer to achieve the best performance CIGS solar cells.

In the first recipe, 22 ml of 7.63 g/l aqueous solution of Cadmium Acetate was mixed with 17 ml of NH_4OH (30%); then, 22 ml of 77.85 g/l of aqueous solution of Thiourea was poured into the beaker containing 164 ml of water. The sample, which was first soaked in DI water for 5 minutes, was immerged into the water bath heated at 60^0C. Every minute, the samples were shaken up and down few times which help remove any precipitates on the surface. The PH of the solution was typically around 11. The deposition was continued for 9 minutes. After the deposition, samples were rinsed with DI water and dried in a nitrogen environment.

In the second recipe, 15 ml of 6.74 g/l aqueous solution of Cadmium Acetate and 35 ml of NH_4OH (28%) were first mixed into a beaker containing 185 ml of DI water. The beaker was then placed into the water bath. After 1 minute, 15 ml of 28.48 g/l aqueous solution of Thiourea was poured into the beaker. The deposition was started when the water bath was heated at 70°C. The sample was then dipped into the solution and the deposition was completed in 22 minutes. Every 2 minutes, the samples were shaken up and down few times which helped remove any precipitates on the surface. After the deposition, samples

are rinsed with DI water and dried in a nitrogen environment. The thickness of the CdS layer for both process was around 50 nm.

SIMS analysis (not shown here) on the finished CdS films showed considerable amounts of carbon, oxygen, nitrogen and hydrogen when we started the process. Extra precautions on the chemical purity and process were taken while performing CBD process to reduce the extra contamination in the films. For each CBD process, a fresh solution was prepared for individual chemical sources which enhanced the fabrication process.

6.4.4 Window layer deposition

The window layer in the CIGS solar cell structure contains two parts: a 100 nm thick intrinsic ZnO and a 350 nm thick 2% aluminum-doped ZnO. Both films were deposited by RF magnetron sputtering at 13.56 MHz with a base pressure of ~5 x 10^{-6} Torr. The power used for the deposition of i-ZnO and Al:ZnO targets were 60 W and 130 W, respectively. The substrate temperature was kept at room temperature, while the pressure was kept constant at 4 mTorr. Uniformity of the film thickness was achieved by using a rotatable substrate holder moving at a speed of ~20 rpm. The ambient humidity affected transparency and conductivity of the aluminum doped zinc oxide during deposition process, since the sputtering system does not have a load lock system. A strong dependence of the deposited layer properties on the ambient humidity was observed. As can be seen from the layer transmission curve (AZO at high humidity condition) presented in Figure 6.5, sputtering from the AZO target after a long exposure of the chamber in the high humidity day resulted in the deposition of resistive layers with low transparency. The conditions were improved by performing depositions after backing out the chamber for an

hour at 250 °C. Sputtering from the AZO target in low humidity condition (called dry environment) allows the layer transparency to be kept at a high level (85-90%) as shown in Figure 6.5 (AZO at low humidity condition) with a low sheet resistance of 30-35 Ω/sq. The detailed mechanism of electrical conductivity and transparency on these AZO layers is not clear yet and needs further investigation.

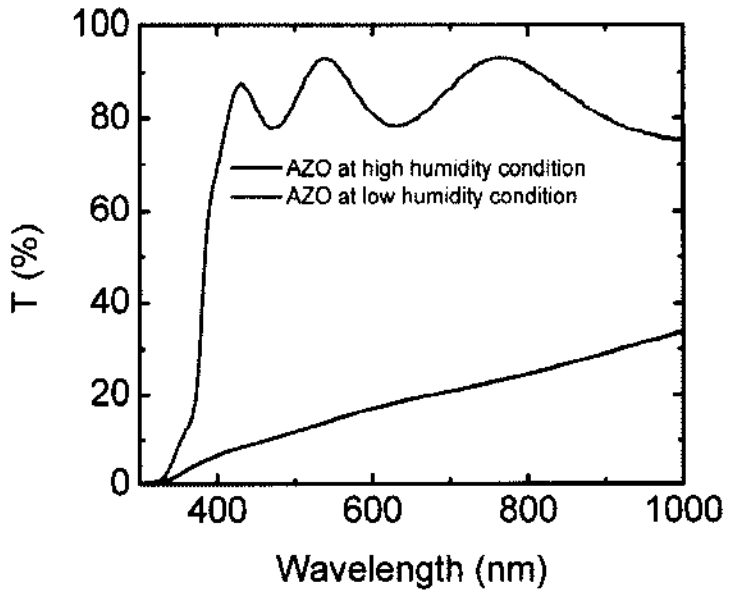

Figure 6.5 Transmission spectra of AZO layers deposited at very high and low humidity condition

6.4.5 Metal contact deposition

After the deposition of the window layers, metal grids were deposited on top of the AZO layer to facilitate the current collection and provide a contact pad for J–V characterization of the cells. The tapered finger grids in a 50/3000/50 nm thick Ni/Al/Ni sandwich were deposited by e-beam evaporation through a shadow mask and covered approximately 4% of the total cell area. The metal evaporation rate and film thickness were monitored with a quartz-crystal microbalance (QCM). The function of the two thin nickel layers is to protect the aluminum to react with oxygen from the front contact layer and from

air, respectively. The top nickel layer also facilitates an Ohmic contact between the grid and the I-V measuring probes. Figure 6.6 shows the CIGS complete cells with area 0.5 cm^2 defined by mechanical scribing.

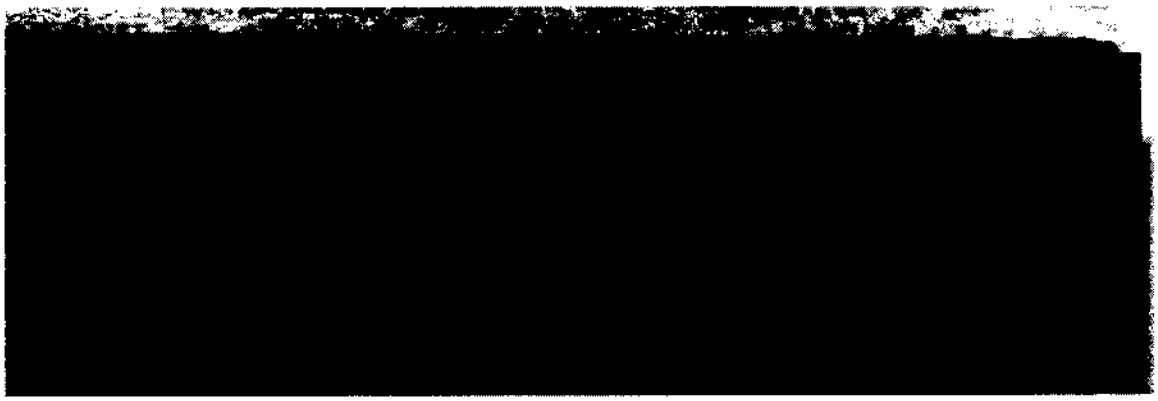

Figure 6.6 CIGS complete cells with area 0.5 cm^2 defined my mechanical scribing

6.4.6 Effect of impurities during the film growth on the performance of CIGS thin film solar cells

Impurities in the CIGS absorber layer can have strong influence on the performance of the CIGS solar cell [84]. Impurities can be introduced unintentionally in many ways into the CIGS layer as mentioned previously. Most of the impurities in the absorber layer degrade the cell performance by introducing recombination centers. Other impurities such as Sb and Bi were found to improve the performance of CIGS solar cells [102]. It is well known also that a small amount of alkaline material such as Na and K is required in the CIGS absorber layer to improve solar cell efficiency [103-104]. Despite the positive effects, it was also found that the presence of excess alkali elements during the growth process can lead to a deterioration of the solar cell performance [104]. It was also reported

for devices at high temperature (~600 °C) that the efficiency of the solar cell starts to decrease at high Na concentration [104]. In order to understand the electronic properties in CIGS solar cells, it is very useful to know the elemental distribution in the film with nanometer-scale resolution. Secondary Ion Mass Spectroscopy (SIMS) is capable of detecting elements with concentration as low as parts per billion (ppb) and is therefore an ideal tool for impurities analysis. In SIMS measurement, a primary ion impinges on the material and depending on the primary ion's charge, positively or negatively charged ions are ejected out of the material.

When we started fabricated solar cells, we observed that a maximum efficiency of 10% was achieved for solar cells grown by 3-stage process, with even lower efficiencies for the other processes. Based on the J-V and QE measurements, a thorough device analysis was done on each of these devices to understand the reason behind the inability to overcome the barrier of 10% efficiency. All these analysis were indicating that, even if 2 μm thick $Cu(In,Ga)Se_2$ was grown for each device, the actual active area was much thinner (~ 500 nm). Solar cells devices were therefore analyzed by SIMS in positive secondary mode and negative secondary mode to find if there was any type of impurities present in the device.

The positive SIMS spectra analysis on a CIGS thin film deposited by 3-stage co-evaporation process on a Si wafer confirmed the presence of impurities like oxygen, hydrocarbon, magnesium, potassium, and calcium as shown in Figure 6.7. The potential source of these impurities could be the liners which were used as evaporation containers for different sources and other supporting parts in the deposition chamber. It needs to be noted that most of the sources were heated above 1000°C during the deposition process.

These contaminations could be the potential sources for higher defects density in CIGS thin film, which we observed while simulating ultrathin CIGS devices as explained in chapter 3. Several parts were covered by high purity molybdenum sheet, which can easily withstand the high temperature outside the sources (~ 500-600 °C). The positive SIMS depth profile spectra of CIGS films deposited on c-Si wafer after covering the parts with molybdenum sheet did not contain any calcium, magnesium and other peaks as can be seen in Figure 6.8. Figure 6.9 shows the elemental depth profiles of the CIGS thin films deposited on the soda lime glass (SLG) after using high purity sources and covering the parts. There were no foreign impurities observed, which could cause defects in the CIGS thin film. Na and K are from the SLG at high temperature, which are generally beneficial for the cell [103]. We were able to fabricate the CIGS solar cell with efficiencies 17.1% after using these improvements.

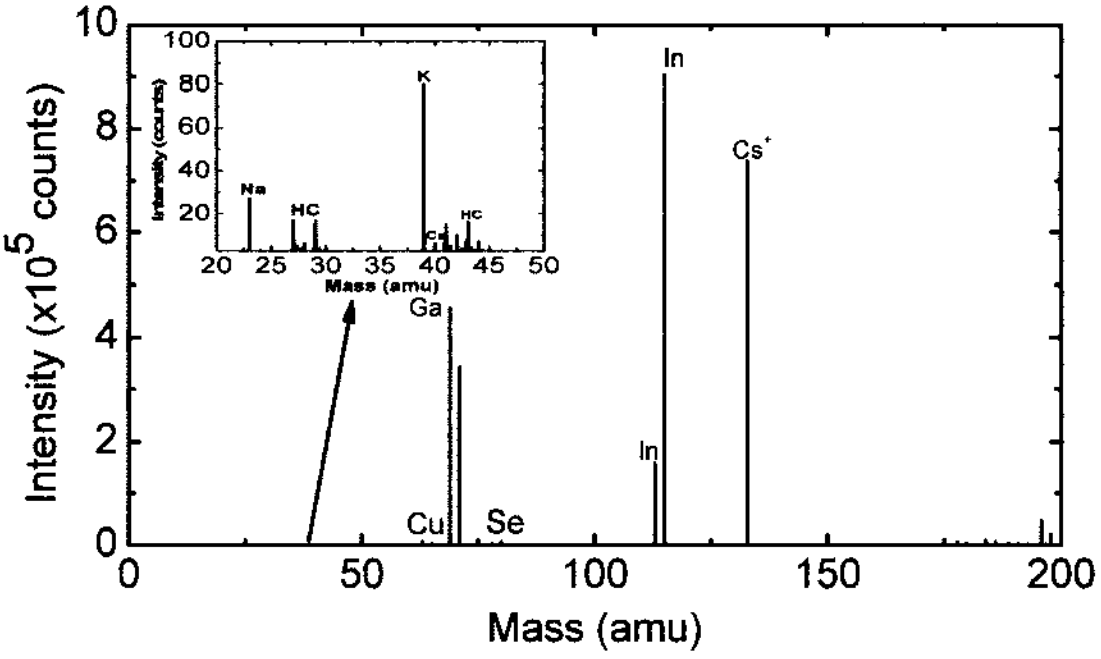

Figure 6.7 The positive ion SIMS spectra of CIGS thin film deposited on c-Si wafer before impurities removal

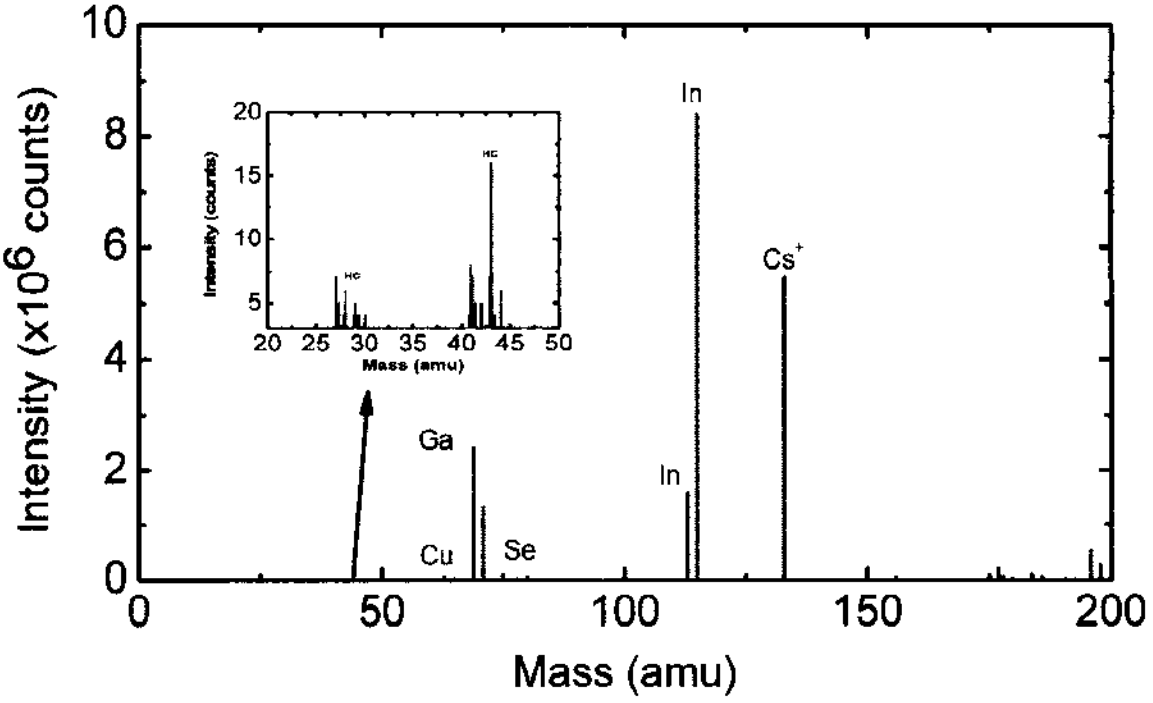

Figure 6.8 The positive ion SIMS spectra of CIGS thin film deposited on c-Si wafer after impurities removal

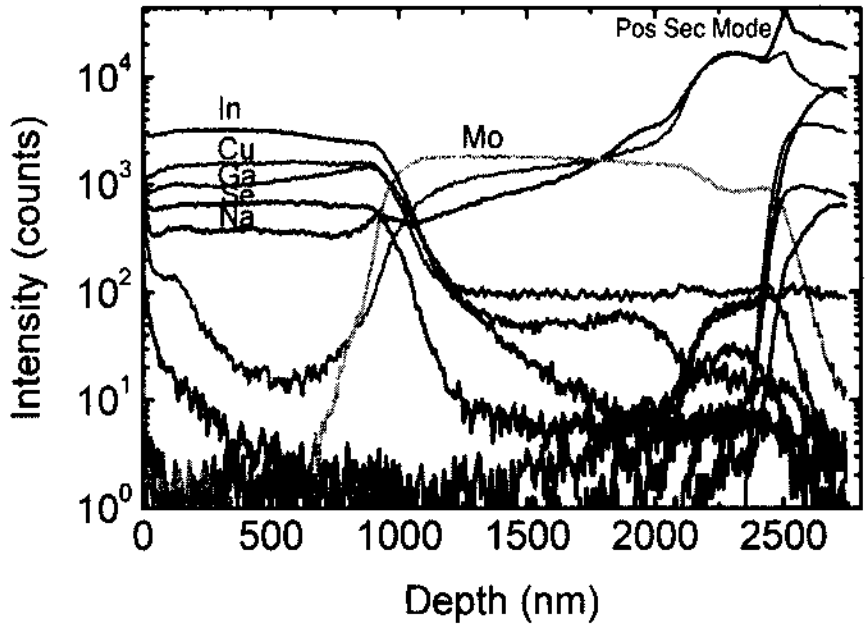

Figure 6.9 The SIMS depth profile in positive secondary mode of the $Cu(In,Ga)Se_2$ thin film deposited on soda lime glass (SLG)

6.4.7 Improved solar cell performance

As mentioned earlier, impurities in the CIGS absorber layer can have a strong influence on the performance of the CIGS solar cell [84]. Most of the impurities in the absorber layer degrade the cell performance by introducing recombination centers. After modification and enhancement of several of our processes, we were able to fabricate CIGS solar cells with efficiency as high as 17.1%.

Current density-voltage (J-V) measurements of the completed devices were performed under standard test conditions (AM 1.5 global spectrum at 25°C, 100 mW/cm^2). We observed uniform cell performance, with efficiencies greater than 16 % without MgF_2, on a 1 inch by 3 inches substrate incorporating 18 small area devices (0.50 cm^2). The best cell exhibited an efficiency of 17.1% after coating with MgF_2, with critical cell parameters as shown in Table 6.1. J-V curve for the best device with and without 100 nm of MgF_2 anti-reflecting coating is shown in Figure 6.10. Quantum efficiency (QE) measurements were also performed on the best cell with and without 100 nm of MgF_2 anti-reflecting coating (Figure 6.11). The calculation of the current from the QE curve by integrating the data over the entire spectrum leads to value identical to the ones obtained via the J-V curves and confirmed the proper calibration of our system and correct area of the cells. The QE onset in the near infrared (~1195 nm) is consistent with the energy band-gap obtained from the XRF, EPMA, XRD, and optical measurements. As can be seen in Figure 6.11 (b), the QE was improved after ARC coating due to the reduction of the reflection from the material interface. There was no significant absorption in the window layer (ZnO/AZO) region since the ZnO/AZO layers have high band-gap energy. Absorption in CdS is one of the major losses in this device. The loss in QE for $\lambda < 500$ nm is directly proportional to the thickness

of the CdS, since electron-hole pairs generated in the CdS are not collected in the device. This loss could be reduced by reducing the thickness of the CdS layer.

Table 6.1 Best solar cells fabricated from CIGS thin film deposited by 3-stage process

Processes	J_{sc} (mA/cm^2)	V_{oc} (V)	Fill Factor (%)	Efficiency (%)
3-stage	34.3	0.64	73.8	16.3
3-stage with ARC	35.6	0.65	73.9	17.1

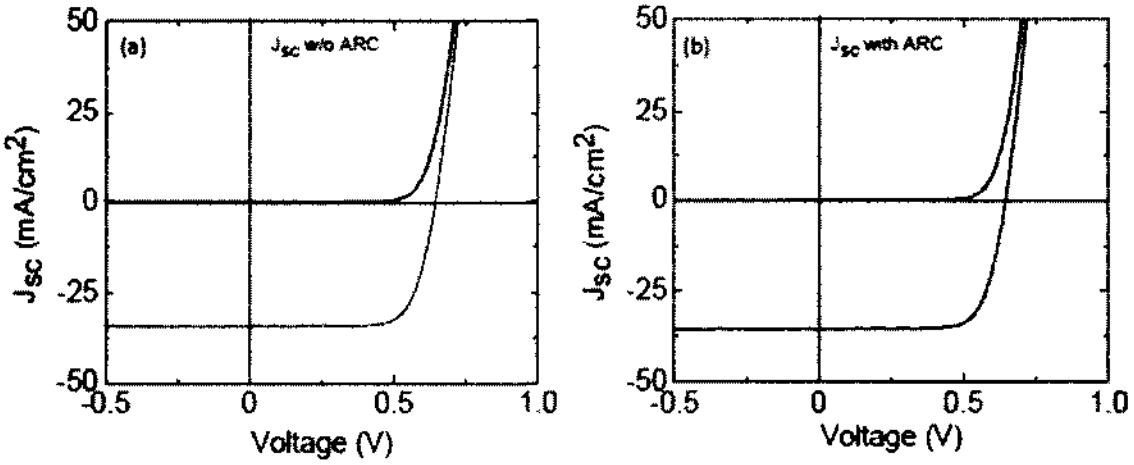

Figure 6.10 (a) Typical light and dark J-V curve for device fabricated from CIGS film deposited by 3-stage process without ARC and (b) typical light and dark J-V curve for device fabricated from CIGS film deposited by 3-stage process with ARC. Thicknesses of the CIGS layers are ~ 2.5 μm.

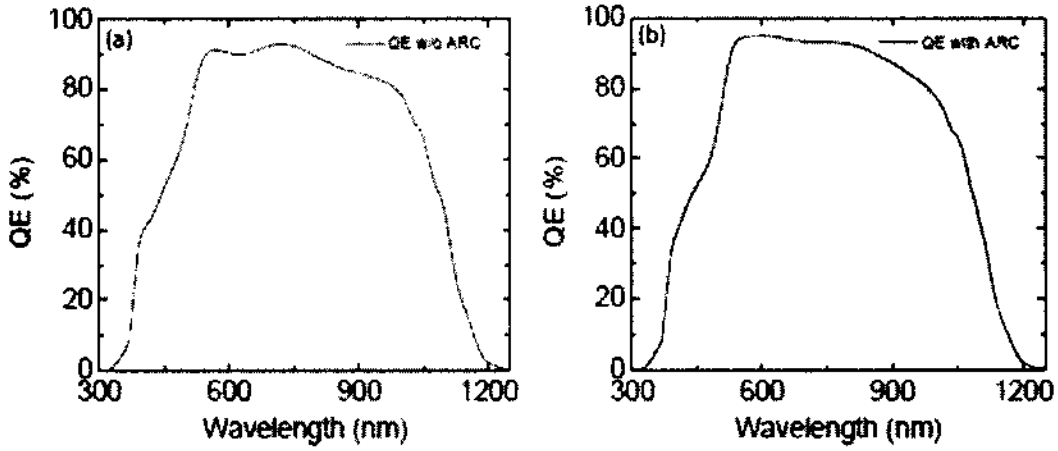

Figure 6.11 (a) Quantum efficiency curve for device fabricated from CIGS film deposited by 3-stage process without ARC and (b) Quantum efficiency curve for device fabricated from CIGS film deposited by 3-stage process with ARC. Thicknesses of the CIGS layers are ~ 2.5 μm.

The J-V data were analyzed using a standard diode equation considering the forward diode current limited by Shockley-Read-Hall (SRH) recombination through the states within the Space Charge Region (SCR) of the $Cu(In,Ga)Se_2$.The diode equation is given by

$$J = J_0 \exp\left(\frac{q(V - R_s J}{AkT}\right) - J_0 - J_L + GV \qquad (6.2)$$

where J_0 is the forward current, A the diode quality factor, R_s the series resistance, J_L the light generated current, and G the shunt conductance. The shunt conductance, calculated from the J-V characteristics in the dark was found to be small for these devices and is, therefore, neglected in the device analysis. Differentiation of (6.2) with $J_L = J_{sc}$ leads to

$$\frac{dV}{dJ} = R_s + \frac{AkT}{q}(J + J_{sc})^{-1} \qquad (6.3)$$

The series resistance (R_s) was around 1.1 Ω-cm^2 and A was around 1.7 for these devices. These data were derived from the slope and intercept, respectively, in a linear fit to dV/dJ plotted versus $(J+J_{sc})^{-1}$. Classically, the value of A is between 1 and 2. The higher value for the diode quality factor indicates that the main recombination mechanism is more closely related to space charge region recombination than to bulk recombination.

6.5 Summary

The co-evaporation system has been used to fabricate the CIGS absorber layer using co-evaporation process. Initially, the distance between the individual source and the substrate was very high (~ 30 inches). During the deposition process, it consumed a lot of source materials such as copper (Cu), indium (In), gallium (Ga) and selenium (Se), which wasted a lot of product during each deposition process. The system was then modified by raising each source in order to reduce the distance between the individual source and the substrate. After this modification, the consumption of each source was reduced significantly and led to better quality films as the rates were more constant over time. I-R sensor has been used to track the transitions between the Cu- rich and Cu-poor surfaces during CIGS deposition process. Each layer of CIGS solar structure was optimized to maintain the quality of each layer in order to fabricate the high efficient CIGS solar cells. Impurities in the CIGS absorber layer can have strong influence on the performance of the CIGS solar cell. The positive SIMS spectra analysis on a CIGS thin film deposited by 3-stage co-evaporation process on a Si wafer confirmed the presence of impurities like oxygen, hydrocarbon, magnesium, potassium, and calcium. The potential source of these impurities could be the liners which were used as evaporation containers for different

sources and other supporting parts in the deposition chamber. Several parts were covered by high purity molybdenum sheet, which can easily withstand the high temperature outside the sources (~ 500-600 °C). The positive SIMS depth profile spectra of CIGS films deposited on c-Si wafer after covering the parts with molybdenum sheet did not contain any calcium, magnesium and other peaks. After modification and enhancement of several of our processes, we were able to fabricate CIGS solar cells with efficiency as high as 17.1%.

CHAPTER 7

CONCLUSIONS

CIGS is a nearly perfect absorber layer for polycrystalline solar cells due to its close match of band gap with the solar spectrum, a relatively high absorption coefficient and good opto-electronic properties in the polycrystalline phase. The capacity to scale up any photovoltaic technology is one of the criteria that will determine its long-term viability. In the case of CIGS, many manufacturers such as Solar Frontier are showing the way for GW-scale production capacity. However, as CIGS technology continues to increase its share of the market, the scarcity and high price of indium will potentially affect its ability to compete with other technologies. One way to avoid this bottleneck is to reduce the importance of indium in the fabrication of the cell simply by reducing its thickness. Reducing the thickness will not only save the material but will also lower the production time and the power needed to produce the cell.

In Chapter 1, an introduction of solar cell technology and an outline of the dissertation objectives were given.

In Chapter 2, materials properties of $Cu(In,Ga)Se_2$ thin films and characterization techniques used to explore the $Cu(In,Ga)Se_2$ thin films and devices were presented. Characterization technique ranging in measurement settings from in-situ, real time growth monitoring to the characterization of the final solar cell have been discussed. It is always encouraged to use more than one characterization tool for the same material if possible in

order to develop a holistic idea of what is happening with the particular material or final device.

In Chapter 3, a brief review of the ultrathin CIGS solar cells and the effect of the absorber thickness on ultrathin CIGS films and devices were discussed. CIGS thin films with various thicknesses from 1.95 μm down to 0.5 μm were deposited by co-evaporation. CIGS solar cells were then fabricated with the following standard structure: glass/Mo/CIGS/CdS/ZnO/ITO/grid. Cells with total area of 0.50 cm^2 were defined by mechanical scribing. The efficiency of the completed device was extracted from J-V measurements under 100 mW/cm^2, and the currents confirmed by QE measurements under white light bias. The current and voltage were roughly constant as thickness reduced from 1.95 μm to 1.3 μm, while decreasing for 0.75 μm and 0.5 μm. The reduction in J_{sc} is likely due to the reduction in absorbance in long wavelength. The observed decrease in V_{oc} could be due to the increase in shunt conductance with reduction of the CIGS absorber layer thickness. The experimental results for ultrathin CIGS solar cells indicate that the efficiency drops not only due to the decrease in J_{sc}, which is expected since the absorber layer gets thinner, but also due to decrease in V_{oc} and FF. The degradation of the overall performance of the ultrathin CIGS solar could be due therefore to the combination of reduction in thickness of the absorber layer as well as the presence of impurities in the absorber layer. Numerical modeling of CIGS solar cells is an efficient way in order to verify the viability of created hypothesis depending on the physical explanations and to predict the effects of these physical changes on the solar cell performance. The simulated current-voltage characteristics of the ultrathin CIGS solar cells suggest that the deep states

defects that lye in the upper part of the energy gap are responsible for the deterioration of the overall solar cell performance of the ultrathin CIGS solar cells

In Chapter 4, characterization of ultra-thin CIGS films deposited by 1-stage, 2-stage and 3-stage process were discussed and the effect of selenium pressure on ultrathin CIGS films and devices were also are presented. The ultrathin CIGS films deposited by 1-stage, 2-stage and 3-stage co-evaporation processes were explored by in-situ spectroscopic ellipsometry via the real time monitoring of the dielectric functions, the thickness, and the roughness. Ultrathin CIGS with thickness ~ 0.7 μm were deposited by 1-stage, 2-stage and 3-stage co-evaporation processes and spectroscopic ellipsometry data were acquired with an energy range of 0.75–6.5 eV. Irrespective of the process, the initial nucleation stages of these ultrathin films show island growth or the Volmer-Weber (V-W) growth process. A comparison of the films in the nucleation stage reveals that the height of nuclei at the onset of coalescence is the lowest for films deposited by 2-stage process, where the Cu-rich growth phase is realized by supplying higher rate of Cu during the first stage. The observed nucleation behavior therefore suggests that this semi-liquid phase increases the mass transport, enhancing the contact and coalescence of the nuclei, leading to a decrease in their height, hence smoothening the early-stage film surface. Material properties of these ultrathin Cu(In,Ga)Se2 films deposited by 1-stage, 2-stage and 3-stage co-evaporation processes were characterized and compared using different optical and electrical characterization techniques such as spectroscopic ellipsometry (SE), XRD and AFM. Out of these three processes, the 3-stage process proved to be the best for growing device quality ultrathin $Cu(In,Ga)Se_2$ films. The solar cells processed from these ultrathin CIGS films with thickness ~ 0.7 μm were also characterized to compare the efficiency, voltage

and current. Current-voltage (J-V) and quantum efficiency (QE) measurements on these ultrathin CIGS solar cells helped us in understanding the reason for different efficiencies. Larger grain size, improved junction interface as well as Ga grading were some of the reasons for better efficiency of the solar cells processed from ultrathin CIGS deposited by 3-stage process.

Ultrathin and thick CIGS films deposited under various Se effusion rates were also studied by real time spectroscopic ellipsometry (RTSE) and ex-situ measurement. The surface morphology of the CIGS film was affected by Se flux rate. The grain size increases as Se rate increases. It was observed that the preferred orientation became (220) for the film with higher Se flux while it tended to be (112) with lower Se flux. These indicate that the Se flux rate significantly influences the crystal growth of CIGS. It was also observed that the hole concentration of the CIGS film increased and resistivity decreased with increasing Se flux. The higher SMR was found to be preferable in order to obtain better material properties to enhance the CIGS solar cell performance.

In Chapter 5, ultrathin CIGS films were deposited using a 3-stage process and detailed study was performed to describe (i) the use of RTSE for analysis of IGS during stage I of the deposition process; (ii) the conversion of IGS into CIGS during stage II and the rapid development of bulk $Cu_{2-x}Se$ during the end of stage II; and (iii) Cu-rich to Cu-poor CIGS thin film transition during stage III in order to maintain the stoichiometric composition of the final CIGS thin film. For $x = 0$, the initial roughness is very large but smoothening occurs via coalescence. In contrast, for $x = 1$, the initial surface is quite smooth and stable with time. Only for $x \sim 0.25$-0.3, does the roughness increase throughout deposition, indicating continuous growth of grains that protrude above the surface. A

significant change in roughness evolution is observed for $x > 0.5$ as the final surface roughness thickness decreases rapidly with x. RTSE enables therefore analysis of the structural evolution, grain growth processes, dielectric functions during CIGS fabrication. It also enables tracking of the IGS-to-CIGS conversion and the transitions between Cu-poor and Cu-rich films during CIGS growth. The RTSE method also proves to be a potentially important tool for end-point detection in each of the three stages of the CIGS growth.

In Chapter 6, the technique to advance the CIGS solar cell fabrication processes are discussed. The co-evaporation system has been used to fabricate the CIGS absorber layer using co-evaporation process. Initially, the distance between the individual source and the substrate was very high (~ 30 inches). During the deposition process, it consumed a lot of source materials such as copper (Cu), indium (In), gallium (Ga) and selenium (Se), which wasted a lot of product during each deposition process. The system was then modified by raising each source in order to reduce the distance between the individual source and the substrate. After this modification, the consumption of each source was reduced significantly and led to better quality films as the rates were more constant over time. I-R sensor has been used to track the transitions between the Cu- rich and Cu-poor surfaces during CIGS deposition process. Each layer of CIGS solar structure was optimized to maintain the quality of each layer in order to fabricate the high efficient CIGS solar cells. Impurities in the CIGS absorber layer can have strong influence on the performance of the CIGS solar cell. The positive SIMS spectra analysis on a CIGS thin film deposited by 3-stage co-evaporation process on a Si wafer confirmed the presence of impurities like oxygen, hydrocarbon, magnesium, potassium, and calcium. The potential source of these

impurities could be the liners which were used as evaporation containers for different sources and other supporting parts in the deposition chamber. Several parts were covered by high purity molybdenum sheet, which can easily withstand the high temperature outside the sources (~ 500-600 °C). The positive SIMS depth profile spectra of CIGS films deposited on c-Si wafer after covering the parts with molybdenum sheet did not contain any calcium, magnesium and other peaks. After modification and enhancement of several of our processes, we were able to fabricate CIGS solar cells with efficiency as high as 17.1%.

FUTURE CONSIDERATIONS

Tandem devices, as well as optimized ultra-thin CIGS devices with alternative back contact may be the next generation of photovoltaics devices. Reducing the thickness will not only save the material but will also lower the production time and the power needed to produce the cell. All these factors will help to reduce the production cost significantly. However, reduce light absorption will reduce the photocurrent. In order to optimize the photocurrent, multi-layer air coating and the alternative back contact will be the future solution for it.

By studying different aspects of ultrathin CIGS cells such as optimizing the different deposition techniques, first time use of real time insitu spectroscopic ellipsometer to study the effect of selenium in ultrathin CIGS thin films and devices, study of effect of impurities in ultrathin CIGS solar cells, the author of this thesis hopes to make a small contribution towards better understanding of the ultrathin devices. Better understanding should lead to get the world class efficient ultrathin CIGS solar cells.

REFERENCES

[1] J. K. Leggett. Half Gone: Oil, Gas, Hot Air and the Global Energy Crisis, Portobello Books (2005).

[2] A. Ken Zwiebel, The terawatt challenge for thin-film PV, NREL/TP-520-38350, (2005).

[3] M.A OpenEI. Transparent Cost Database. Available from: http://en.openei.org/apps/TCDB/.

[4] C. A. Wolden, J. Kurtin, J. B. Baxter, I. Repins, S. E. Shaheen, J. T. Torvik, A. A. Rockett, V. M. Fthenakis, and E. S. Aydil , "Photovoltaic manufacturing: Present status, future prospects, and research needs". J. of Vacuum Science & Technology A: Vacuum, Surfaces, and Films, 29(3): p. 030801-030801-16, (2011).

[5] P. Jackson, D. Hariskos, R. Wuerz, O. Kiowski, A. Bauer,T. M. Friedlmeier, and M. Powalla,"Properties of Cu(In,Ga)Se2 solar cells with new record efficiencies up to 21.7%, Phys. Status Solidi RRL, 1–4 (2014).

[6] J. A. Del Cueto, S. Rummel, B. Kroposki, C. Osterwald, and A. Anderberg, "Stability of CIS/CIGS Modules at the Outdoor Test Facility over Two Decades," 33rd IEEE Photovoltaic Specialists Conference San Diego, California, May 11–16, (2008).

[7] G. G. Voorwinden, R. Kniese, and M. Powalla, "In-line Cu(In,Ga)Se2 co-evaporation processes with graded band gaps on large substrates," Thin Solid Films, vol. 431-432, pp. 538—542 (2003).

[8] K. Ramanathan, R. Noufi, B. To, D. L. Young, R. Bhattacharya, M. A. Contreras, R. G. Dhere, G. Teeter "Processing and Properties of Sub-Micron CIGS Solar Cells" in Conference Record of the 2006 IEEE 41h World Conference on PV, p. 380 (2006).

[9] R. F. Pierret, Semiconductor Device Fundamentals, New York: Addison- Wesley Publishing Company, Inc, (1996).

[10] K. D. G. I. Jayawardena, L. J. Rozanski, C. A. Mills, M. J. Beliatis, N. Aamina Nismy and S. Ravi P. Silva, "Inorganics–in- organics: recent development and

outlook for 4G polymer solar cell", Nanoscale 5, 8411-8427 (2013).

[11] F. Haug, Edevelopment of CIGS superstrate thin film solar cells, Ph.D. Thesis, Swiss Federal institute of Tech. (2001).

[12] M K. Zweibel, Harnessing Solar Power: The Photovoltaics Challenge (Plenum Press, New York, (1990).

[13] A D. M. Chapin, C. S. Fuller, G. L. Pearson, "A new silicon p-n junction photocell for converting solar radiation into electrical power", J. Appl. Phys. 25, 676-677 (1954).

[14] M. A. Green, K. Emery, Y. Hishikawa, W. Warta, and E. D. Dunlop, "Solar cell efficiency tables (version 42)." Prog. Photovolt: Res. Appl. 21, 827 (2013).

[15] M. A. Green, "Third generation photovoltaics: solar cells for 2020 and beyond" Physica E 14, 65 (2002).

[16] W. Shockley, and H. J. Queisser, "Detailed Balance Limit of Efficiency of p-n Junction Solar Cells", J. Appl. Phys. 32, 510 (1961).

[17] W. N. Shafarman, S. Siebentritt, and S. Lars, "Cu(In,Ga)Se2 Solar Cells ." In: Luque, A., and Hegedus, S. (ed.), Handbook of Photovoltaic Science and Engineering (pp. 547). Wiley, New York, (2011).

[18] M. Belhadj, T. Tadjer, B. Abbar, Z. Bousahla, B. Bouhafs and H. Aourag, "Structural, electronic and optical calculations of Cu(In,Ga)Se2 ternary Chalcopyrites", Phys. Stat. Sol. 241, 2516-2528 (2004).

[19] U. Rau and H. W. Schock, in Solar Cells: Materials, Manufacture and Operation, eds. T. Markvart and L. Castaner, Elsevier, Great Britain, (2005).

[20] H. Schock, "Properties of Chalcopyrite-based Materials and Film Deposition for Thin-Film Solar cells", In: Y. Hamakawa, (eds.), "Thin Film Solar Cells: Next Generation Photovoltaics and its Applications", Springer, Berlin, pp.106, (2004).

[21] D. Hebert, "Optical characterization of copper indium gallium diselenide thin films",Ph.D. thesis, University of Illinois at Urbana-Champaign, (2012).

[22] B. J. Stanbery, "Copper Indium Selenides and Related Materials for Photovoltaic Devices, Critical Reviews in Solid State and Materials Science 27, 73 (2002).

[23] D. K. Schroder, "Semiconductor Material and Device Characterization", 3rd edition,Wiley, New York, (2006).

[24] S.-H. Wei, S.B. Zhang, A. Zunger, "Effects of Ga addition to $CuInSe_2$ on its electronic, structural, and defect properties", Appl. Phys. Lett. 72, 3199 (1998).

[25] N. Amin, "Promises of Cu (In, Ga)Se_2 Thin Film Solar Cells from the Perspective of Material Properties, Fabrication Methods and Current Research Challenges", J. of Appl. Sci., 11: 401-410 (2011).

[26] C. Suryanarayana, and M.G. Norton, X–Ray Diffraction: A Practical Approach, Plenum Press, New York, (1998).

[27] S. S. Hegedus, and W. N. Shafarman, "Thin–film solar cells: device analysis and Measurements", Progress in Photovoltaics: Research and applications **12**, 155 (2004).

[28] M. Gloeckler, Device physics of Cu(In,Ga)Se2 thin film solar cells, Ph.D. thesis, Colorado State University, (2005).

[29] S. Little, Enhancement of Cu(In,Ga)Se2 Solar Cells and Materials via the Incorporation of Silver, Ph.D. Thesis. University of Toledo: U.S (2011).

[30] V. Ranjan, Ph.D. Thesis. "Enhancement of the Deposition Processes of Cu(In,Ga)Se2 and CdS Thin Films via In-situ and Ex-situ Measurements for Solar Cell Application", The University of Toledo, Ohio, USA (2010).

[31] S. M. Sze, "Physics of semiconductor devices", John Wiley& Sons press, New York, (1981).

[32] M. Gloeckler, A. L. Fahrenbuch and J. R. Sites, in Proc. 3rd WCPEC, (2003).

[33] A. Lique and S. Hegedus , Handbook of Photovoltaic Energy Conversion and Engineering: John Wiley & Sons LTD, Chichester, West Sussex, England, (2003).

[34] W. Shockley, W. T. Read, Jr., "Statistics of the Recombinations of Holes and Electrons", Phys. Rev. 87, 835 (1952).

[35] Z. Jehl, F. Erfurth, N. Naghavi et al., "Thinning of CIGS solar cells: part II: cell characterizations," Thin Solid Films, **519**, 21, 7212–7215 (2011).

[36] J. T. Heath and J. D. Cohen, W. N. Shafarman, D. X. Liao and A. A. Rockett, "Effect of Ga content on defect states in $CuIn_{1-x}Ga_xSe_2$ photovoltaic devices," American Institute of Physics (2002).

[37] M. Igalsona, M. Edoff , "Compensating donors in Cu(In,Ga)Sez absorbers of solar cells," Thin Solid Films 480-481 322-326 (2005).

[38] W. Fucheng, T. Fuling, X. Hongtao, L. Wenjiang, F. Yudong, and R. Zhiyuan, "Effects of defect states on the performance of $CuInGaSe_2$ solar cells", Journal of Semiconductors, **35**, No. 2 (2014).

[39] O. Lundberg, M. Bodegard, and L. Stolt, "Influence of the $Cu(In,Ga)Se_2$ thickness and Ga Grading on Solar Cell Performance", Prog. Photovolt: Res. Appl. 11, 77–88 (2003).

[40] A. Han, Y. Zhang,W. Song, B. Li,W. Liu and Y. Sun, "Structure, morphology and properties of thinned CIGS films and solar cells", Semicond. Sci. Technol. 27, 035022 (2012).

[41] P. Jackson, D. Hariskos, E. Lotter et al., "New world record efficiency for $Cu(In,Ga)Se_2$ thin-film solar cells beyond 20%," Progress in Photovoltaics: Research and Applications, vol. 19, no. 7, pp. 894–897 (2011).

[42] B. D. Cullity, Elements of x-ray Diffraction, 2nd printing Adison-Wesley Publishing Company, Inc, (1959).

[43] M. Bodegard, O. Lundberg, J. Lu and L. Stolt, "Re-crystallisation and interdiffusion in CGS/CIS bilayers",Thin Solid Films 431-432, 46-52 (2003).

[44] M. E. Beck, A. Swartzlander-Guest, R. Matson, J. Keane and R. Noufi, "$Cu(In,Ga)Se_2$-based devices via a novel absorber formation process", Sol. Energy Mater. Sol.Cells 64, 135-65 (2000).

[45] Y. Liu, Y.S., and A. Rockett. wxAMPS Simulation software. Available from: https://wiki.engr.illinois.edu/display/solarcellsim/Simulation+Software.

[46] S. Degrave, M. Burgelman, and P. Nollet, "Modelling of polycrystalline thin film solar cells: new features in scaps version 2.3," in Proceedings of the 3rd World Conference on Photovoltaic Energy Conversion, pp. 487–490 (2003).

[47] J. Kessler, J. Scholdstrom, and L. Stolt, "Analysis of CIGS films and devices resulting from different Cu-rich to Cu-poor transitions," in Proceedings of the 17th European Photovoltaic Solar Energy Conference, pp. 1019 (2001).

[48] W. S. Chen, and R. A. Mickelsen, "Thin film CdS/$CuInSe_2$ hetero junction solar cell", Proc. SPIE 248, 62 (1980).

[49] J. Scholdstrom, J. Kessler, and M. Edoff, "Two-stage growth of smooth Cu(In,Ga)Se_2 films using end-point detection." Thin Solid Films, 61, 480–481 (2005).

[50] A. Gabor, J. Tuttle, D. Albin, M. Contreras, R. Noufi, and A. Hermann, "High-efficiency $CuIn_xGa_{1-x}Se_2$ solar cells made from $(In_xGa_{1-x})_2Se_3$ precursor films", Applied Physics Letters 65(2), 198 (1994).

[51] J. R. Tuttle, M. Contreras, M. H. Bode, D. Niles, D. S. Albin, R. Matson, A. M. Gabor, A. Tennant, A. Duda, and R. Noufi, "Structure, chemistry, and growth mechanisms of photovoltaic quality thin-film Cu(In,Ga)Se2 grown from a mixed-phase precursor" J. Appl. Phys. 77, 153 (1995).

[52] M. I. Alonso, M. Garriga, C. A. Durante Rincon, E. Hernandez, and M. Leon, "Optical functions of chalcopyrite $CuGaxIn_{1-x}Se_2$ alloys", Appl. Phys. A 74, 659 (2002).

[53] G. F. Feng, and R. Zallen, "Optical properties of ion-implanted GaAs: The observation of finite-size effects in GaAs microcrystals." Physical Review B, 40, 1064 (1989).

[54] W. N. Shafarman, S. Siebentritt, and L. Stolt, "Cu(In,Ga)Se_2 Solar Cells ." In: A. Luque, and S. Hegedus, (eds.), Handbook of Photovoltaic Science and Engineering, Wiley, NewYork, p.547 (2011).

[55] A.L. Patterson, "The Scherrer Formula for X-Ray Particle Size Determination", Physical review 56, 978 (1939).

[56] M. A. Contreras, B. Egaas, K. Ramanathan, J. Hiltner, A. Swartzlander, F. Hasoon and Rommel Noufi, "Progress toward 20% efficiency in CIGS polycrystalline thin-film solar cells", Prog. Photovolt. Res. Appl. 7, 311-316 (1999).

[57] N. Ott, G. Hanna, U. Rau, J. H. Werner, and H P Strunk, "Texture of Cu(In,Ga)Se2 thin films and nanoscale cathodoluminescence", J. Phys. Condens. Matter 16, S85-S89 (2004).

[58] U. Rau, and H. W. Schock, "Cu(In,Ga)Se_2 solar cells" , In: Clean Electricity from Photovoltaics" (pp. 277), Imperial College Press (2001).

[59] T. Dullweber, G. Hanna, U. Rau, and H.W Schock, "A new approach to high efficiency solar cells by band gap grading in Cu(In,Ga)Se_2 chalcopyrite semiconductors",Solar Energy Materials & Solar Cells 67,145 (2001).

[60] J. Song, S.S. Li, C.H. Huang, O.D. Crisalle, and T. J. Anderson, "Device modeling and simulation of the performance of $Cu(In_{1-x}Ga_x)Se_2$ solar cells" Solid-State Electronics **48**, 73 (2004).

[61] A. M. Gabor, J.R. Tuttle, M. H. Bode, A. Franz, A. L. Tennant, M. A. Contreras, R. Noufi, D.G. Jensen, and A.M. Hermann, "Solar Energy Materials and Solar Cells", 41-42, 247 (1996).

[62] G. Hanna, J. Mattheis, V. Laptev, Y. Yamamoto, U. Rau, H.W. Schock, "Influence of the selenium flux on the growth of Cu(In,Ga)Se_2 thin film", Thin Solid Films 431-432, 31–36 (2003).

[63] B. Marsen, S. Marsillac. S. Dom, R. Rocheleau, "Effect of selenium effusion rate on CIGS thin films deposited at low substrate temperature", Photovoltaic Specialists Conference, 31st IEEE, 386-389 (2005).

[64] D. J. Dwyer, S. B. Schujman, J. A. Novak, D. J. Metacarpa and P. Haldar, "Selenium flux effects on CIGS growth rate and control by in-line X-ray fluorescence, 39th Proceedings of the IEEE Photovoltaic Specialists Conference, 978 (2013).

[65] M. I. Alonso, M. Garriga, C. A. Durante Rincon, E. Hernandez, and M. Leon, "Optical functions of chalcopyrite $CuGaxIn_{1-x}Se_2$ alloys", Appl. Phys. A 74, 659 (2002).

[66] M. M. Islam, T. Sakurai, S. Ishizuka, A. Yamada, H. Shibata, K. Sakurai, K. Matsubara, S. Niki, and K. Akimoto, "Effect of Se/(Ga+In) ratio on MBE grown Cu(In,Ga)Se_2 thin film solar cell", J. Crystal Growth 311, 2212 (2009).

[67] J. AbuShama, R. Noufi, Y. Yan, K. Jones, B. Keyes, P. Dippo, M. Romero, M. Al-Jassim, J. Alleman, D. Williamson,"Cu(In,Ga)Se_2 thin-film evolution during growth from $(In,Ga)_2Se_3$ precursors", Materials Research Society Symposium Proceedings, 668: H7.2-1–6 (2001).

[68] R. W. Collins, I. An, J. Lee, and J. A. Zapien, "Multichannel ellipsometry", In: Tompkins, H. G. and Irene, E. A. (Eds.), Handbook of Ellipsometry. New York, Noyes (2001).

[69] S. Marsillac, M. N. Sestak, J. Li and R. Collins, Advanced Characterization Technique for thin film Solar cells, "Spectroscopic Ellipsmetry", (eds. D. A. Ras, T. Kirchartz, and U. Rau) Wiley-VCH Verlag GmbH& Co. KGaA, (2011).

[70] R. W. Collins, and B.Y. Yang,"In situ ellipsometry of thin-film deposition – implications for amorphous and microcrystalline Si growth." J. Vac. Sci. Technol. Bl, 1155 (1989).

[71] H. G. Tompkins, "A User's guide to ellipsometry", Academic press, New York, (1992).

[72] R. M. A. Azzam and N. M. Bashara, "Ellipsometry and Polarized light", Holland, Amsterdam, 1977. Tompkins, "A User's guide to ellipsometry", Academic press, New York, (1992).

[73] H. Fujiwara, "Spectroscopic Ellipsometry: Principles and applications", John Wiley & Sons Ltd, (2007).

[74] R.W. Collins and A.S. Ferlauto, in: Handbook of Ellipsometry. Edited by H.G. Tompkins and E.A. Irene, p. 94, (William Andrew, Norwich, NY, (2005).

[75] F. Wooten, "Optical properties of solids", New York, Academic press, (1972).

[76] J. A. Stoke. L. R. Dahal, J. Li, N. J. Podraza, X. Cao, X. Deng, and R. W. Collins, "Optimization of Si:H multijunction n-i-p solar cells through the development of deposition phase diagrams", Proc. 33rd IEEE Photovolt. Spec. Conf., IEEE, New York, Art No. 413 (2008).

[77] R. D. Guenter, "Modern Optics", Wiley, (1990).

[78] J. R. Tuttle, M. Contreras, M. H. Bode, D. Niles, D. S. Albin, R. Matson, A. M. Gabor, A. Tennant, A. Duda, and R. Noufi, J. Appl. Phys. 77, 153 (1995).

[79] A. F. da Cunha, D. Rudmann, P.M.P. Salomé, and F. Kurdesau, "Growth and characterization of CIGS solar cells by RF magnetron sputtering with continuous Se evaporation and end point detection", 20th Eur. Photovoltaic Solar energy Conf. Barcelona, Spain, Paper 4AV.1.33, pp 1819-1822 (2005).

[80] S. Nishiwaki, T. Satoh, Y. Hashimoto, T. Negami, and T.Wada, "Preparation of Cu(In,Ga)Se2 thin films at low substrate temperatures," J. Mater. Res., vol. 16, pp. 394–9 (2001).

[81] M. Nishitani, T. Negami, and T. Wada, "Composition monitoring method in $CuInSe_2$ thin film preparation", Thin Solid Films 258, 313 (1995).

[82] C R. Scheer, A. Neisser, K. Sakurai, P. Fons, and S. Niki, "Cu(In1−xGax)Se_2 growth studies by in situ spectroscopic light scattering" Appl. Phys. Lett. 82, 2091 (2003).

[83] J. L. Simpson, B. S. Joshi, L. A. Gonzales, and T. E. Furtak, "A Parallel Detecting, Spectroscopic Ellipsometer for Intelligent Process Control of Continuously Deposited CIGS Films", MRS Symp. Proc. 616, 9 (2000).

[84] M. Yuan, D. B. Mitzi, W. Liu, A. J. Kellock, S. J. Chey, and V. R. Deline, "Optimization of CIGS-Based PV Device through Antimony Doping", Chemistry of Materials 22, 285 (2010).

[85] S. Nishiwaki, T.Satoh, S. Hayashi, Y. Hashimoto, T. Negami, T. Wada, "Preparation of Cu(In,Ga)Se2 thin films from In–Ga–Se precursors for high-efficiency solar cells", J. Mater. Res. 14, 4514 (1999).

[86] A. M. Gabor , J R Tuttle, DS Albin, M A Contreras, R Noufi, A M Herman, "High- efficiency $CuInxGa_{1-x}Se_2$ solar cells made from $(In_x,Ga_{1-x})_2Se_3$ precursor films". Applied Physics Letters; 65(2): 198–200 (1994).

[87] W.N. Shafarman, J. Zhu, "Effect of substrate temperature and deposition profile on evaporated Cu (In,Ga)Se2 films and devices", Thin Solid Films; 361–362: 473–477 (2000).

[88] C.A. Gogol, H.S. Reagan "A performance comparison of vacuum deposition monitors employing atomic absorption (AA) and electron impact emission spectroscopy", Journal of Vacuum Science and Technology; A1 (2): 252–256 (1982).

[89] C.A. Gogol, C. Cipro. Current industrial practices—technical note: composition control of high temperature superconducting materials, Surface and Coatings Technology; 37: 339–348 (1989).

[90] L. Stolt, J. Hedstrom, D. Sigurd, "Coevaporation with rate control system based on quadrupole mass spectrometer", Journal of Vacuum Science and Technology, 3: 403–407 (1985).

[91] M. Nishitani, T. Negami, T. Wada,"Composition monitoring method in $CuInSe_2$ thin film preparation", Thin Solid Films; 258: 313–316 (1995).

[92] T. Negami, M. Nishitani, N. Kohara, Y. Hashimoto, T. Wada, "Real-time composition monitoring methods in physical vapor deposition of $Cu(In,Ga)Se_2$ thin films", Materials Research Society Symposium Proceedings; 67: 267–278 (1996).

[93] K. Ramanathan, M.A. Contreras, C.L. Perkins, S. Asher, F.S. Hasoon, J. Keane, D. Young, M. Romero, W. Metzger, R. Noufi, J. Ward, A. Duda,"Properties of 19.2% efficiency CuInGaSe2 thin-film solar cells", Progress in Photovoltaics: Research and Applications 11: 225–230 (2003).

[94] J. Kessler, J. Scholdstrom, L. Stolt, "Rapid $Cu(In,Ga)Se_2$ growth using end point detection", Proceedings of the 28th IEEE Photovoltaics Specialists Conference, 509–512 (2000).

[95] R. Scheer, C. Pietzker, D. Braunig, "Laser light scattering in-situ studies on the growth of chalcopyrite thin films", Materials Research Society Symposium Proceedings, 668: H7.3.1–H7.3.5 (2001).

[96] K. Sakurai, R. Hunger, R. Sheer, C.A. Kaufmann, A. Yamada, T. Baba, Y. Kimura, K. Matsubara, P. Fons, H. Nakanishi, S. Niki, In situ diagnostic methods for thin-film fabrication: utilization of heat radiation and light scattering, Prog. Photovolt: Res. Appl. 12, 219–234 (2004).

[97] J. S. Park, Z. Dong, S. Kim, and J. H. Perepezko, " $CuInSe_2$ phase formation during Cu_2Se/In_2Se_3 interdiffusion reaction." Journal of applied Physics, 87, 3683 (2000).

[98] J. AbuShama, R. Noufi, Y. Yan, K. Jones, B. Keyes, P. Dippo, M. Romero, M. Al Jassim, J. Alleman, and D. L.Williamson, "$Cu(In,Ga)Se_2$ Thin-Film Evolution DuringGrowth From $(In,Ga)_2Se_3$ Precursors", Mat. Res. Soc. Symp.Proc. H7.2.1 (2001).

[99] J. Kessler, M. Ruckh, D. Hariskos, U. Ruhle, R. Menner, , and H.W. Schock, "Interface engineering between CuInSe2 and ZnO." In: Proc. of the 23rd IEEE Photovoltaic Specialist Conference, pp.447 (1993).

[100] D. Lincot, R. Ortega-Borges, J. Vedel, , M. Ruckh, J. Kessler, K.O. Velthaus, D. Hariskos, H.W. Schock, , Proc. of the11th EC PVSEC, pp.870 (1992).

[101] J. H. Scofield, A. Duda, D. Albin, B. L. Ballard, and P. K. Predecki, "Sputtered molybdenum bilayer back contact for copper indium diselenide-based polycrystalline thin-film solar cells," Thin Solid Films 260, 26 (1995).

[102] T. Nakada, Y. Honishi, Y. Yatsushiro, and H. Nakakoba, Impacts of Sb and BiIn corporations on CIGS thin films and solar cells, in 37th IEEE Photovoltaic Specialist Conference (PVSC), 2011, pp. 003527–003531 (2011).

[103] D. Guettler, A. Chirila, S. Seyrling, P. Bloesch, S. Buecheler, X. Fontane, V. Izquierdo Roca, L. Calvo-Barrio, A. Perez-Rodriguez, J. Morante, A. Eicke, and A. Tiwari, "Influence of NaF incorporation during $Cu(In,Ga)Se_2$ growth on microstructure and photovoltaic performance", in 35th IEEE Photovoltaic Specialists Conference (PVSC), pp. 003420–003424 (2010).

[104] A. Rockett, J. S. Britt, T. Gillespie, C. Marshall, M. M. Al Jassim, F. Hasoon, R. Matson, and B. Basol, Na in selenized Cu(In,Ga)Se2 on Na-containing and Na free glasses: distribution, grain structure, and device performances, Thin Solid Films 372, 212 (2000).

[105] R. Scheer, H.W. Schock, "Chalcogenide Photovoltaics: Physics, Technologies and Thin Film Devices" Wiley-VCH Verlag GmbH & Co. KGaA, (2011).

APPENDICES

VITA

Krishna P. Aryal

231 Kaufman Hall
ECE Department
Old Dominion University
Norfolk, VA 23529

Education

2015	**Ph.D.**	Electrical Engineering	Old Dominion University, VA
2011	**M.E.**	Electrical Engineering	Texas Tech University, TX
2008	**M.S.**	Physics	University of Massachusetts Dartmouth, MA

Selected Peer Reviewed Publications

1. **K. Aryal**, H. Khatri, R.W. Collins, and S. Marsillac "In Situ and Ex Situ Studies of MolybdenumThin Films Deposited by rf and dc Magnetron Sputtering as a Back Contact for CIGS Solar Cells", *International Journal of Photoenergy* **2012**, 723714 (2012).
2. S. Marsillac, H. Khatri, **K. Aryal**, R.W. Collins "Properties of Cu(In,Ga)Se_2 Thin Films and Solar Cells deposited by Hybrid Process," *International Journal of Photoenergy* **2012**, 385185 (2012).

Selected Conference Proceedings

1. **K. Aryal,** G. Rajan, T. Ashrafee, V. Ranjan, J. Li. A. Rockett, R. W. Collins, S. Marsillac "Effect of selenium evaporation rate on ultrathin Cu(In,Ga)Se_2 films", *40th IEEE Photovoltaic Specialist Conference*, 113-B35, 2014, Denver, CO.
2. **K. Aryal**, G. Rajan, T. Ashrafee, V. Ranjan, P. Aryal, A. Rockett, R. W. Collins, S. Marsillac "Real time spectroscopic ellipsometry studies of ultrathin CIGS films deposited by 1-stage, 2-stage and 3-stage co-evaporation processes", *40th IEEE Photovoltaic Specialist Conference*, 114-B38, 2014, Denver, CO.
3. **K. Aryal**, Y. Erkaya, G. Rajan, T. Ashrafee, A. Rockett, R. W. Collins, S. Marsillac "Comparative Study of ZnS Thin Films Deposited by CBD and ALD as a Buffer Layer for CIGS Solar Cell", *Proc. 39th IEEE Photovoltaics Specialists Conference*, June 16-21, 2013, Tampa, FL.
4. **K. Aryal**, G. Rajan, Y. Erkaya, N. Hegde, P. Boland, V. Ranjan, R. W. Collins, and S. Marsillac "Characterization of TCO Deposition for CIGS Solar Cells", *Proc. 38th IEEE Photovoltaics Specialists Conference*, June 3-8, 2012, Austin, TX ,G4, p. 595.

Honors, Awards and Scholarships

- 2012 Outstanding Ph.D. Researcher Award in Electrical and Computer Engineering, ODU